



HAL
open science

Effects of ligand and receptor valence on the surface dynamics and nanoscale localization of synaptic membrane proteins

Camille Saphy

► **To cite this version:**

Camille Saphy. Effects of ligand and receptor valence on the surface dynamics and nanoscale localization of synaptic membrane proteins. Human health and pathology. Université de Bordeaux, 2018. English. NNT : 2018BORD0243 . tel-02177139

HAL Id: tel-02177139

<https://theses.hal.science/tel-02177139>

Submitted on 8 Jul 2019

HAL is a multi-disciplinary open access archive for the deposit and dissemination of scientific research documents, whether they are published or not. The documents may come from teaching and research institutions in France or abroad, or from public or private research centers.

L'archive ouverte pluridisciplinaire **HAL**, est destinée au dépôt et à la diffusion de documents scientifiques de niveau recherche, publiés ou non, émanant des établissements d'enseignement et de recherche français ou étrangers, des laboratoires publics ou privés.

THÈSE PRÉSENTÉE
POUR OBTENIR LE GRADE DE

DOCTEUR DE
L'UNIVERSITÉ DE BORDEAUX

ÉCOLE DOCTORALE SCIENCES DE LA VIE ET DE LA SANTE

SPÉCIALITÉ NEUROSCIENCES

Par Camille SAPHY

**EFFECTS OF LIGAND AND RECEPTOR VALENCE ON THE SURFACE
DYNAMICS AND NANOSCALE LOCALIZATION OF SYNAPTIC MEMBRANE
PROTEINS**

Sous la direction de : Olivier THOUMINE
co-directeur : Ehud ISACOFF (UC Berkeley)

Soutenue le 29 Novembre 2018

Membres du jury :

Mme MONTCOUQUIOL, Mireille	DR, Université de bordeaux	Présidente
M. SPECHT, Christian	CR, Institut de biologie de l'ENS	Rapporteur
Mme RENNER, Marianne	Professeur, Institut du Fer à Moulin	Rapporteur
Mme SALOME, Laurence	DR, Institut de pharmacologie et Biologie structurale	Examineur
M. SANDOZ, Guillaume	DR, Biology of Ion Channels	Examineur
M. VAFABAKHSH, Reza	Assistant Professor, University of Illinois	Invité

THÈSE PRÉSENTÉE
POUR OBTENIR LE GRADE DE

DOCTEUR DE
L'UNIVERSITÉ DE BORDEAUX

ÉCOLE DOCTORALE SCIENCES DE LA VIE ET DE LA SANTE
SPÉCIALITÉ NEUROSCIENCES

Par Camille SAPHY

**EFFECTS OF LIGAND AND RECEPTOR VALENCE ON THE SURFACE
DYNAMICS AND NANOSCALE LOCALIZATION OF SYNAPTIC MEMBRANE
PROTEINS**

Sous la direction de : Olivier THOUMINE
co-directeur : Ehud ISACOFF (UC Berkeley)

Soutenue le 29 Novembre 2018

Membres du jury :

Mme MONTCOUQUIOL, Mireille	DR, Université de bordeaux	Présidente
M. SPECHT, Christian	CR, Institut de biologie de l'ENS	Rapporteur
Mme RENNER, Marianne	Professeur, Institut du Fer à Moulin	Rapporteur
Mme SALOME, Laurence	DR, Institut de pharmacologie et Biologie structurale	Examineur
M. SANDOZ, Guillaume	DR, Biology of Ion Channels	Examineur
M. VAFABAKHSH, Reza	Assistant Professor, University of Illinois	Invité

– Summary –

Synapses are highly compartmentalized structures packed with interacting protein complexes. The synaptic cleft bridging pre- and post-synaptic compartments is an adhesive zone ~20 nm thick, containing adhesion proteins and neurotransmitter receptors.

Thanks to recent improvements in microscopy with the development of super-resolution imaging, it is now possible to observe and study synapses at the scale of their building blocks: the proteins. Studying the organization and the mobility of these molecules helps understand how synapses can perform distinct and specific functions.

A major way to visualize these molecules is to attach a fluorescent probe on them. However, these probes are sometimes as bulky as the molecules of interest themselves, and therefore, can disrupt the natural behavior and function of these molecules, such as the way they assemble and interact together. For instance, the traditional ways to label receptors rely on antibodies, whose relatively large size (~15 nm) may lead to steric hindrance and localization bias, while their divalence can cause protein cross-linking.

To solve these problems, new probes are continuously being developed, each one of them with their advantages and drawbacks, which are yet mostly unknown and need to be characterized.

In my thesis, I focused on the impact of probe and receptor valence on the diffusion and organization of 3 synaptic proteins: β -neurexin1, neuroligin1, and the GluK2 kainate receptor subunit, using different microscopy techniques in a controlled environment. After characterizing the receptor stoichiometry with single photobleaching step counting, I highlighted the special attention that should be taken with regards to probe concentration and labeling conditions to achieve minimal impact on protein natural behavior. In this view, low labeling concentration of multivalent probes does not seem to alter freely moving protein diffusion, as measured by uPAINT experiments. On the other hand, FRAP experiments showed that saturating labeling concentrations strongly disrupt protein diffusion and immobilization, with varying degrees depending on the probe valence and size. Indeed, clustering the protein of interest by multivalent probes leads to enlarged immobile fractions and decreased diffusion coefficients, effects that are even larger when the protein displays multiple binding sites.

Finally, the changes in the number of proteins counted inside clusters in super-resolved dSTORM images are very nuanced and open to interpretation, with multiple parameters to consider to avoid counting biases.

This study, carried out on freely moving protein expressed in COS-7 cells, combined with other specific studies on synaptic proteins in cultured neurons, suggest that even more precious care should be taken when labelling proteins in confined spaces such as synapses, where large and multivalent probe would have drastic effects, thereby highlighting the crucial issues at stake in labeling strategies.

– Résumé –

Les synapses sont des structures hautement compartimentées contenant de larges complexes protéiques interagissant entre eux. Les compartiments pré- et post-synaptiques forment une zone adhésive d'environ 20 nm d'épaisseur riche en protéines d'adhésion et récepteurs aux neurotransmetteurs. Grâce aux récentes améliorations en microscopie optique, notamment avec le développement de l'imagerie à super-résolution, il est désormais possible d'observer et d'étudier les synapses à l'échelle de leurs composantes premières : les protéines. L'étude de l'organisation et de la mobilité de ces molécules aide à mieux comprendre comment les synapses peuvent exercer des fonctions distinctes et spécifiques essentielles à la transmission neuronale. Une méthode clé pour visualiser ces molécules consiste à y attacher une sonde fluorescente. Mais ces sondes sont parfois aussi volumineuses que les molécules d'intérêt elles-mêmes, et par conséquent, peuvent perturber le comportement et la fonction naturels de ces molécules, comme la façon dont elles vont s'assembler et interagir ensemble. Par exemple, les méthodes traditionnelles de marquage des récepteurs reposent sur l'utilisation d'anticorps, dont la taille relativement importante (environ 15 nm) peut entraîner une gêne stérique et un biais de localisation, tandis que leur divalence entraîne une réticulation des protéines. Pour résoudre ces problèmes, de nouvelles sondes sont constamment développées, chacune avec ses avantages et ses inconvénients pour la plupart inconnus et qui appellent à une caractérisation plus précise. Dans ma thèse, je me suis concentrée sur l'impact de la valence des sondes et de la stœchiométrie de la protéine d'intérêt sur la diffusion et l'organisation de 3 protéines synaptiques : β -neurexine1, neuroligine1 et la sous-unité GluK2 du récepteur kainate, en utilisant différentes techniques de microscopie dans un environnement membranaire contrôlé. Après avoir caractérisé la stœchiométrie des 3 récepteurs étudiés par une technique de comptage des sauts de photo-blanchiment, j'ai souligné l'attention particulière qui doit être portée aux concentrations de sondes utilisées, ainsi qu'aux conditions de marquage, au sens large, pour assurer un impact minimal sur le comportement naturel des protéines. Ainsi, la valence et la taille des sondes ne semblent pas altérer la diffusion des protéines se mouvant librement dans un environnement non confiné, avec les faibles concentrations de sondes utilisées lors des expériences de uPAINT. Cependant, les concentrations de marquage quasi-saturantes utilisées pour les expériences de FRAP ont

un effet très marqué sur la diffusion et l'immobilisation des protéines. En effet, une fraction immobile élevée et un coefficient de diffusion lent peuvent être mesurés lors de la réticulation des protéines par la liaison à des sondes multivalentes, et cet effet est d'autant plus important que la protéine présente plusieurs sites de liaison. En revanche, bien que reposant également sur une concentration élevée en sonde, le comptage des protéines sur des images super-résolues de dSTORM sont très nuancés et ouverts à l'interprétation, avec de multiples paramètres à prendre en compte pour éviter les biais éventuels. Cette étude réalisée sur des protéines diffusant librement à la membrane de cellules COS-7 et combinée aux résultats d'autres études spécifiques sur des protéines synaptiques réalisées dans des neurones en culture, suggère que des précautions supplémentaires doivent être prises lors de l'utilisation dans des espaces confinés tels que les synapses, où la taille et la valence des sondes vont avoir des effets encore plus drastiques, soulignant ainsi les enjeux cruciaux des stratégies de marquage.

– Remerciements –

Je tiens à exprimer ma profonde gratitude aux membres du jury pour avoir accepté d'évaluer ce travail : Mireille Montcouquiol, Marianne Renner, Christian Specht, Laurence Salomé, Guillaume Sandoz. Je remercie également Reza pour son soutien et son amitié au cours de mon séjour à Berkeley, et d'avoir accepté d'assister à ma soutenance.

Merci à l'IdEx et la Fondation pour la Recherche Médicale d'avoir financé ma thèse, ainsi que la Fulbright pour le financement de mon année aux Etats-unis.

Je remercie mes directeurs de thèse, Olivier Thoumine sans qui cette thèse n'aurait pu être réalisée, et Ehud Isacoff pour son humanité et sa bienveillance.

Je remercie bien entendu l'ensemble des membres des équipes dont j'ai eu la chance de faire partie, la liste étant particulièrement longue, je ne donnerai que quelques noms : Béatrice, Séb et Cherry (sans qui notre travail de recherche n'avancerait certainement pas aussi rapidement) et toutes ces personnes qui m'ont aidée dans ma réflexion scientifique : Reza, Shai, Shashank, Chris, Matthieu, Mathieu, Thomas, Amine, Konstantina... Je tiens à remercier également ces personnes qui ont pris le temps de se pencher sur mon travail : Corey, Florian, Jean-Baptiste, Mathieu, Eric et Léa.

De manière générale, je tiens particulièrement à exprimer ma gratitude à l'équipe de Berkeley, pour leur soutien sans faille après un accident de la voie publique qui a eu lieu au cours de mon séjour aux USA : vous êtes des exemples d'humanité et d'altruisme, je vous serai éternellement reconnaissante.

Parce qu'au cours d'une thèse il est avant tout nécessaire d'être bien entouré, je remercie chaleureusement toutes ces personnes qui ont rendu la route moins difficile, qui ont su me faire sourire, rire, et m'ont tendu la main dans les moments les plus durs, ces collègues qui sont devenus des amis. Thomas mon bro', Léa ma meuf, Konstantina et Sandra pour les pauses bateau et cinéma, Amine le super héros, Ani et Steve (qui devraient s'améliorer en badminton), Matthieu pour nos discussions très passionnées, le petit poulet Sébastien, le quadrilingue Filipe, et notre innocente petite Zeynep.

Je remercie évidemment mes amis : Ambre, tu es merveilleuse, on débattrait encore beaucoup, mais ton soutien m'a été vital, Marion qui est passée par là avant moi. Dam, tu as fait de Berkeley une autre expérience.

Enfin, ma famille, vous restez ma première ressource, un soutien infaillible, mon lieu de confiance. Je remercie donc mes 3 parents : ma mère pour son amour inconditionnel et sa confiance absolue, mon beau-père, véritable coach personnel, le guerrier qui a forgé la personne que je suis maintenant (Patrick, j'ai fini mon marathon !), mon père qui voit en moi plus que je ne verrai jamais, modèle d'optimisme et de force. Et je remercie mes 2 frères, ces génies, et mes antithèses : mon grand frère Julien, qui a de la confiance pour deux et qui m'aidera toujours à me relever, et Antoine, mon petit frère, Piccolo, merci pour nos moments de détente. Vous êtes tous de belles personnes, je suis fière de vous avoir comme famille.

– Contexte –

Cette thèse a été réalisée en co-direction entre l'Université de Bordeaux et l'Université de Berkeley, sous la direction d'Olivier Thoumine et Ehud Isacoff respectivement, sur la base d'un financement ANR et d'un financement IdEx. La quatrième année a été financée par la Fondation pour la Recherche Médicale.

Les premiers mois de ma thèse ont été consacrés à poursuivre mon travail de master 2 sur la fonction des neuroligines (cf - ANNEXES). Pendant le reste de la première année, je me suis ensuite intéressée à la plasticité homéostatique et la manipulation des LiGluR (cf - ANNEXES). Devant le manque de résultat sur le scaling des récepteurs AMPA, j'ai appris les techniques de single molecule pull down, durant mon bref séjour à Berkeley. Enfin, à mon retour à Bordeaux et après une interruption liée à un accident de la voie publique, je me suis intéressée aux phénomènes d'oligomérisation induits par différentes techniques de marquage sur 3 protéines : la β -neurexin1, la neuroligin1 and les récepteurs kaïnate GluK2 (expérience représentant l'essentiel du manuscrit), principalement sur un modèle de cellules hétérologues.

– Table of contents –

– Summary –	3
– Résumé –	5
– Remerciements –	7
– Contexte –	9
– Table of contents –	11
– Abbreviations –	17
– List of figures –	19
1. - Introduction -	23
1.1. Essentials of optical microscopy	29
1.1.1. Fluorescence fundamentals	30
1.1.2. Fluorescence microscopy: contrast and signal to noise ratio	31
1.1.2.1. Image contrast	31
1.1.2.2. Signal to noise ratio	34
1.1.3. Point Spread Function and resolution	35
1.1.3.1. Point Spread Function	35
1.1.3.2. Resolution	36
1.1.4. From microscope to nanoscope	37
1.2. Single molecule localization microscopy: protein organization and quantitative microscopy	38
1.2.1. Principle	38
1.2.2. Localization precision and localization accuracy	40
1.2.2.1. Localization precision	40
1.2.2.2. Localization accuracy	41
1.2.3. Single molecule localization microscopy techniques	42

1.2.3.1.	PALM	42
1.2.3.2.	STORM/dSTORM.....	43
1.2.4.	Applications.....	45
1.2.4.1.	the single molecule localization microscopy: a new tool for relative and absolute quantification	46
1.3.	Fluorescence microscopy and protein dynamics.....	50
1.3.1.	FRAP.....	50
1.3.2.	Single particle tracking	51
1.3.2.1.	The single particle tracking concept	51
1.3.2.2.	The single particle tracking: detection and trajectory reconstructions	53
1.3.2.3.	The single particle tracking: analysis	55
1.3.2.4.	Localization precision and limitations.....	57
1.4.	Probes for single molecule localization microscopy	58
1.4.1.	Intrinsic probes.....	58
1.4.2.	Extrinsic probes	60
1.4.2.1.	Semi-conductors	60
1.4.2.2.	Antibodies	61
1.4.2.3.	Alternative methods relying on recombinant protein expression	61
1.4.2.4.	DNA-PAINT	62
1.5.	Labeling-induced biases in organization and diffusion studies	64
1.6.	Experimental design in the synaptic context	65
1.6.1.	Glutamatergic receptors	66
1.6.2.	Synaptic cell adhesion molecules.....	66
2.	-Materials and Methods-.....	71
2.1.	Slide and coverslip preparation.....	72
2.1.1.	Culture support preparation	72

2.1.2.	Slide and coverslip preparation for single molecule pull down.....	72
2.1.2.1.	Slide and coverslip cleaning.....	72
2.1.2.2.	Aminosilanization.....	73
2.1.2.3.	PEGylation.....	73
2.2.	Cell culture and transfection.....	73
2.2.1.	COS-7 cells.....	73
2.2.2.	HEK 293 cells.....	74
2.2.3.	Primary neuronal cultures.....	74
2.2.3.1.	Coating, and dissection of the glia for Banker's cultures.....	74
2.2.3.2.	Coating, and dissection of the neurons for Banker's cultures.....	75
2.3.	Expression constructs.....	75
2.4.	Labeling strategies and fixation.....	76
2.4.1.	Fluorescent probes.....	76
2.4.2.	Labeling.....	76
2.4.2.1.	uPAINT labeling.....	77
2.4.2.2.	FRAP and dSTORM labelling.....	78
2.4.3.	Fixation for dSTORM.....	78
2.5.	Microscopy.....	78
2.5.1.	Setup configuration.....	78
2.5.2.	Single photobleaching step counting.....	79
2.5.2.1.	Cell lysate preparation.....	79
2.5.2.2.	Observation chamber preparation.....	79
2.5.2.3.	Acquisition and analysis.....	80
2.5.3.	Single molecule tracking: uPAINT.....	80
2.5.3.1.	Acquisition.....	80
2.5.3.2.	Trajectory analysis and image reconstruction.....	80

2.5.3.3.	Localization precision and $D_{\text{threshold}}$	81
2.5.4.	Fluorescent Recovery After Photobleaching: FRAP	81
2.5.5.	dSTORM	82
2.6.	Statistical analysis.....	85
3.	- Results -	87
3.1.	Characterization of the receptor stoichiometry	89
3.2.	Effect of probe binding on the protein diffusion using uPAINT	91
3.3.	Effect of probe binding on the protein diffusion using FRAP	98
3.4.	Effect of probe binding on protein aggregation level	104
3.4.1.	Effect of probe size and valence on nanoscopic organization of the monomeric proteins AP-TMD and AP- β -nrxn1	106
3.4.2.	Effect of probe size and valence on AP-nlgn1 dimer nanoscopic organization.....	109
3.4.3.	Effect of probe size and valence on the tetrameric AP-GluK2 nanoscopic organization	110
3.4.1.	Effect of probe size and valence on the cluster size measured with dSTORM	112
3.4.2.	Effect of probe concentration and incubation time on the nanoscopic organisation of AP-GluK2.....	113
3.5.	Quantification of protein levels in neurons	116
4.	- Discussion –	119
4.1.	Receptor stoichiometry	122
4.2.	Probe size and valence affects protein diffusion when high labeling concentration are used but not with low concentration	123
4.2.1.	Effects of probe size and valence on protein diffusion assessed by uPAINT... ..	123
4.2.2.	Effect of probe size and valence on protein diffusion assessed by FRAP	126
4.3.	Probe size and valence impact the aggregation of membrane proteins.....	129
4.3.1.	The analytical approach	130
4.3.2.	Aggregation levels	131

4.3.3.	Main analytical limitations	133
4.4.	Quantification of protein levels in neurons	135
4.5.	Conclusion: from COS-7 to synapses.....	136
5.	- Bibliography -	139
6.	- ANNEXES -	151

– Abbreviations –

AP	Acceptor Peptide
BirA ^{ER}	Endoplasmic reticulum located biotin ligase enzyme
DIV	Day In Vitro
dSA	divalent streptavidin
dSTORM	direct Stochastic Optical Reconstruction Microscopy
EGF	Epidermal Growth Factor
EPSC	Excitatory Post Synaptic Current
FRAP	Fluorescent Recovery After Photobleaching
HILO	Highly Inclined and Laminated Optical
KD	Knock Down
KI	Knock In
KO	Knock Out
LiGluR	Light-gated ionotropic glutamate receptor
LTD	Long Term Depression
LTP	Long Term Potentiation
MAG	Maleimide Azobenzene Glutamate
mEPSC	miniature Excitatory Post-Synaptic current
mSA	monovalent streptavidin
MSD	Mean Squared Displacement
Nlgn	Neuroigin
Nlgn1-EL	neuroligin1 E584A/L585A mutant
Nrxn	Neurexin
PA	Photo-activable fluorophore

PALM	PhotoActivated Localization Microscopy
PC	photoconvertible probe
PEG	PolyEthyleneGlycol
PLL	poly-lysine
PS	Photo-witchable fluorophore
PSD	Post-synaptic density
PSF	Point Spread Function
QD	Quantum dots
SCAM	Synaptic Cell Adhesion Molecule
SIM	Structured Illumination Microscopy
SMLM	Single Molecule Localization Microscopy
SNR	Signal to Noise Ratio
SPIM	Selective Plane Illumination Microscopy
Spt	Single particle tracking
STED	Stimulated Emission Depletion
TIRF	Total Internal Reflexion Fluorescence
TMD	TransMembrane Domain
TTX	Tetrodotoxin
uPAINT	universal Point Accumulation Imaging in Nanoscale Topography
WT	Wild type

– List of figures –

Figure 1. Drawing from Ramón y Cajal of chicken cerebellar cells.	25
Figure 2. Synapses construct neural circuits	27
Figure 3: Schematic of an optical microscope.	29
Figure 4: Jablonsky diagram displaying the energy steps of a molecule during fluorescence.	31
Figure 5: Absorption and emission spectra of a fluorescent molecule.	32
Figure 6: Principle of an epi-fluorescence microscope.	33
Figure 7: Illustration of epi, HILO and TIRF illumination	34
Figure 8: Point Spread Function	35
Figure 9: Illustration of the diffraction limit for visible light defined by Ernst Abbe.	36
Figure 10: Basic principle of single molecule localization microscopy.	39
Figure 11: Framework for localization, and super-resolved image construction from single molecule data.	40
Figure 12: Super-resolutive localization with PALM technique	43
Figure 13: Jablonsky diagram displaying the energy steps of a molecule during fluorescence and phosphorescence.	44
Figure 14: Schematic of the different types of probes	49
Figure 15: Summary of the different biases that can lead to undercounting or overcounting of the molecule of interest.	50
Figure 16. Principle of FRAP technique	51
Figure 17: Principles of the uPAINT technique.	53
Figure 18: Framework for localization, reconnection, and construction of trajectories from single molecule data.	55
Figure 19: MSD based analysis	56
Figure 20: Tri-dimensional structure of the Green Fluorescent protein.	59
Figure 21: Summary of the different probes for SMLM with their properties.	63
Figure 22. Scheme illustrating the labeling of AP-tagged membrane protein.	77
Figure 23: Localizations and image reconstruction.	84
Figure 24: Cluster analysis	85
Figure 25. Single-molecule subunit counting on the three membrane proteins.	90

Figure 26. uPAINT of AP- β -nrxn1 with mSA or biotin antibody or streptavidin.	93
Figure 27. uPAINT of AP-Nlgn1 with mSA or biotin antibody or streptavidin.	94
Figure 28. uPAINT of AP-GluK2 with mSA or biotin antibody or streptavidin.	95
Figure 29: Effect of incubation time of streptavidin-Atto594 on the diffusion of AP-GluK2 using uPAINT.....	96
Figure 30: Effect of the concentration of the probe on the diffusion of AP-GluK2 using uPAINT.	97
Figure 31. FRAP experiments on AP- β -Nrxn1, AP-Nlgn1 and AP-GluK2, labeled with mSA, dSA, anti-biotin antibody, or streptavidin.....	100
Figure 32. FRAP experiments on AP- β -Nrxn1 labeled with mSA or streptavidin compared to GFP- β -Nrxn1 and AP-TMD labeled with mSA.	101
Figure 33: FRAP experiments on AP-TMD, AP-nlgn1 and AP-GluK2, labeled with mSA, dSA, anti-biotin antibody, or streptavidin.	103
Figure 34: dSTORM of AP-TMD, AP- β -nrxn1, AP-nlgn1 and AP-GluK2, labeled with mSA, dSA, anti-biotin antibody, or streptavidin.....	105
Figure 35: dSTORM of AP-TMD labeled with mSA, dSA, anti-biotin antibody, or streptavidin conjugated to alexa647.....	107
Figure 36: dSTORM of AP- β -nrxn1 labeled with mSA, dSA, anti-biotin antibody, or streptavidin conjugated to alexa647.....	108
Figure 37: dSTORM of AP-nlgn1 labeled with mSA, dSA, anti-biotin antibody, or streptavidin conjugated to alexa647.....	110
Figure 38: dSTORM of AP-GluK2 labeled with mSA, dSA, anti-biotin antibody, or streptavidin conjugated to alexa647.....	111
Figure 39: Cluster size of AP-TMD, AP- β -Nrxn1AP-nlgn1 and AP-GluK2, labeled with mSA, dSA, anti-biotin antibody, or streptavidin on dSTORM pointillist images.	112
Figure 40: dSTORM of AP-GluK2 labeled with 5.8 nM, 58 nM, or 580 nM, of streptavidin conjugated to alexa647.....	114
Figure 41: dSTORM of AP-GluK2 labeled with streptavidin conjugated to alexa647 for 10 min, 20 min, or 40 min.	115
Figure 42: Nanoscale organization of AP-b-Nrxn1 labeled with mSA-Alexa647 at the pre-synapse using dSTORM.	116

Figure 43: Nanoscale organization of AP-Nlgn1 labeled with mSA-Alexa647 at the post-synapse using dSTORM.	117
Figure 44: Nanoscale organization of AP-GluK2 labeled with mSA-Alexa647 at the post-synapse using dSTORM.	118
Figure 45: Alternative labeling strategies.	122
Figure 46: Labeling strategy for dSTORM and probe undercounting illustrated on AP-nlgn1.	134
Figure 47: Illustration of the probe counting limitations on AP-TMD and AP-GluK2 in dSTORM.	135
Figure 49. Principles of light-gated glutamate receptors (LiGluRs).	157
Figure 50: Effect of LiGluRs expression on mEPSCs of cultured neurons	159
Figure 51: Effect of chronic wide-field light-activation of LiGluR on AMPA receptor and synapse number.	160

– CHAPTER 1 –

Introduction

For millennia, the mental activity headquarters were thought to lie in the center of the human body: the heart. This belief, probably born from the fact that cardiac manifestations can be observed and felt during intense emotions (contrasting with the absolute absence of sensitivity of the brain), left its stamp in many adages: “to have a heartbreak”, “to be cold-hearted”, “learning by heart” ...

Then, along the centuries, little by little, the brain was placed as the active center of knowledge and emotions. For La Mettrie, the body should be considered as a machine in which the brain would be the organ hosting the soul. During the 19th century, the development of phrenology led to the discovery of several functions of the cortex, and later, to the observations of Broca on the language areas of the brain. The end of the 19th century was marked by the development of novel research tools to improve the research on the brain, which was, until then, only relying on descriptive anatomy. With the development of microscopy, a crucial milestone was reached by Ramón y Cajal, with the discovery and description of the cells forming the nervous system: the neurons (**Figure 1**).

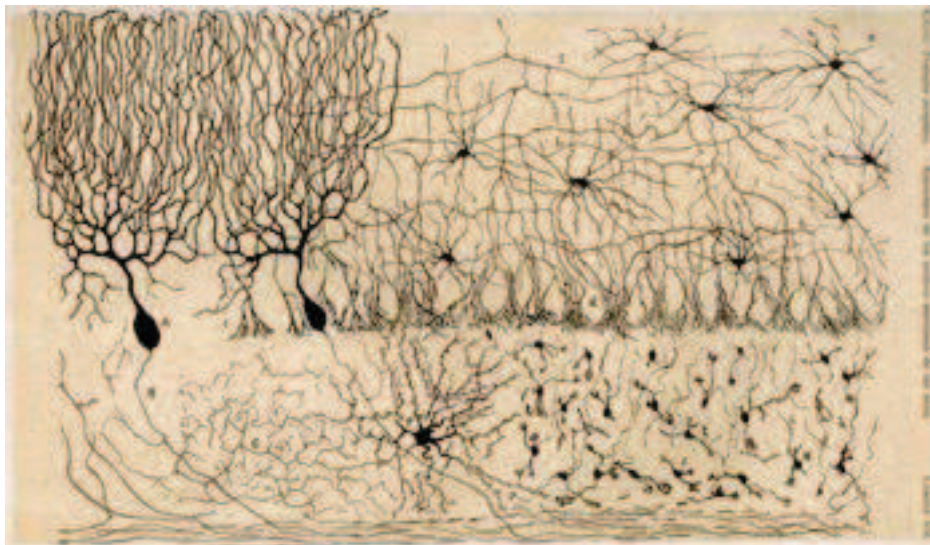


FIGURE 1. DRAWING FROM RAMÓN Y CAJAL OF CHICKEN CEREBELLAR CELLS.
(Estructura de los centros nerviosos de las aves, 1905)

The last centuries have led to many discoveries, and a large understanding of the different brain areas and functions, even though entire continents remain unexplored. While recent studies have highlighted the importance of the body as a whole, for instance the gut microbiota seem to play a key role in neurodevelopmental disorders (Hsiao et al., 2013; Kim

et al., 2017), the brain remains the keystone of consciousness, encoding each of our behaviors, reaction, and adaptation to our environment.

The human brain is composed of around 100 billion neurons, relaying the information from our sensory organs, to program the most adapted reaction with regards to our memory, our innate instincts, and this reaction is in turn relayed to our motor organs. In order to relay, store, and reuse information, neurons are connected into millions of overlapping and interdigitated neural circuits, through communication nodes called synapses.

Two distinct classes of synapses have been described: the electrical synapse, which relies on ionic currents through channels that connect physically two cells (gap junctions), and the more complex, chemical synapse. In the central nervous system of vertebrates, chemical synapses represent a large majority of the synapses. Chemical synapses are highly specialized junctions between neurons, with compartments structurally distinguishable, where the information is computed and transmitted from a donor neuron to an acceptor neuron, forming respectively the pre- and the post-synapse (**Figure 2**). The pre-synaptic terminal contains hundreds of vesicles loaded with neurotransmitter, which are endogenous chemicals including specific amino acids or monoamines. The fusion of those vesicles with the neuron's plasma membrane at active sites, following an action potential, leads to the release of neurotransmitters into the extracellular space, called the synaptic cleft. Once in the synaptic cleft, the neurotransmitters are detected by specific receptors located in the post-synaptic membrane. The activation of those receptors induces the generation of ion influx and local changes of the cell membrane polarization, leading to different signaling cascades.

Chemical synapses can be further divided into several categories depending of the main neurotransmitter used: the excitatory synapses, with the glutamate as the principal neurotransmitter, the inhibitory synapses using Glycine or GABA (γ -aminobutyric-acid) and the modulatory synapses (dopamine, serotonin, acetylcholine...).

Excitatory synapses comprise a relatively narrow synaptic cleft (~ 20 nm) and a thick electron-dense post-synaptic density (PSD) that spans around 300 nm in width. Considering the density of molecules in the PSD with regard to the pre-synaptic active zone, those synapses are referred to as asymmetric synapses (**Figure 2**). The activation of post-synaptic glutamate receptors, consecutive to the release of glutamate from the pre-synaptic terminal, leads to a

local depolarization of the post-synaptic membrane that, in turn, activates voltage-gated ionic channels, triggering a global depolarization (excitation) of the post-synaptic neuron.

On the contrary, inhibitory synapses present a narrow synaptic cleft ($\sim 10\text{-}12\text{ nm}$) and PSD of comparable thickness, and are thus, referred to as symmetric synapses. Post-synaptic receptor activation by glycine or GABA induces a hyperpolarization (inhibition) of the post-synaptic cell.

The modulatory synapse aims to regulate the post-synaptic neuron. In contrast with excitatory and inhibitory transmission in which the neurotransmitters target fast-acting receptors at the partner neuron post-synapse precisely aligned to the pre-synaptic terminal, neuromodulators diffuse through neural tissue to affect slow-acting receptors of many neurons.

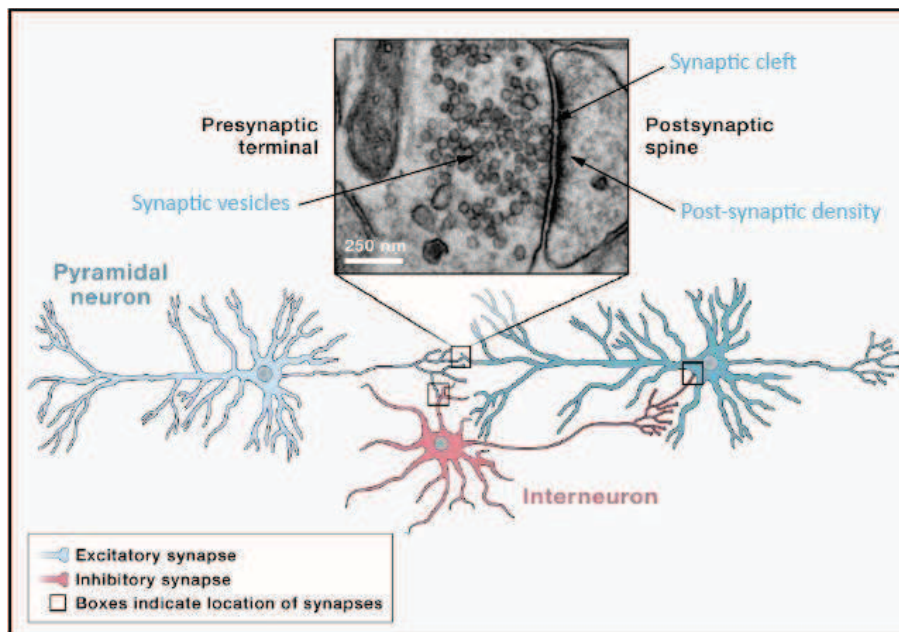


FIGURE 2. SYNAPSES CONSTRUCT NEURAL CIRCUITS

Schematic of a neural microcircuit. Top, electron microscopy image of an excitatory synapse. (Adapted from Südhof, 2017)

Even among excitatory or inhibitory synapses, the properties, plasticity and modulation of individual synapses lead to drastic variation in the way they process inputs. Thus, no general rule applies in terms of information transfer, and every single neuron integrates the information relayed by each of the unique synapses that it contains into a pattern of spikes, source for outputs that will greatly differ from one neuron to another, as well as from different synapses of a single neuron. To understand the synapse function at the network level, there is a need for a complete description of the synapse content, from the characterization of the proteins expressed and the number of copies for each protein, to the description of the

protein interactions and organization. A growing body of evidence suggests that proteins are **precisely organized** in synapses, with the presence of the right components at the right place, and that this specific organization is responsible for the synapse function at the network level. For instance, at excitatory synapses, a relationship between the receptor density and hippocampal synapse size has been demonstrated. Indeed, while the density of NR2B subtype of NMDA glutamatergic receptor is inversely proportional to the PSD area, GluA1 glutamatergic AMPA receptor subunit density increases with the PSD area (Shinohara, 2009). Interestingly, this receptor density to size relationship can be related to well-characterized synaptic plasticity mechanisms involved in learning and memory, such as long-term potentiation (LTP). On the other hand, inhibitory synapse organization seems to be highly entangled to synapse function too. Using single molecule localization microscopy, a recent study showed that the organization of gephyrin, a key scaffolding protein of inhibitory synapses, undergoes major changes upon inhibitory LTP, with an increasing proportion of multi-spot gephyrin clusters per synapse (Pennacchietti et al., 2017).

Furthermore, those findings highlight the **dynamic** compound of synapses (Choquet and Triller, 2013). Indeed, synapses are highly dynamic structures, with extensive variation from synapse formation to mature synapses, in terms of content and organization; and even among mature synapses depending on the activity levels. The synapse equilibrium is achieved through a specific sequence of events, in which protein dynamic plays a key role. Moreover, an emerging paradigm suggests that protein dynamics in the synapse regulates their function. An example illustrating this paradigm is the impairment of recovery from paired pulse depression (Heine et al., 2008), and of hippocampal-dependent learning tasks (Penn et al., 2017), observed when the GluA2 subunit of AMPA receptors are cross-linked at the cell membrane with specific antibodies.

Altogether, **synapse organization** and **dynamics** are indivisible, and part of a whole, as proteins organized through dynamic mechanisms, and this environmental organization impacts the diffusion of the proteins, highlighting the importance of studying both synapse composition and dynamics.

Recent advances in microscopy techniques with the development of super-resolution microscopy, allow the study of synapse organization and protein dynamics with a spatial resolution close to the one achievable with electron microscopy. Among those techniques,

the **single molecule localization microscopy** (SMLM) techniques became a tool of choice, widely used in life-sciences as they simply require regular fluorescence microscopy setups with only little modifications. To achieve single molecule localization microscopy, a sparse number of proteins of interest fused to specific fluorescent protein, or targeted by extrinsic fluorophores are imaged at a time, upon stochastic activation at a specific wavelength (usually in the near ultra-violet). Yet, all the different probes used to label proteins display specific properties, and it remains unclear how those properties might induce biases in the nanoscale organization and diffusion of the proteins of interest. For instance, probes of large **size** may alter protein localization or diffusion due to steric hindrance, while the number of binding domains, as referred to the **valence** of the probe, can lead to protein clustering.

In the introduction of this PhD thesis, different approaches allowing us to assess the organization of synapses and the dynamics of proteins are described with their specific advantages and drawbacks. Finally, the probes that can be used to tag proteins are addressed, as well as how this probe labeling may induce biases in the study of the organization and dynamics of the protein of interest.

1.1. Essentials of optical microscopy

Since the 17th century, optical microscopes have been widely used in biology to investigate living systems. The principle of optical microscopy is to manipulate the trajectory of light with a combination of lenses of different refraction index in order to obtain an image of bigger size of the object of interest (**Figure 3**).

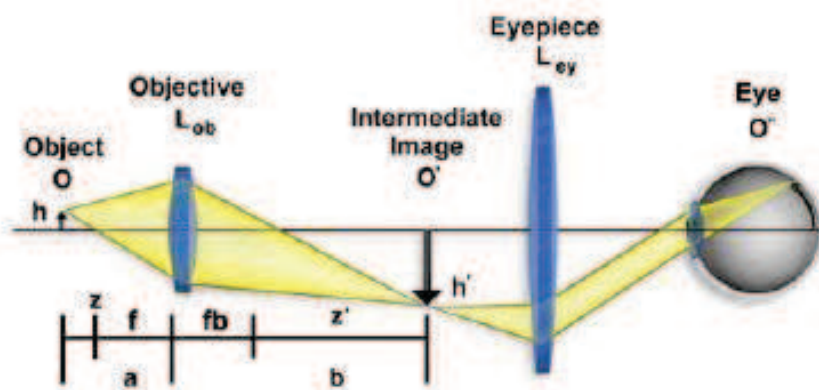


FIGURE 3: SCHEMATIC OF AN OPTICAL MICROSCOPE.
(Adapted from Davidson and Abramowitz, 2002)

Although electron microscopy provides much higher resolution (see the definition of resolution in [1.1.3.2 Resolution](#)), it relies on the use of very expensive and complex setups. Moreover, sample preparations required are long and cumbersome, leading to the death and alteration of the tissue.

With the development of fluorescent probes, optical microscopy has been widely improved in terms of contrast and specificity, from the primarily used absorption techniques, and therefore, remains a major tool of choice in the imaging toolbox.

1.1.1. Fluorescence fundamentals

The basis of fluorescence relies on the emission of photons rapidly, within nanoseconds, after the absorption of energy, generally under the form of light.

More thoroughly, the fluorescence mechanism can be broken down into 3 critical steps ([Figure 4](#)):

- (1) Initially, the molecule is in a normal, non-excited state called ground state (S_0).
- (2) Through the absorption of a photon, the molecule switches to an excited state, as its electrons transit to a higher energy level. Inside the same electronic energy state, the molecule reaches the lower vibrational state through vibrational relaxation. Depending on the energy of the photon, this excited state can be of different levels (S_1 or S_2), and the energy exchange between the molecule and its environment leads to a rapid relaxation towards more stable electronic levels. This phenomenon is called internal conversion.
- (3) Finally, the molecule leaves the excited state (S_1) by discharging energy and return to the ground state (S_0). Energy can be released through a non-radiative mechanism, for instance through thermic dispersion, or through a radiative mechanism: the **fluorescence**. The fluorescence corresponds to a radiative energy release through the emission of a photon. As energy has been dissipated in the environment in the process, the emitted photon is of lower energy. Again, the molecule undergoes vibrational relaxation to return to its fundamental vibrational state.

Two phenomena can be responsible for the extinction of the molecule fluorescence. While quenching is reversible, occurring through non-covalent binding with the molecular

environment, bleaching refers to all the processes that lead to a permanent loss of fluorescence.

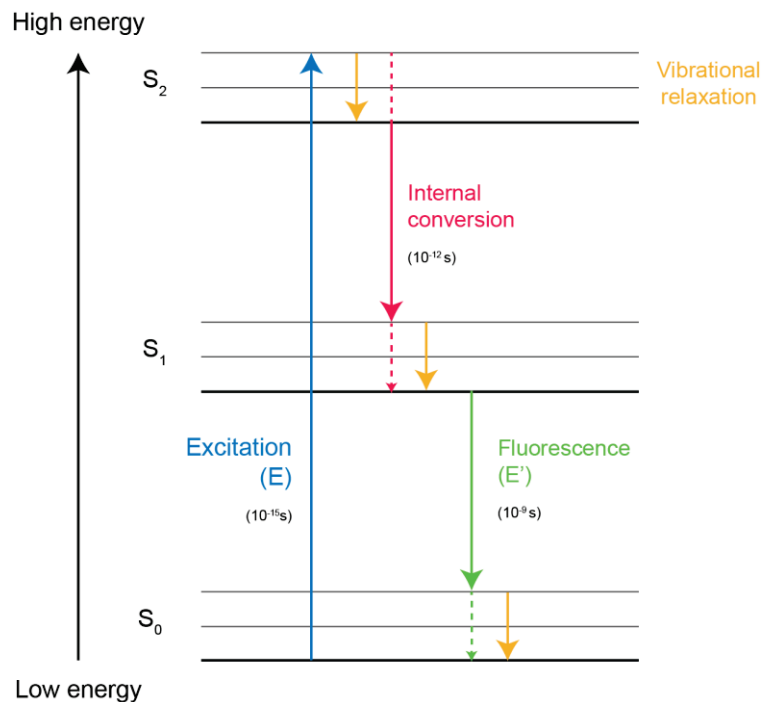


FIGURE 4: JABLONSKY DIAGRAM DISPLAYING THE ENERGY STEPS OF A MOLECULE DURING FLUORESCENCE.

The fluorescent molecule used in fluorescent microscopy can be of two types: intrinsic or extrinsic fluorophores. Intrinsic fluorophores are directly expressed by the living system, through the cellular machinery, and fused to the protein of interest, using recombinant proteins. While extrinsic fluorophores target the protein of interest through different labeling techniques. Those intrinsic and extrinsic fluorescent probes are detailed in [1.4. Probes for single molecule localization microscopy](#).

1.1.2. Fluorescence microscopy: contrast and signal to noise ratio

1.1.2.1. Image contrast

The **contrast** allows the distinction between the signal of interest and the noise coming from the background, and is described by:

$$\text{contrast} = \text{signal of interest} - \text{background noise}$$

The energy of a photon is inversely proportional to its wavelength, as defined by $E = h \times c / \lambda$ (where h is the Planck's constant, c the speed and λ the wavelength of light in a vacuum), therefore the emitted photon is of higher wavelength. This shift in the photon wavelength is

referred as the Stokes shift ($\delta\lambda_{Stokes}$) and can be calculated as the difference between the maxima emission and absorption wavelengths, corresponding to λ_{Em} and λ_{Exc} respectively (Figure 5):

$$\delta\lambda_{Stokes} = \lambda_{Em} - \lambda_{Exc}$$

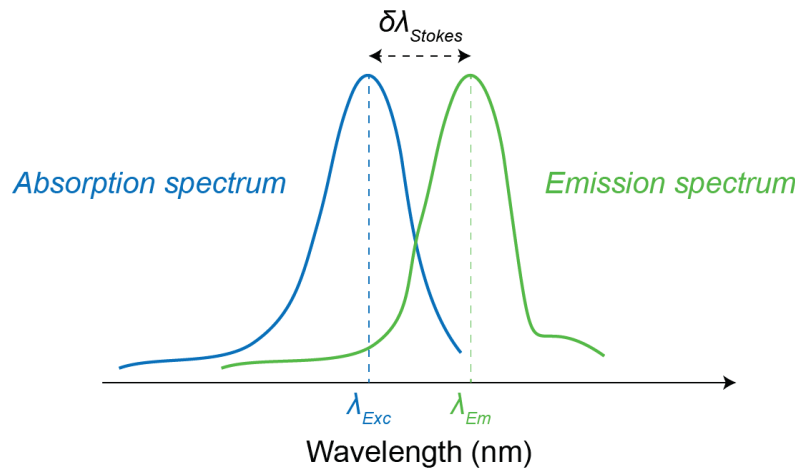


FIGURE 5: ABSORPTION AND EMISSION SPECTRA OF A FLUORESCENT MOLECULE.

The Stokes shift is fundamental in the optimization of optical microscopy provided by fluorescence, as higher contrast can be achieved by filtering the excitation/emission wavelength, compared with absorbance microscopy. The higher Stokes shift, the easier filtering, and therefore, better contrast. Epi-fluorescence microscopy uses the objective both to illuminate and image the sample. Through the use of specific filters and dichroic mirrors, the sample can be illuminated only with the excitation wavelength and higher wavelengths can be selected for the return of the light (Lichtman and Conchello, 2005) (Figure 6).

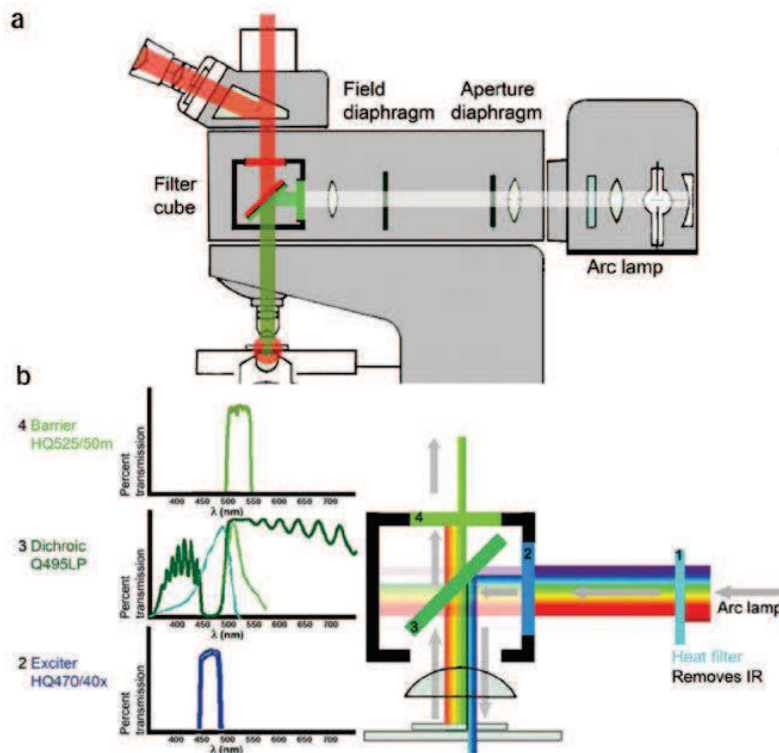


FIGURE 6: PRINCIPLE OF AN EPI-FLUORESCENCE MICROSCOPE.

(A) Schematic of an up-right epi-fluorescence microscope. The objective is used to focalize the excitation beam on the sample AND to image the specimen. A fluorescence cube composed of two filters, the dichroic mirror and barrier filter selectively illuminates the sample with the specific excitation wavelength, and prevents the excitation wavelength to reach the detector. The emitted photons are sent in all direction and a fraction is collected by the objective and send through the cube towards the detector.

(B) Schematic example of the cube designed by Chroma Technologies to excite and detect EGFP. (from Dobrucki and Kubitscheck, 2017)

In regular **epi-fluorescence**, the excitation beam is focused in the optical axis, on the back focal plan of the imaging objective. In this illumination mode, the whole specimen is illuminated homogenously and fluorescent molecule from above the focal plan are contaminating the signal. Fluorescence from out of focus molecules is a common source of background noise. In order to improve the precision of the system, the out of focus fluorescence can be reduced by changing the illumination mode of the microscope (Figure 7).

Around a specific incidence angle, the light illuminating the sample is totally reflected at the glass-sample interface, creating a non-propagative wave penetrating the sample, called evanescent wave, whose amplitude decreases exponentially with the distance from the interface. In this illumination mode, called TIRF for **Total Internal Reflection Fluorescence**,

only fluorophores located in the first 200-300 nm of the sample are illuminated (Axelrod, 2001). By moving the light beam to an angle close to TIRF, the sample can be illuminated on a thin and inclined light sheet, this oblique illumination allows to access fluorescent emission from a portion of the cell surface while limiting the background noise: this is the **Highly Inclined and Laminated Optical** (HILO) (Tokunaga et al., 2008). Finally, In **Selective Plane Illumination Microscopy** (SPIM), a thin light sheet can illuminate the sample from the side.

These types of illumination restrict the fluorescent signal to the focal plane, while maintaining fluorophores from other planes in a non-emitting state. Moreover, such approaches reduce the phototoxicity due to laser illumination.

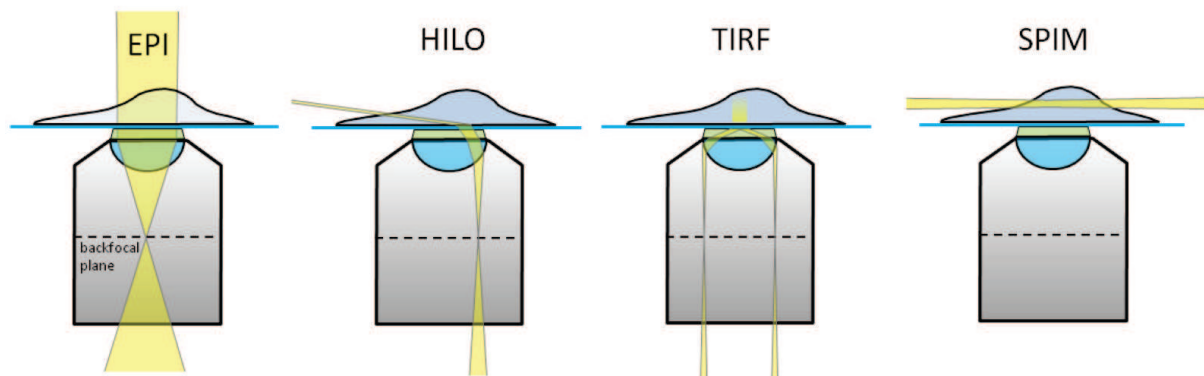


FIGURE 7: ILLUSTRATION OF EPI, HILO AND TIRF ILLUMINATION

In **epi-illumination** the whole specimen is illuminated by the excitation beam.

In oblique illumination or **Highly Inclined and Laminated Optical** (HILO), a thin and inclined light sheet illuminates the sample. The light sheet is achieved by moving the excitation beam to an angle close to total internal reflection.

Total Internal Reflection Fluorescence (TIRF) leads to an evanescent field, where the sample is illuminated within 100 - 200 nm at the specimen.

In **Selective Plane Illumination Microscopy** (SPIM), a thin layer of light sheet is illuminating the sample from the side.

(From Flottmann, 2014)

1.1.2.2. *Signal to noise ratio*

The signal quality can also be defined by the ratio between the signal of interest and the background noise. This ratio is referred to as the **signal to noise ratio** (SNR), and practically can be calculated by dividing the intensity of the signal of interest by the variance in the signal due to the noise. Consequently, as it is directly related to the number of photons collected from the signal and from the background, the SNR is highly impacted by the fluorophore properties, and can be improved by the illumination mode.

The brightness of the fluorescent molecule depends on two parameters: the extinction coefficient (ε), which corresponds to the probability of absorption of a photon by the fluorophore (expressed in $M^{-1}cm^{-1}$), and the quantum yield. The quantum yield is defined by the number of photons emitted over the number of photons absorbed. Therefore, it renders the probability of the fluorescent molecule to undergo a radiative desexcitation (fluorescent) once it has been excited.

1.1.3. Point Spread Function and resolution

1.1.3.1. Point Spread Function

The image of a single-point emitter through any optical imaging system is blurred due to the diffractive properties of light. The diffraction pattern of the light from this single-point emitter forms an object of fixed size composed of concentric rings of light surrounding a bright central spot called the Airy disk (**Figure 8**). The **point spread function** (PSF) is the function that measures the intensity of this single-point emitter image in each point of the space. Therefore, it corresponds to the minimum-size point source that can be observed by a microscope.

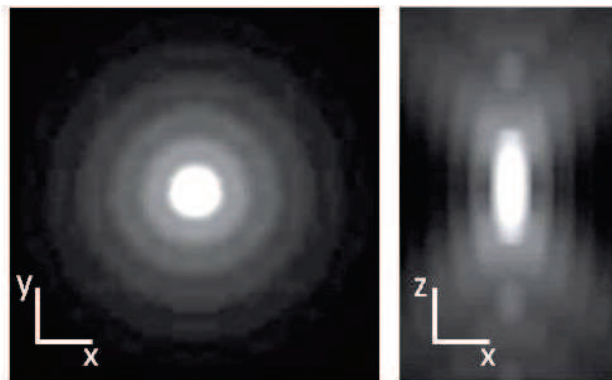


FIGURE 8: POINT SPREAD FUNCTION

Intensity profile of a single-point emitter (*left*) in the orthogonal plan and (*right*) parallel plan from the light trajectory.

(from Lagardère, 2018)

Different analytical functions allow the approximation of the PSF. The Bessel-based model is the most-accurate as the PSF formed by an ideal, aberration-free microscope, and is expressed by the following Bessel function of the first kind (J_1):

$$I(r) = I_0 \left(\frac{2J_1\left(\frac{2\pi NAr}{\lambda}\right)}{\frac{2\pi NAr}{\lambda}} \right)^2$$

where I_0 is the intensity of the Airy disk center, λ the wavelength of the single-point emitter, r the radius to the first dark ring, and NA the numerical aperture the imaging objective lens.

On the other hand, the Gaussian approximation of the PSF is simpler and faster to compute and is given by the following equation:

$$I(r) \cong e^{-\frac{r^2}{2\sigma^2}} \text{ with } \sigma = \frac{1}{2\sqrt{5}} \frac{\lambda}{NA}$$

This approximation shows that the Airy disk length increases with the wavelength and decreases with the numerical aperture of the imaging objective lens.

1.1.3.2. Resolution

The **resolution** of the system quantifies the ability to distinguish two emitting sources close from one another, and is intrinsically linked to the PSF of the microscope. More specifically, the resolution corresponds to the minimal distance that must separate two emitting point for them to be distinguishable. The Rayleigh criterion defined by Lord Rayleigh estimates that two point-sources are considered resolved, when the maximum of the first point-emitting PSF coincides with the first minimum of the other point-emitting PSF, which is expressed by:

$$d = 0.61 \frac{\lambda}{NA}$$

Where d is the effective resolution, λ the emitted light wavelength, and NA the numerical aperture the imaging objective lens. Effectively, with the wavelengths used for life-sciences imaging, the resolution achievable with epi-fluorescence has been defined as $\sim 200\text{-}250$ nm by Erns Abbe in 1973. With this resolution whole cells as well as organelles can be imaged and distinguished, however this limitation can be problematic when studying living system at the scale of the proteins as they are only few nanometers big (**Figure 9**).

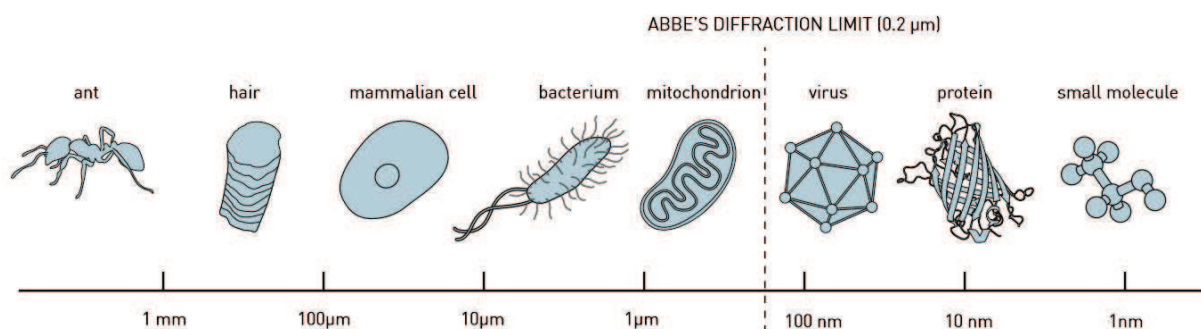


FIGURE 9: ILLUSTRATION OF THE DIFFRACTION LIMIT FOR VISIBLE LIGHT DEFINED BY ERNST ABBE. (from Fernholm and Jarnestad, 2014)

1.1.4. From microscope to nanoscope

Over the past decades, the scientific community continuously invested major efforts to bypass the resolution limitation imposed by light diffraction. Awarded by the Nobel Prize in Chemistry in 2014, Eric Betzig, Stefan W. Hell and William E. Moerner, managed to circumvent this diffraction limit developing new microscopy techniques and tools, gaining over two orders of magnitude in precision. Multiple approaches emerged, and commercial super-resolution microscopes are now available.

For now, two ways to achieve super-resolution with light microscopy exist: the illumination based super-resolution, and the emission based super-resolution (Eggeling et al., 2015; Galbraith and Galbraith, 2011; Huang et al., 2009; Toomre and Bewersdorf, 2010).

The illumination based super-resolution techniques, like STED microscopy (STimulated Emission Depletion) and SIM (Structure Illumination Microscopy), can achieve a lateral resolution of tens of nanometers by modulating the sample illumination to reduce focal spot-size, with an illuminated region smaller than the diffraction limit (Klar et al., 2000; Schermelleh et al., 2008). Those powerful techniques are particularly interesting when studying thick tissues, however, they require complex setups with high intensity pulsed lasers, whose phototoxicity can lead to sample damage.

On the other hand, emission based super-resolution microscopy takes advantage of fluorophore photophysics to achieve iterative activation of a small subset of the fluorescent population, and reconstruction of super-resolved images by super-imposing images sequentially acquired. Those techniques are referred to as **single molecule localization microscopy** (SMLM), and among them, the Photo-Activated Localization Microscopy (PALM) and the STochastic Optical Reconstruction Microscopy (STORM) have become very popular in the scientific community, allowing a spatial resolution from 10-50 nm, with commercially available setups (Betzig et al., 2006; Manley et al., 2008; Rust et al., 2006). Yet, they do not allow the study of in-depth tissues.

With the major breakthrough of super-resolution microscopy, the optical microscopy has now become nanoscopy.

1.2. Single molecule localization microscopy: protein organization and quantitative microscopy

With the groundbreaking contributions of super-resolution microscopy, it is now possible to study cellular mechanisms at their building blocks: the protein.

In this part, SMLM techniques will be detailed as well as their applications, for they are the most commonly used, and required only little modifications on a regular epi-fluorescence system.

1.2.1. Principle

Because of the diffraction of the light, molecules that are fluorescent at the same time cannot be distinguished from one another in a sub-diffraction volume, as the PSFs will overlap in the acquired image. In order to circumvent the diffraction limit, SMLM relies on the stochastic detection through iterative activation over time of sub-fractions of the fluorescent molecules. On each time-frame of the sequential acquisition, the now isolated emitting-points are precisely localized with nanometer-precision by assessing the center of the PSFs. This localization concept actually derives from a widely used technique since the 80s, known as the single particle tracking (SPT) (Thompson et al., 2002). The activation/localization process is repeated over many cycles until all fluorescent molecules have been acquired, and the super-resolved image is obtained by summing the localization points from each time-frame (**Figure 10**).

To achieve complete exhaustion of the signal, acquisitions may be quite long (from tens of minutes to hours), therefore, stage drift has to be corrected to obtain precise localizations. Piezo stages with closed loop feedback controls can be used, however, the easiest and most commonly used way to correct for stage drift remains the use of fiducial markers immobilized on the sample (**Figure 11**).

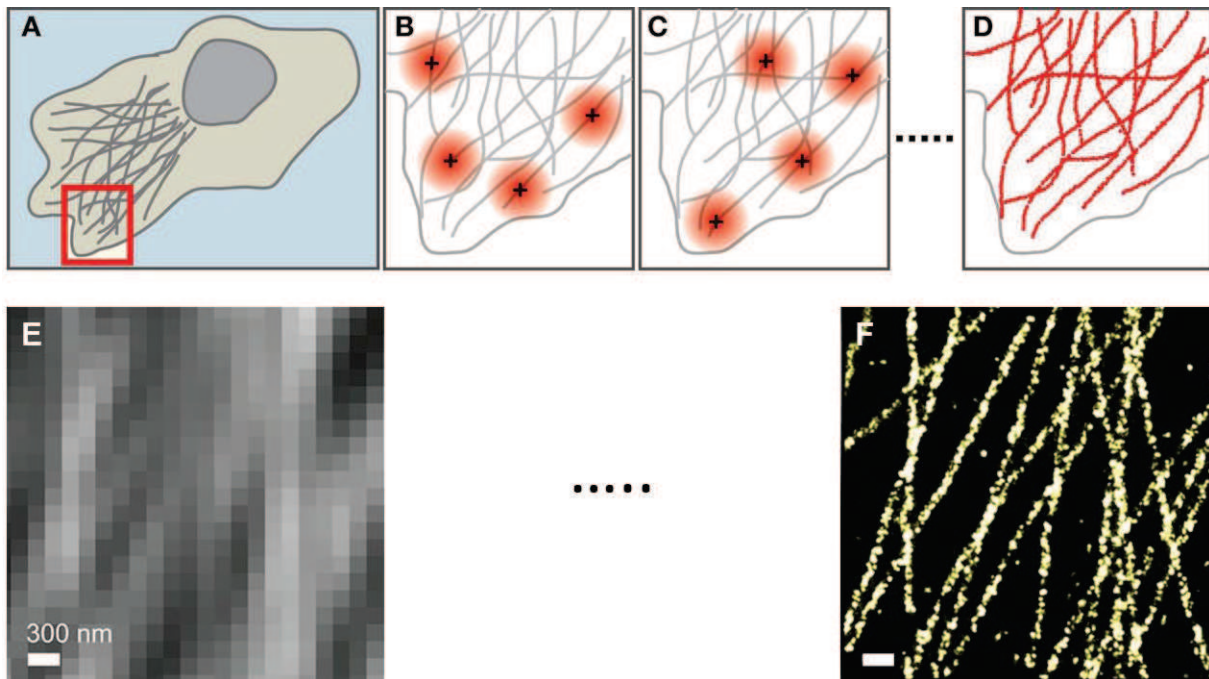


FIGURE 10: BASIC PRINCIPLE OF SINGLE MOLECULE LOCALIZATION MICROSCOPY.

(A) Schematic of SMLM experiment on a cell in which the structures of interest are labeled with fluorescent molecule stochastically activated and imaged. The red box indicates the area shown in panels B-D. (B) Schematic of an activation cycle: a sparse set of fluorophores is activated such that their images (large red spots) do not overlap. The image of each fluorophore appears as a diffraction-broadened spot, and the position of each activated molecule is determined by fitting to find the centroid of the spot (black crosses). (C) on each activation cycle a different set of fluorophores is activated, and their positions are determined as before. (D) After exhaustion of the signal, high resolution image is constructed by plotting the measured positions of the fluorophores (red dots). The resolution of this image is not limited by diffraction but by the accuracy of each fluorophore localization and by the number of fluorophore positions obtained. (From Bates et al., 2013)

Example of single molecule localization microscopy performed on microtubule of BS-C-1 cell, (E) conventional fluorescence image, and (F) STORM image of microtubule immunostained with Cy3-Alexa647-conjugated antibodies. (Adapted from Bates et al., 2013)

The privileged method to segment individual detection relies on the Gaussian analysis, as it provides the best localization performance. The center of the molecule fluorescence emission is determined by fitting with a Gaussian approximating the PSF intensity profile (Betzig et al., 2006; Sergé et al., 2008) (Figure 11). Nevertheless, despite its good localization performance, this technique turns out to be very time consuming, each localization being computed one at a time.

An alternative approach for localization of single detection is the wavelet segmentation, with wavelet maps decomposition of each acquisition plan (Izeddin et al., 2012) (Figure 11). The strong advantage of this method relies in its fast computation (several minutes against hours with Gaussian fittings), with minimal loss of localization detections: comparison on simulated

datasets showed that the wavelet segmentation tends to be better at localizing molecule on acquired images with low signal to noise ratio, but gives rise to a few more false positive detections than the Gaussian fitting (Izeddin et al., 2012).

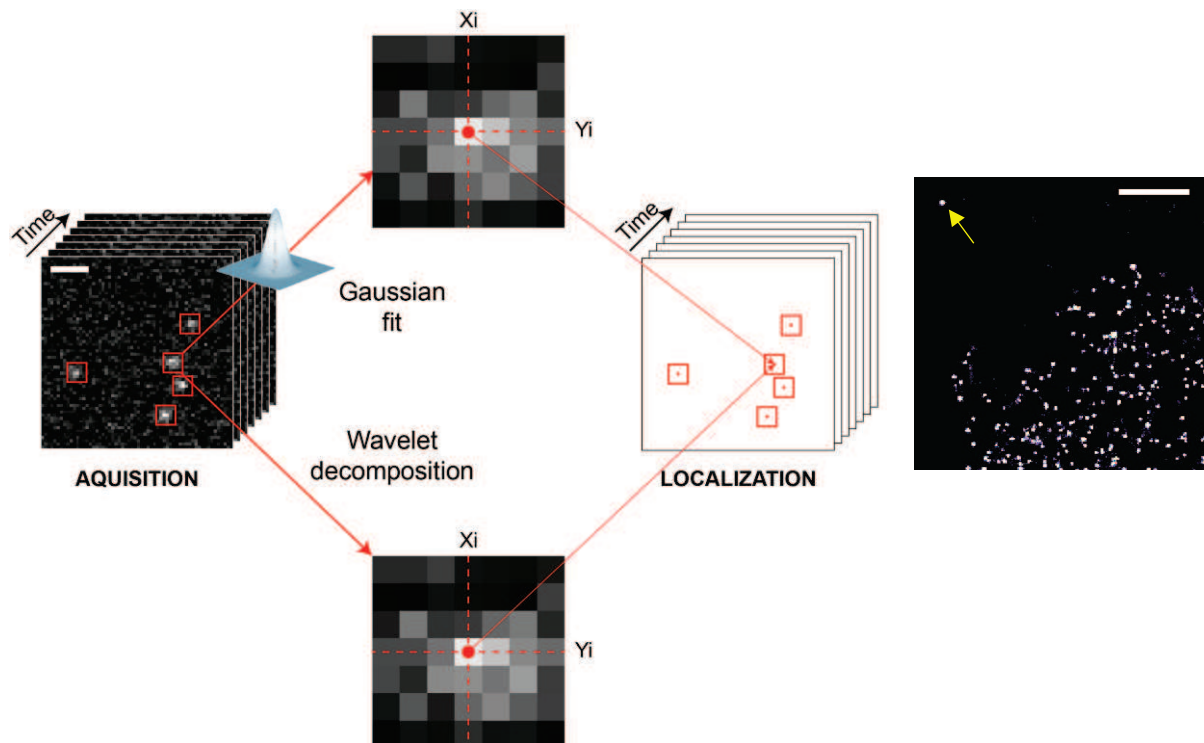


FIGURE 11: FRAMEWORK FOR LOCALIZATION, AND SUPER-RESOLVED IMAGE CONSTRUCTION FROM SINGLE MOLECULE DATA.

SMLM experiments are divided into 3 steps: the acquisition (left), localization of fluorescent molecules (middle), and superposition of localization points on the pointillist image (right) (scale bar: 2 μm)

Segmentation of the detections: each plane of the acquisition dataset is analyzed to extract coordinates of all fluorescent molecules, using different computation methods such as Gaussian analysis (top), and wavelet segmentation (bottom). After all fluorescent molecules have been imaged, corresponding localization points are summed to form the super-resolved pointillist image. (Right) example of a super-resolved image, with its fiducial marker (yellow arrow).

(Inspired by Sibarita, 2014)

1.2.2. Localization precision and localization accuracy

1.2.2.1. Localization precision

The **localization precision** can be measured by calculating the standard deviation of the detected localizations. It describes the spread of estimates $x_{p,i}$ around a mean value \bar{x}_p of the true position coordinate x_p of a particle measured multiple times, commonly expressed by (Deschout et al., 2014):

$$\sigma_x = \sqrt{\frac{1}{n-1} \sum_{i=1}^n (x_{p,i} - \bar{x}_p)^2}$$

where n is the number of estimates.

The real particle position (x_p, y_p) is therefore estimated with a lateral **localization precision** of (Deschout et al., 2014):

$$\sigma_{xy} = \sqrt{\sigma_x^2 + \sigma_y^2}$$

The precise localization of each emitting single molecule mainly relies on the signal to noise ratio per localization, which depends on the number of collected photons, image sampling and background noise (Sibarita, 2014). In the case of a PSF approximated by a Gaussian of standard deviation s , **localization precision** is limited by (Deschout et al., 2014):

$$\sigma_x \geq \frac{s}{\sqrt{N}}$$

where N is the **number of photons collected**.

From the sample, auto-fluorescence and out-of-focus fluorescence strongly impact the SNR, and therefore, contribute to a degradation of the localization precision. While out-of-focus fluorescence can be addressed by varying the illumination mode, the use of bright probes may render the auto-fluorescence input negligible. Moreover, background auto-fluorescence is progressively reduced at higher wavelength and quenchers can be used to minimized fixative induced auto-fluorescence.

1.2.2.2. *Localization accuracy*

The lateral **localization accuracy** (Δ_{xy}) quantifies the standard deviation between the true position of the particle (x_p, y_p) and its mean measured position (\bar{x}_p, \bar{y}_p) (Deschout et al., 2014):

$$\Delta_{xy} = \sqrt{(x_p - \bar{x}_p)^2 + (y_p - \bar{y}_p)^2}$$

The **localization accuracy** is insensitive to the number of photons, therefore, there is no fundamental limit in the achievable accuracy. However, this accuracy relies on other factors that are either specific to the localization algorithm or probe-specific. For instance, the

distance between the fluorescent marker and the molecule of interest, or the emission isotropy of the fluorescent molecule strongly impact the accuracy of the localization.

1.2.3. Single molecule localization microscopy techniques

The SMLM techniques differ in the way they achieve the isolation of single molecule emissions. In this part, 2 major SMLM techniques are described: the PALM and STORM. While the PALM relies on the fusion of the molecule of interest with fluorescent protein that can be photo-activated or photo-switched, the STORM takes advantage of the fluorescence properties of organic dyes.

1.2.3.1. PALM

In 1997, W. E. Moerner discovered a variant of the Green Fluorescent Protein (GFP) that could be turned on and off at will, thus demonstrating that it was possible to optically control the fluorescence of individual molecules (Dickson et al., 1997).

This discovery was the cornerstone of the following work performed by E. Betzig, leading to the development of a new fluorescence microscopy technique that revolutionized nanomolecular studies: the **photo-activated localization microscopy** (Betzig et al., 2006).

In **PALM** single molecule localization is obtained by stochastically activating a small subset of photo-activable/switchable fluorescent protein (PAs/PSs) fused to the protein of interest among a dense population of inactive ones (Betzig et al., 2006). PAs/PSs change their emitting spectrum upon illumination with near-ultraviolet (UV) light (**Figure 12A**), by adjusting photoactivation laser power (UV), it is possible to control the fluorescent molecule density in order to resolve individual protein localization (Manley et al., 2008). The cycle of activation, imaging, localization is repeated until all fluorescent molecules are bleached, and the combination of all detections forms a super-resolved pointillist image of higher resolution (**Figure 12C**).

By observing only a subset of fluorescently visible proteins over time, such single molecule localization techniques bring the spatial resolution down to only 20-50 nm, with a localization accuracy of 2-25 nm (Betzig et al., 2006).

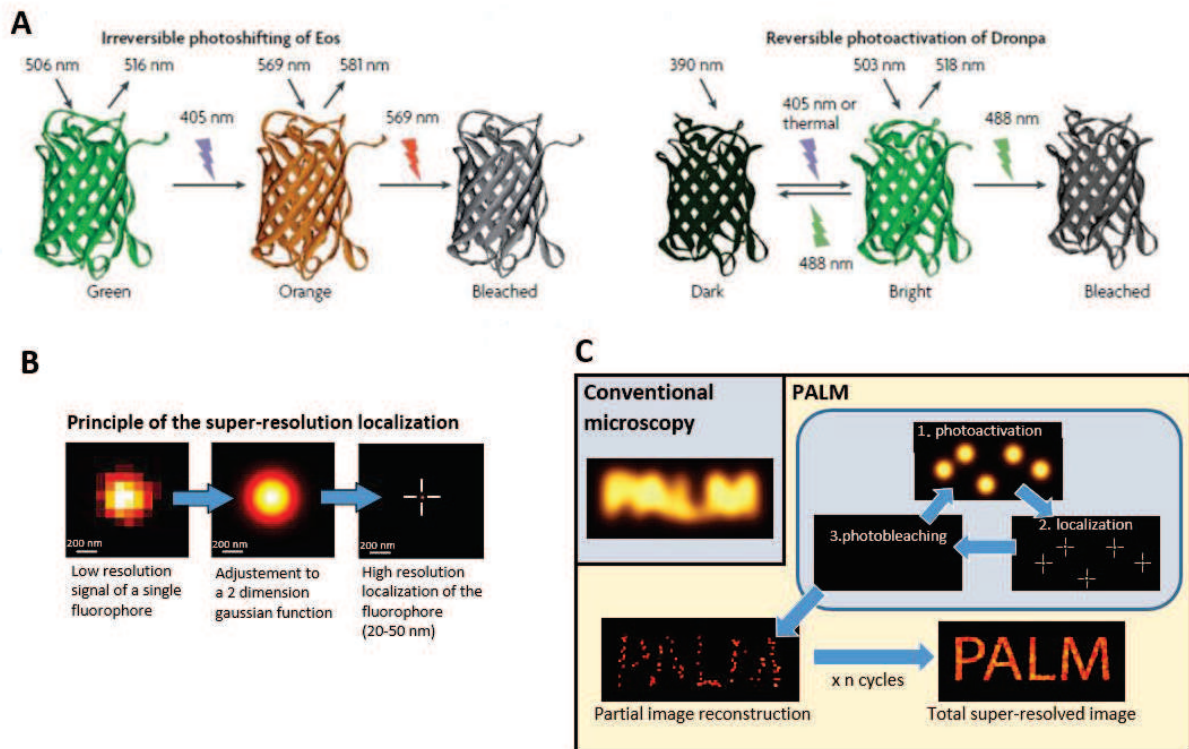


FIGURE 12: SUPER-RESOLUTIVE LOCALIZATION WITH PALM TECHNIQUE

(A) Fluorescence state of photoswitchable and photoactivable proteins. (Left) Example of a photoswitchable probe: Initially emitting at 516 nm, mEos is photoconverted upon 405 nm activation to emit at 581 nm, and bleached using 569 nm illumination. (Right) Example of a reversibly photoactivable probe, initially in the dark state, Dronpa is visible in the green channel upon 405 nm activation, and can go back to the dark state with 488 nm illumination. Multiple photoactivation cycles are achievable before protein photobleaching. (From Lagardère, 2016).

(B) Basis of super-resolutive localization. **(C)** Schematic of the PALM technique and overview of the improved resolution with PALM with regard to conventional microscopy. (From Orre, 2016).

1.2.3.2. STORM/dSTORM

STORM, on the other hand, relies the immersion of organic dyes in reducing agents to allow the photoconversion of fluorophores using light of different wavelengths (Rust et al., 2006). Like for PALM, the pointillist super-resolved image in STORM is acquired by combining the localizations obtained in series of imaging cycles until the fluorophores are photobleached; in each acquisition, only a fraction of the fluorophores in the field of view are switched on, making them optically resolvable.

However, STORM does not rely on molecule fluorescence but phosphorescence (**Figure 13**).

Depending on the incident photon energy, excitation of a molecule can lead to a change in its electronic state. Indeed, many fluorophores have their singlet-excited energy level

overlapping with the energy levels of the triplet state, which favor intersystem crossing. The molecule return to a singlet state through the emission of a photon is called **phosphorescence**. The emitted photon is of even lower energy as the one in the fluorescence phenomenon, therefore, of higher wavelength (Figure 13).

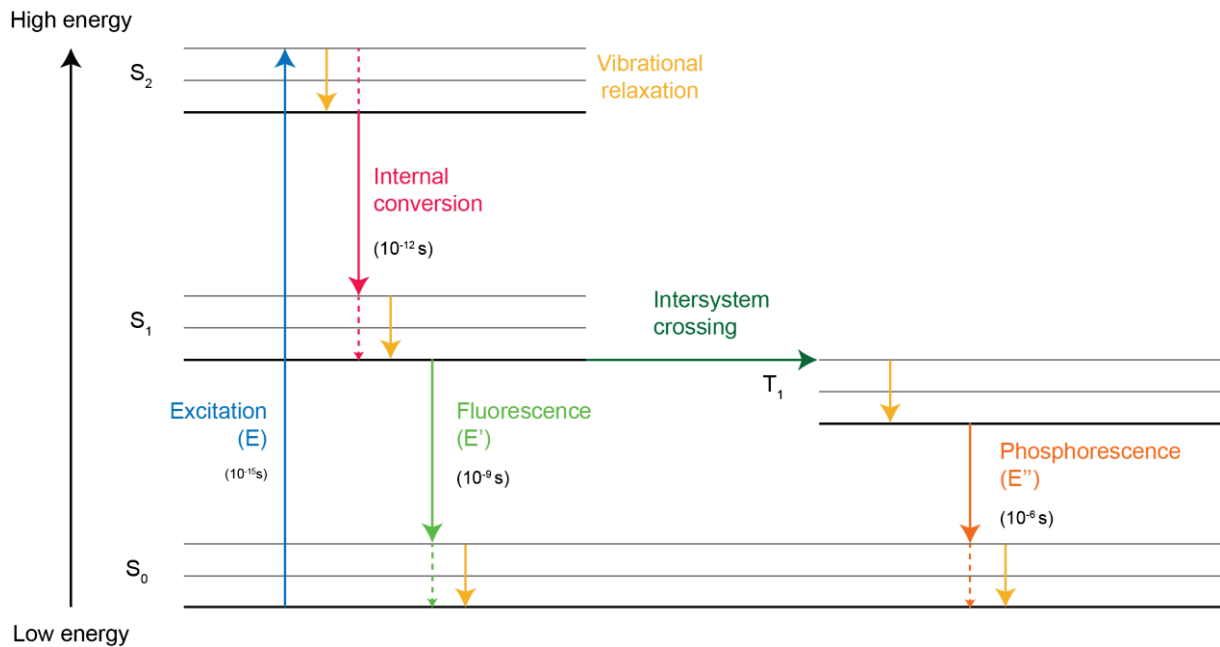


FIGURE 13: JABLONSKY DIAGRAM DISPLAYING THE ENERGY STEPS OF A MOLECULE DURING FLUORESCENCE AND PHOSPHORESCENCE.

The STORM technique takes advantage of the timescale of those phenomena. Indeed, while fluorescence happens in a range of nanoseconds, the phosphorescence takes microsecond to occur, and during that time-lapse further photon absorption can lead to triplet-triplet transitions delaying even further the light emission by moving the molecule to higher triplet state. Moreover, STORM specific reducing agents react with the fluorophores in triplet state forming a molecule in stable dark radical state, which have even longer lifetime (from seconds to hours). The bound between the reducing agent and the fluorophore can be broken using 405 nm laser, leaving the molecule free to return to the stable singlet state through phosphorescence. By carefully adjusting the 405 nm laser, only a sparse set of fluorophores can be imaged, ensuring single molecule localization.

Interestingly, the triplet state is more sensitive to bleaching as electron rearrangement between the triplet molecule and molecule in the environment can occur. Moreover, electrons can be exchanged with oxygen in the medium, leading to the formation of oxygen

radicals that are highly reactive and a major source for photobleaching. In STORM experiment, enzymatic oxygen scavenging system are often used to limit the fast photobleaching caused by oxygen radicals.

Originally, STORM was developed using a combination of orange and red-emitting carbocyanine dyes, Cy3 and Cy5, forming an activator-reporter pair. Indeed, Cy3 can be used to switch Cy5 between the fluorescent and dark states in a controlled and reversible manner. In this approach, the red laser light (~647 nm) stimulates the fluorescence emission from Cy5, and with proper reducing agent and laser power, switches the dye to a non-emitting triplet state, the dark state. Then, excitation of Cy3 results in a non-radiative transfer of energy to Cy5, stimulating its recovery from the dark state, a process referred to as activation. Alternatively, **dSTORM** (direct STochastic Optical Reconstruction Microscopy) differs from the parent technique by employing conventional carbocyanine dyes and does not rely on the use of the activator-reporter pair. The red laser light (~647 nm) is used to stimulate and switch the fluorophore to the dark state, and the dye goes back to the emitting state stochastically.

1.2.4. Applications

With the development of SMLM techniques, studies of synaptic protein organization became more and more thorough. New algorithms are constantly being developed to better characterize the organization of the synapse. With a lateral resolution close to the one achievable with electron microscopy, SMLM allows the precise characterization of protein organization. The differential organization of synaptic proteins can be compared: for instance, β -neurexin1 synaptic partners displays different organization as neuroligin1 seems to be more diffused than LRRTM at synapses (Chamma et al., 2016a). Formation of nanodomains of AMPA receptors has been identified, as well as pre-/post- alignment of synaptic partners (Haas et al., 2018; Nair et al., 2013).

Besides their evident contribution in protein organization characterization, SMLM has been used in many studies to assess relative and absolute quantification of proteins (Durisic et al., 2014a; Finan et al., 2015; Haas et al., 2018; Levet et al., 2015; Nair et al., 2013; Patrizio and Specht, 2016; Patrizio et al., 2017; Renz et al., 2012; Specht et al., 2013).

1.2.4.1. *the single molecule localization microscopy: a new tool for relative and absolute quantification*

Synapses are very complex structures, where protein concentration is extremely high and lies in a very confined and compartmentalized space, forming dynamic molecular platforms at the cell surface. As many biological mechanisms rely on multifarious systems, even small changes in the synapse content can lead to major alteration of the synaptic transmission. For instance, changes in the composition or density of the vesicle machinery at the pre-synapse can be responsible for variation in the release probability. At the post-synapse, the number of receptors available to conduct the information is directly correlated with the synapse strength. Moreover, receptor efficacy depends on their conformational states, and some receptors even requires oligomerization to be active (example, Fibroblast Growth Factor receptor dimerization in response to ligand binding leading to their activation and/or internalization). In this view, just like encased Russian dolls, numbers count from the network level (number of synapses), to the number of proteins at the synapse level, including the number of subunit inside a receptor complex.

Different approaches, are available to access quantitative information, ranging from electrophysiology (for ionic channels) to immunogold labelling (Patrizio and Specht, 2016). For instance, absolute and relative proteomic quantification of synaptic components can be achieved from enriched fraction purification, using mass spectrometry. However, the main drawbacks of proteomic strategies are the loss of components during biochemical purification, and the loss of cell type and synapse specificity. Immunogold labeling provides information about synapse enrichment with the high spatial resolution characteristic to electron microscopy, but it is a very time-consuming technique, and can lead to an alteration of the structure morphology due to aggressive fixation.

In this part, I will detail different applications of SMLM and how it allows to assess protein number. Quantification can be either relative or absolute. Relative comparison of protein number, for instance inside a protein complex or between to experimental conditions is referred as **relative quantification**, while **absolute quantification** aims at characterizing the absolute number of proteins inside a structure.

When aiming at protein quantification, several pitfalls and biases are to be considered. Basically, counting errors fall into two categories: **overcounting** and **undercounting** of the proteins of interest, which are summarized in [Figure 15](#).

To avoid undercounting of the proteins, every probes must have been exhaustively imaged during the single molecule localization microscopy imaging (Durisic et al., 2014b). One way to ensure that the imaging period is long enough is to plot the cumulative frequency of all the single molecule localization detections in each frame: the cumulative curve should increase slowly, and reach a plateau once most of the fluorophores have been imaged (Durisic et al., 2014b).

In terms of absolute quantification, photophysical properties of fluorophores are still ill-defined, fluorophores are usually active, therefore detected, for several consecutive frames, and the precision of the localization is submitted to the number of emitted photons, which is variable. Consequently, the number of detections constituting the pointillist image is not equal to the number of fluorophores present, each fluorescent molecule being in fact represented by a small cluster of points. To achieve absolute quantification, bursts of detection must be translated into absolute molecule number. To overcome these difficulties, calibration standards with a known number of fluorophores can be used (Finan et al., 2015). Relying on this technique, Renz and colleagues assessed relative expression stoichiometry of PA-GFP and PA-Cherry tagged subunits of rat hepatic lectin using a PA-GFP-PA-Cherry double construct as an internal ruler for a 1:1 ratio (Renz et al., 2012).

On the other hand, Specht and colleagues used the photobleaching step counting technique developed by Ulbricht and Isacoff (Ulbricht and Isacoff, 2007) to translate the peak intensities of a small subset of Dendra2-tagged proteins in absolute numbers, which they could then use to normalize the intensity of a given cluster, obtaining the absolute number of scaffolding proteins present (Specht et al., 2013).

Another important parameter to achieve absolute quantification, is the stoichiometry of the probe-target interaction. Indeed, even if antibodies are interesting probes since they can target endogenous proteins, polyclonal antibodies that can bind to the same target at the same time give rise to over-labeling and therefore overcounting, while monoclonal divalent antibodies might lead to undercounting through artificial clustering, or because of the steric hindrance caused by their large size.

When it comes to single molecule localization, a wide variety of probes are available, which belongs to two distinct categories: the reversibly photoswitching (PS) probes and irreversibly photoactivable/convertible (PA/PC) probes. Indeed, as opposed to PA and PC (e.g. PA-GFP, PA-Cherry, dendra2, mEOS2... used for PALM experiment), PS are called reversibly as they can be switched on and off many times, falling in this category are organic fluorophores used for STORM and dSTORM (e.g. Cy5, Alexa647...), and the photochromic fluorescent proteins (e.g. Dronpa) used in PALM (**Figure 14**). As a result, the same fluorophore leads to multiple detection points, even with optimized frame rate, and therefore, smoother images can be obtained. However, the fact that the dye can be cycled hundreds of times before being permanently photobleached, makes the pointillist image more challenging to normalize to obtain the absolute number of fluorescent proteins. Finan and colleagues propose different calibration standards fused to an alexa647-conjugated SNAP-tag to normalize dSTORM images, they used those rulers to quantify the number of Nup107 copies inside nuclear pores (Finan et al., 2015). To be noted that, as blinking of the fluorophore is achieved by “pumping” with high laser power, one needs to use exact same experimental settings in order to have the same fluorophore photophysics.

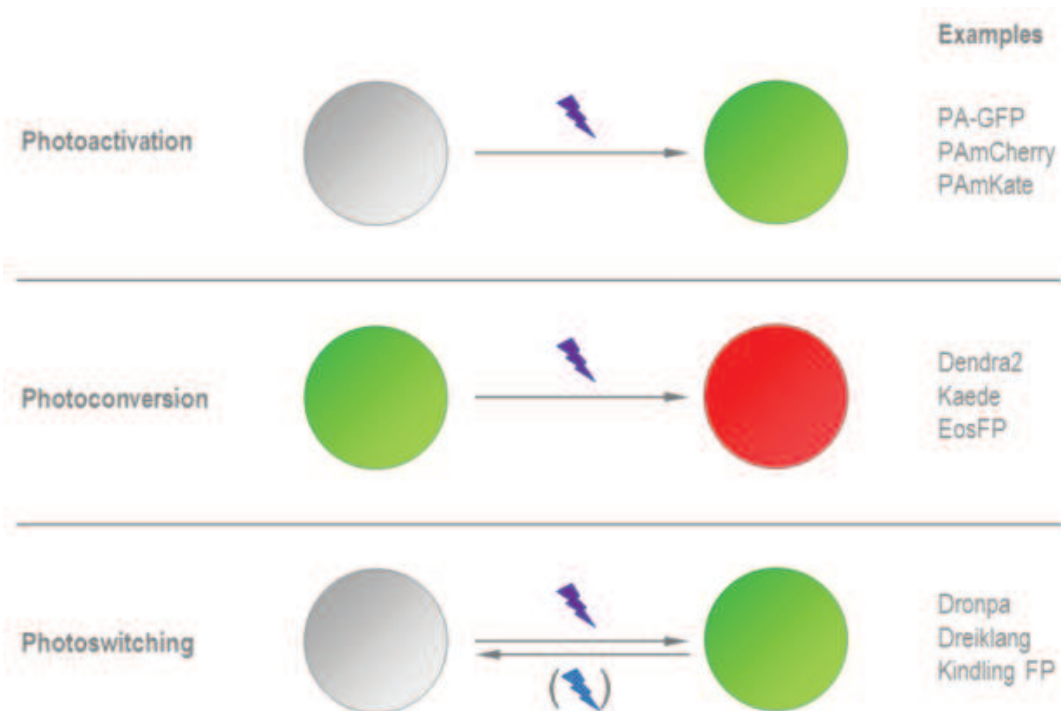


FIGURE 14: SCHEMATIC OF THE DIFFERENT TYPES OF PROBES

Schematics of probes undergoing photoactivation (top), photoconversion (middle), and photoswitching (bottom).

(from <https://www.leica-microsystems.com/science-lab/photoactivatable-photoconvertible-and-photoswitchable-fluorescent-proteins/>)

Yet, even PAs can undergo transitions to non-fluorescent off triplet states, resulting in a blinking of the fluorescence, translated into multiple appearance of the same molecule during the acquisition, which can lead to overcounting of the proteins.

Recently, some studies have proposed solutions to correct for multiple detections according to their temporal and/or spatial distribution, based on the analysis of single fluorophore behaviors (Annibale et al., 2011; Durisic, Cuervo, & Lakadamyali, 2014; Fricke et al., 2015). For instance, the blinking of PAs can be accounted for by taking advantage of the time dependence of the blinking and photoactivation. Indeed, by carrying out the photoactivation slowly over a long period of time, then the blinking events are closer in time compared to the photoactivation, and detections from blinking can be grouped together (Annibal et al., 2011). Alternatively, various mathematical algorithms such as the pair-correlation function have been used to analyze the spatial distribution of fluorophores (Sengupta et al., 2013) to identify non-random patterns in the pointillist image. Another algorithm, the SR-tesseler, was recently developed to identify spatially defined clusters in an unbiased fashion (Levet et al., 2015). This

algorithm is based on the Voronoï tessellation, subdividing space into a number of polygonal regions centered on a set of points, called seeds. Applied to single molecule localization microscopy, this method allows the precise, robust and automatic quantification of protein organization (Levet et al., 2015).

Undercounting	Overcounting
<ul style="list-style-type: none"> • Undetected fraction of molecule (non-mature fluorescent protein, bleaching prior to imaging, incomplete labeling...) • Multivalent probes • Simultaneous activation of multiple fluorescent molecule from the same cluster (below diffraction limit) 	<ul style="list-style-type: none"> • Fluorescence detected on a longer period than the acquisition rate (on multiple frames) • Multiple <i>Off time</i> per fluorescent molecule (blinking, reversible photoswitch...) • Multiple fluorescent dye per probe (alexa647...) • Overlabeling with polyclonal antibodies

FIGURE 15: SUMMARY OF THE DIFFERENT BIASES THAT CAN LEAD TO UNDERCOUNTING OR OVERCOUNTING OF THE MOLECULE OF INTEREST.

1.3. Fluorescence microscopy and protein dynamics

1.3.1. FRAP

To measure the mobility of membrane proteins, several complementary strategies are available. The oldest technique is the **Fluorescence Recovery After Photobleaching (FRAP)** (Figure 16). This method consists in the irreversible photobleaching of fluorescent proteins by a strong laser in a region of interest, creating two populations (one fluorescent and one bleached) in spatially distinct compartments (Figure 16B). The diffusion of the two populations leads to a recovery of fluorescence in the region of interest, as the unbleached proteins enter (Figure 16C,D). Fluorescence recovery depends on multiple factors that can be extracted with appropriate mathematical models or simulation: the protein mobility and its availability in the surroundings, the presence of free binding slots in the bleached region, and the association/dissociation rate constants of the protein of interest complexes (Reits and Neefjes, 2001).

With this technique, **long dwell times** can be accessed, in the range of minutes to hours. However, biological events being inhomogeneous in terms of molecule behaviors and kinetics,

as they are generally mediated by a small number of molecules, ensemble techniques such as FRAP do not access individual protein behavior, and lead to a **loss of heterogeneity**.

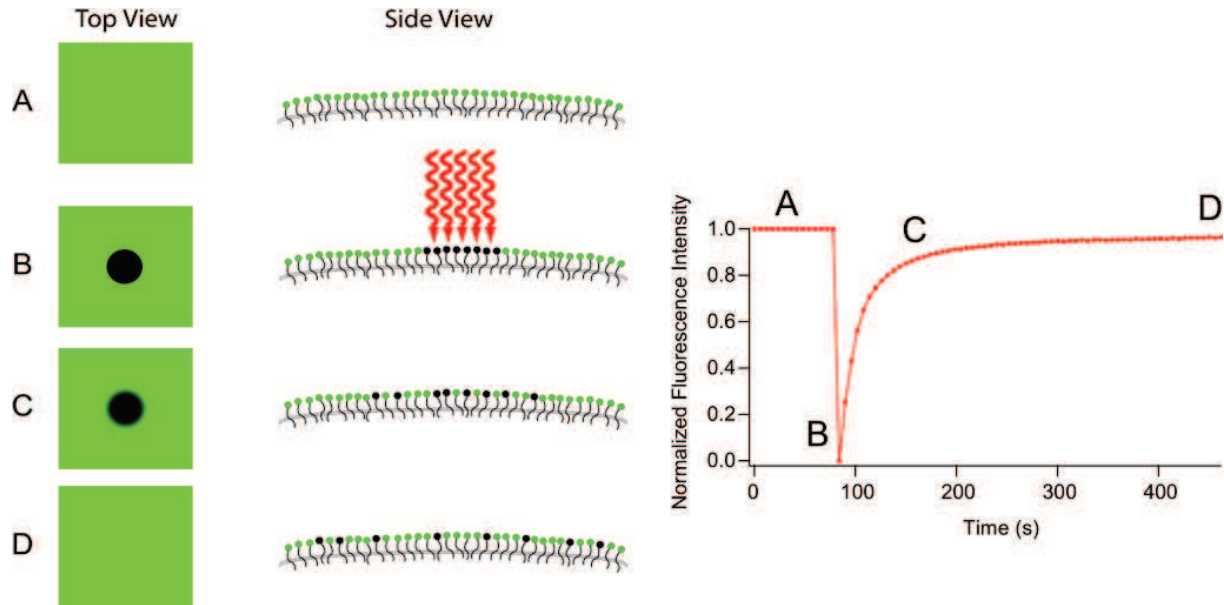


FIGURE 16. PRINCIPLE OF FRAP TECHNIQUE

(Top) (Left) Schematic of the top view, and (right) side view of the plasma membrane with fluorescent trans-membrane proteins, **(A)** before photobleaching, **(B)** during photo-bleaching, **(C)** during fluorescence recovery, **(D)** and when the fluorescence intensity is stabilized. (Bottom) Graph of the normalized fluorescence intensity, with the 4 steps of a FRAP acquisition.

(modified from: <https://commons.wikimedia.org/w/index.php?curid=5507867>; MDougM)

1.3.2. Single particle tracking

1.3.2.1. *The single particle tracking concept*

Single particle tracking (SPT) techniques use localization of individual molecules at high acquisition rate, in order to detect in each frame, the precise position of the fluorescent protein, and finally, reconstruct its trajectory by reconnecting each position with sophisticated image analysis methods. Nevertheless, because of the diffraction properties of light, the resolution of relative localization of individual fluorescent proteins is impossible with conventional microscopy techniques. To work around this optic limitation, SPT was primarily relying on the use, at low density, of nanoparticle such as nano-gold particles and, more recently quantum dots (QD) (Michalet et al., 2005; Pinaud et al., 2010; Saxton and Jacobson, 1997). Their high photostability was enabling the tracking of molecule over long period of time (from minutes to hours). The precision of the detection is then depending on the total number

of photon detected and can be as low as 10 nm (Pinaud et al., 2010). Yet, their relatively large size and multivalence may have strong impact on protein diffusion and behavior. Indeed, a twofold to four-fold decrease in diffusion coefficient (D) can be observed with nano-gold based SPT with regards to FRAP (Saxton and Jacobson, 1997). Moreover, the **low labeling density** used in traditional SPT techniques to reach individual detections strongly limits statistic.

With the recent breakthrough of super-resolution microscopy, new microscopy techniques are now available to assess the diffusion of single molecule.

The combination of PALM with the SPT technique, gives rise to the **sptPALM** (Manley et al., 2008), allowing to monitor recombinant protein behavior at **high density** (over a 1'000 trajectories in the range of a minute). Yet, as it relies on the expression of recombinant protein, the position and size of the PA/PS fluorescent tag, may alter diffusion, addressing, and overall function of the targeted protein, moreover, fluorescent proteins presenting fewer double-bound than organic dyes, limited number of photons are emitted, reducing localization precision of the molecule of interest.

Based on the stochastic labeling at low density of the membrane targets by fluorescent probes, the **uPAINT technique (universal Point Accumulation Imaging in the Nanoscale Topography)** allows **high density SPT**, with the strong advantage to be able to track endogenous proteins, through specific antibodies (Giannone et al., 2013a) ([Figure 17](#)). In this approach, the labeling density of the sample is adjusted by varying the concentration of probes in solution. Probes are conjugated to organic fluorophores, which hold photophysical properties assuring signal more intense than photoactivable fluorescent protein, with a wide range of the color spectrum available. However, labeling specificity is primordial to ensure the least non-specific binding of the free fluorescent ligands in solution during the acquisition.

While nano-gold particles and QD allow the tracking of protein over long period of time, high density SPT such as sptPALM and uPAINT technique, provide shorter trajectories but higher statistics.

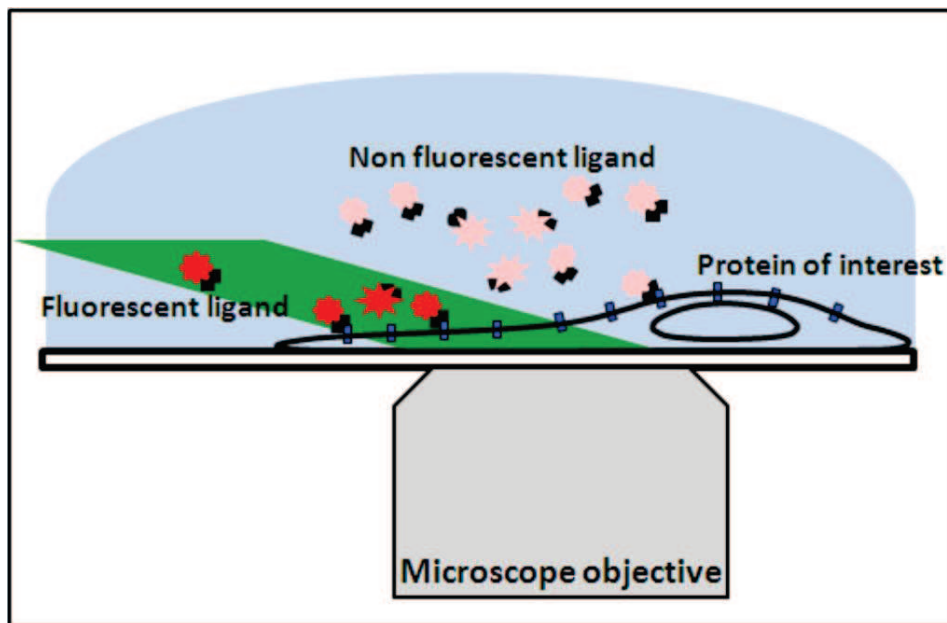


FIGURE 17: PRINCIPLES OF THE UPAINTECHNIQUE.

uPAINT is based on the real-time imaging and tracking of single fluorescent ligands while they label their membrane biomolecules targets. A low concentration of fluorescent ligands is introduced in the extracellular medium such that a constant rate of membrane molecules is being labeled during the imaging sequence. Oblique illumination of the sample is used to excite predominantly fluorescent ligands, which have bound to the cell surface while not illuminating the molecules in the above solution.

(From Gregory Giannone et al., 2013).

1.3.2.2. *The single particle tracking: detection and trajectory reconstructions*

Trajectory reconstruction is divided in two critical steps: the segmentation of individual fluorophore detected, and the reconnection of the detected objects frame by frame (Sibarita, 2014) (Figure 18).

The same algorithms can be used to segment individual detections from regular PALM and STORM experiments, as those algorithms actually derives from the one that have been used for over 2 decades in the SPT field.

Nevertheless, despite the good localization performance of the Gaussian-based fits, some other segmentation methods may be preferred, especially when it comes to high density SPT. Indeed, each localization being computed one by one, this technique turns out to be very time consuming. With the development of high density SPT, new techniques of segmentation were required, to be able to detect and reconnect thousands of trajectories per minute of

acquisition. Therefore, alternative methods such as the wavelet segmentation may be preferred (Izeddin et al., 2012).

When it comes to trajectory reconstruction of high density SPT dataset, the main limitations are that false reconnections may happen due to the high density of the localizations. Wavelet segmentation on simulations with different densities and signal to noise ratio led Izeddin and colleagues to conclude that localization density should not exceed 0.5 molecule/ μm^2 (Izeddin et al., 2012; Sibarita, 2014). However, this analysis only took into account the capacity of the computation to achieve good localization accuracy (e.g. number of false positive and false negative detections), but not the ability to reconnect trajectories correctly (e.g. number of false positive and false negative reconnections), suggesting that even lower densities should be recommended.

To achieve good reconnection of single molecule localization, constraints need to be established as there are many possibilities for each trace. The most general approach to obtain the best correct reconnection rate in the shortest computation time, is to restrict the area of possible reconnection within a region potentially explorable by a molecule exhibiting theoretical maximum velocity (Sibarita, 2014). However, different approaches exist, for instance, implementing statistics of behavior to the maximum diffusion coefficient, for the determination of the restriction domain (Sergé et al., 2008). This approach is particularly efficient to avoid false reconnection, especially in high density SPT where different molecules cross paths, allowing to determine through evaluation of probabilities, the best match when it comes to overlapping restriction domains or multiple detections in the same restriction domain. However, the major drawbacks of such frameworks are that they are very time consuming and relies on assumption of probability distribution.

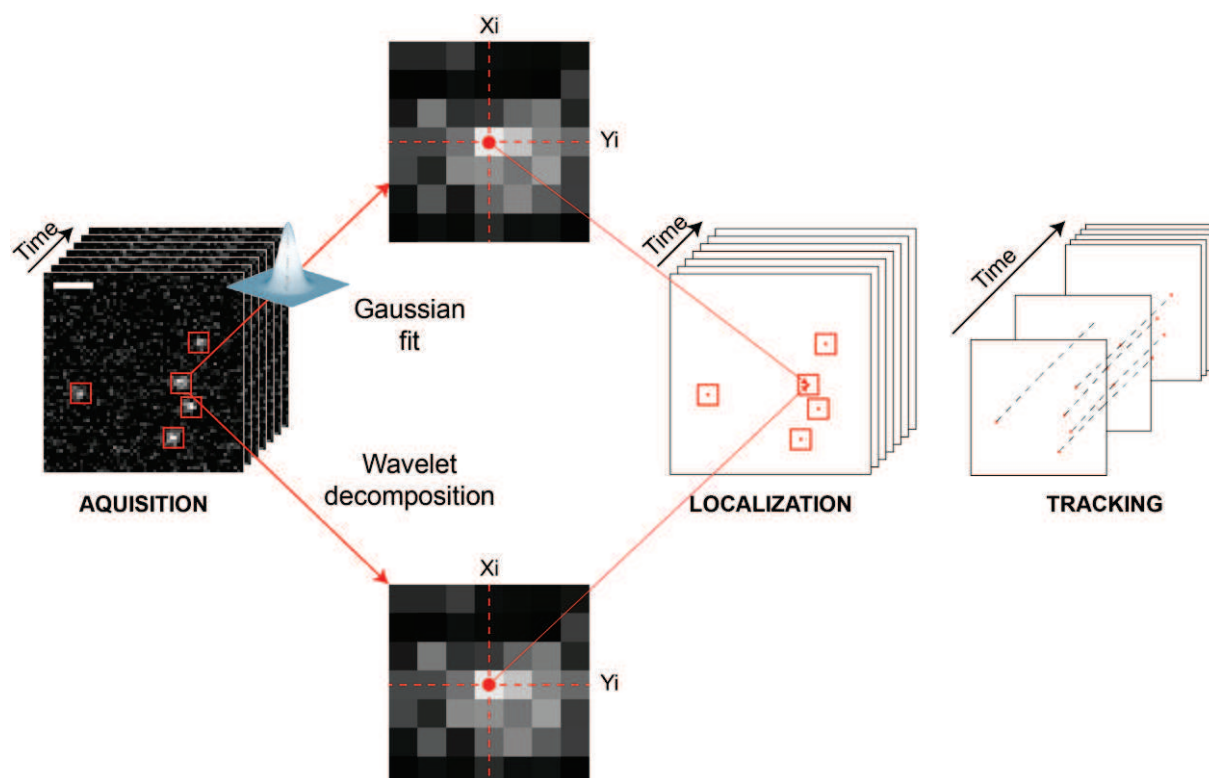


FIGURE 18: FRAMEWORK FOR LOCALIZATION, RECONNECTION, AND CONSTRUCTION OF TRAJECTORIES FROM SINGLE MOLECULE DATA.

SPT experiments are divided into 3 steps: the acquisition (left), localization of fluorescent molecules (middle), and the tracking of each molecule (right) (scale bar: 2 μm)

Segmentation of the detections: each plane of the acquisition dataset is analyzed to extract coordinates of all fluorescent molecules, using different computation methods such as Gaussian analysis (top), and wavelet segmentation (bottom). Then all the detections can be pooled to create a density map, or **reconnected** to form trajectories map.

(Inspired by Sibarita, 2014)

1.3.2.3. *The single particle tracking: analysis*

The most common analysis technique relies on the computing of the mean squared displacement (MSD) as a function of time (Pinaud et al., 2010; Sibarita, 2014) (Figure 19). The $\text{MSD}(t)$ measures the mean area (r^2) explored by a molecule during a period of time. The MSD calculated from the trajectories can be compared to theoretical MSD derived from models for different molecular movement, giving information about the molecule type of motion (diffusive, directed, confined, and others) (Saxton and Jacobson, 1997) (Figure 19). From each $\text{MSD}(t)$ curve calculated, diffusion coefficient (D) can be extracted by fitting the first 4 point of the $\text{MSD}(t)$ with the Brownian model expressed by the equation $r^2(t) = 4Dt$ (Figure 19). However, the diffusion coefficient D is an average motion parameter over the entire trajectory, which does not take into account the time-varying dynamic of the molecule,

for instance its entry inside a confined nanodomain. To assess such information, instantaneous diffusion coefficient can be extracted for each time point: the total trajectory is divided in small segments, for each of them the MSD is calculated, providing with a local diffusion coefficient (Sibarita, 2014). However, the MSD(t) curve and therefore, the calculated D being more accurate for long trajectories, instantaneous D are more sensitive to fluctuations.

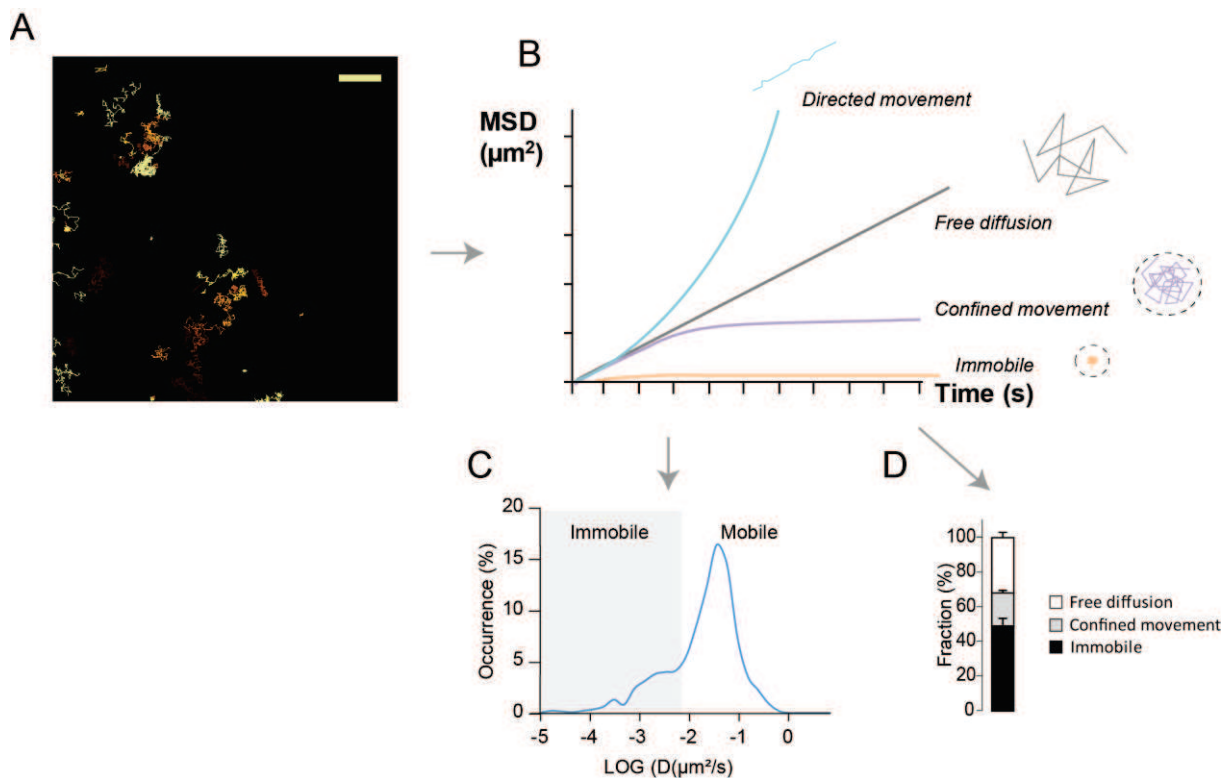


FIGURE 19: MSD BASED ANALYSIS

(A) Typical image reconstruction of single particle tracking trajectories. (Scale bare: $2\mu\text{m}$). **(B)** Classification of single molecule trajectories using the mean squared displacement analysis (MSD): depending on the shape of the MSD function over time, motions can be sorted as directed movement, free diffusion (or Brownian motion), confined motion, and immobile. **(C)** typical distribution of diffusion coefficient that can be extracted from the fitting of the first 4 points of the MSD curve with the Brownian equation model. **(D)** Fractions of the different motions can as well be extracted.

Behind the analysis of changes in molecule diffusion, an important correlated information can be inferred: the environment viscosity. Indeed, changes in molecule behavior can be assessed as global changes in the protein motion proper to the dynamic equilibrium of the biological environment: for instance, the dynamic of AMPA receptors gives information about the molecular mechanisms at stake in acute and chronic synapse plasticity, resulting to the

synapse structure at a t time with specific physiological consequences. Yet, those changes in protein diffusion, are locally dictated by the environment and more precisely, by the protein interactions with binding partners, viscosity of the membrane, the topology of the field, for instance. Although the reconstructed density map generated by high density SPT can give hints about changes in membrane topology/viscosity or localization of molecular interactions, parameters extracted from MSD analyses do not allow the discrimination of local changes in the protein behavior that can be observed in regions with different level of confinement (Renner et al., 2017), as they are averaged over the entire trajectories. Recent analysis developments, however, overcame this issue, and rendered possible to assess new types of parameters, such as landscape parameters or packing coefficient, not available with MSD based analysis (Beheiry et al., 2015; Masson et al., 2014; Renner et al., 2017). The InferenceMap, based on Bayesian inference methods, aims to create an environmental cartography depending on two parameters: the diffusivity, which is linked to the viscosity, and the potential binding energy (reflecting changes in the binding forces due to protein interaction) (Masson et al., 2014). Thanks to this technique, the environment is mapped in meshes, and in each one of them, dynamic landscape parameters are available, such as local changes in diffusion, forces applied on the protein of interest, and energy of the interactions. Finally, the “packing coefficient” defined by Renner and colleagues, proposed an alternative to the MSD based analyses to quantify local confinement sequences, from which the binding rate k_{on} and the backward binding rate k_{off} can be inferred (Renner et al., 2017).

Those techniques are powerful methods that allow a direct observation of the instantaneous behaviors of individual molecules in complex environments, thus accessing a wide range of specific diffusion profiles that are not accessible with ensemble techniques such as FRAP.

1.3.2.4. *Localization precision and limitations*

Good localization precision is fundamental to be able to achieve the resolution of confined nanoscale motion from immobilization. Indeed, the localization precision determines the smallest diffusion coefficient ($D_{threshold}$) measurement achievable by the system, which corresponds to the diffusion of a molecule in an area smaller than the one defined by the localization precision. Effectively, the $D_{threshold}$ is given by:

$$D_{threshold} = \frac{\sigma_{xy}^2}{n \times 4\delta t}$$

where σ_{xy} is the localization precision, n the number of points used to fit the MSD, and δt the acquisition time.

For a D calculated from the first 4 points of the MSD(t) curve, this correspond to:

$$D_{threshold} = \frac{\sigma_{xy}^2}{4 \times 4\delta t}$$

1.4. Probes for single molecule localization microscopy

Thousands of probes have been devised and are now available for fluorescence microscopy (The Molecular Probes® Handbook, 2010).

The recent development of fluorescence-based super-resolution imaging techniques created a critical need for efficient labelling strategies, with the highest signal to noise ratio, the best tissue penetration, and the minimal linkage error, to assess nanoscale organization and dynamics of proteins, as discussed in detail in the following paper (Fernández-Suárez and Ting, 2008). Ideally, probes should allow quantitative labeling with a 1:1 stoichiometry for the target.

Basically, probes used for SMLM fall in two categories: **intrinsic** probes genetically fused to the target, therefore relying on the expression of recombinant protein, and **extrinsic** probes conjugated to organic fluorophores that can either target endogenous or recombinant proteins, summarized in the table [Figure 21](#).

While SPT requires probes that remain fluorescent over several consecutive frames in order to be able to reconstruct trajectories, multiple cycles of detection per probe are to be avoided for quantitative SMLM. Therefore, probe choice must take into account fluorophore photophysical properties as well as probe's internal properties in order to meet the requirement for the microscopy technique used.

1.4.1. Intrinsic probes

Intrinsic probes are **fluorescent proteins**, composed of amino-acids, and therefore, that can be expressed by the cell. Genes of the protein of interest are modified to contain the sequence of the chosen fluorescent protein, and once transfected inside the cell, the protein will be expressed fused to the fluorescent protein.

Some proteins are endogenously fluorescent, this phenomenon is called auto-fluorescence. However, the probability for the protein of interest to be auto-fluorescent remains low, and auto-fluorescence is generally prone to photobleaching. With the discovery and modification of the **Green Fluorescent Protein** (GFP) in the jellyfish *aequorea victoria* (Shimomura et al., 1962; Tsien, 1998), fluorescence microscopy has been revolutionized. Now, a large family of fluorescent proteins are available with a wide cover of the light spectrum. Those proteins share a common structure, composed of around 200-220 amino-acids, forming an 11-stranded β -barrel with an α -helix, containing the chromophore, running up the axis of the cylinder (Tsien, 1998). The chromophore, created by a post-translational modification of the Ser65, Tyr66 and Gly67 residues, is therefore protected from the environment by the β -sheets very stable both thermally and chemically (Figure 20).

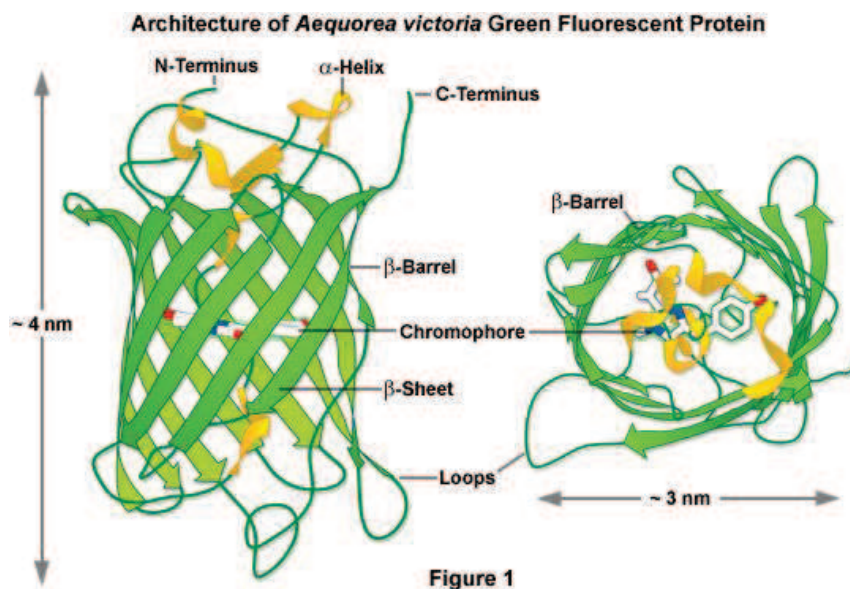


FIGURE 20: TRI-DIMENTIONAL STRUCTURE OF THE GREEN FLUORESCENT PROTEIN.

The barrel formed by 11 β -strands is threaded by an α -helix containing the chromophore.
From <http://zeiss-campus.magnet.fsu.edu/articles/probes/jellyfishfps.html>

Beside changes in the absorption/emission specters, mutations of the GFP were introduced to create PA, PC and PS fluorescent proteins (see Figure 14), at the origin of the development of SMLM (Betzig et al., 2006). PA can transit irreversibly from a non-fluorescent to a fluorescent state, while PS display a reversible transition. PC on the other hand, goes from one fluorescent state to another one, following the absorption of the light of photoconversion (see Figure 14).

Fluorescent proteins are, by nature, not as bright as organic fluorophores, and fewer photons are collected, impacting the signal to noise ratio, and therefore, the localization precision. Moreover, they are less photostable, which render the tracking of protein diffusion more problematic.

Because they are genetically coded, fluorescent proteins are intrinsically specific, and relatively not toxic. Their 1:1 labeling ratio combined with the use of irreversible PA probes are particularly interesting when aiming at absolute quantification of proteins. However, the fusion of a fluorescent protein to the sequence of the protein of interest can be responsible for an alteration of protein folding, trafficking, binding, and thus, overall function.

Moreover, these approaches relying on overexpression of recombinant proteins, can lead to mis-localization of the protein of interest, or even gain-of-function artifacts. Correction of the expression background through KD, KO or ideally KI strategies should ensure a proper level of expression of the protein of interest, and are therefore to be preferred.

1.4.2. Extrinsic probes

Extrinsic probes are generally conjugated to small organic fluorophores whose size does not affect protein accessibility, localization nor diffusion. Although fluorescent proteins may be more suitable for absolute quantification, since organic fluorophores present numerous *on* and *off* states, the use of extrinsic probes present multiple advantages: endogenous proteins can be targeted, organic fluorophores are more photostable, and brighter, which make protein tracking easier and improve the localization precision respectively. Yet they rely on the specificity of the probe, and unspecific binding should be maintained as low as possible, to reduce background noise as well as misinterpretation of the results.

1.4.2.1. *Semi-conductors*

To increase the stability of the fluorescence, an alternative method proposes to coat the probe on semi-conductor nanoparticles called Quantum Dots (QD). QD are very photostable structures, allowing the recording of protein diffusion over longer period of time (tens of minutes to hours) (Pinaud et al., 2010), with minimal photobleaching, and multiple wavelength can be used for dual recordings. Many surface functionalization schemes are available to achieve specific interaction (antibodies, nanobodies, streptavidin...) (Michalet et al., 2005), complemented by surface passivation to minimize unspecific binding (PEG and FAB

coating, for instance) (Bentzen et al., 2005). However, the relatively **large size** (10-40 nm) and **multivalence** of QD are susceptible to alter protein function, diffusion, and localization. Therefore, it is strongly recommended to apply extra precaution when comparing protein behavior, especially when applied to different types of compartments (e.g. extra-synaptic *versus* synaptic).

1.4.2.2. *Antibodies*

While intrinsic fluorophores have the strong advantage to be highly specific, extrinsic fluorophore can target **endogenous protein**, getting rid of over-expression artifacts, or biases induced by the insertion of large protein inside the target.

Conventionally, samples are immunostained and proteins are targeted by specific antibodies. However, this technique relies on the use of highly specific **antibodies**, which are not available for all proteins of interest. The silver lining of such probes is the targeting of endogenous proteins, allowing the description of synapse structures without altering its content. Yet, full-length antibodies are divalent proteins of around 150 kDa, likely to cross-link proteins, thus biasing diffusion measurements and protein quantification. Moreover, biological response as well as protein internalization may be instigated by protein crosslinking (Belleudi et al., 2012; Leemans et al., 2017). Finally, labeling with antibodies may lead to protein mis-localization due to the inaccessibility of such large complexes to the synapse, the synaptic cleft being ~20 nm thick (Chamma et al., 2016b).

1.4.2.3. *Alternative methods relying on recombinant protein expression*

Several alternative methods relying on the detection of tagged-recombinant proteins have been recently developed, aiming to provide high tissue penetration, minimizing protein crosslinking. For instance, anti-GFP **nanobodies** can be used to subsequently label an extra-cellular GFP (Ries et al., 2012), or recombinant protein fused to **enzymatic tags**, such as SNAP, CLIP or HALO tags can be covalently bound to conjugated substrate upon incubation.

However, as for the GFP, the insertion of large tags, such as SNAP or HALO-tag can lead to an alteration of protein functions.

In the effort to provide monovalent small probes, the **monovalent streptavidin** (mSA) targeting a biotin acceptor peptide (AP tag) (15 amino acids) fused to the protein of interest, has been developed. This tool allows to assess protein nanoscale organization and dynamics

with a wide range of microscopy techniques, in both live and fixed conditions (Chamma et al., 2017; Lim et al., 2013; Liu et al., 2013).

However, as for intrinsic probes, these approaches rely on overexpression of recombinant proteins, which may lead to mis-localization and gain-of-function artifacts, therefore KD, KO or KI strategies should be privileged.

1.4.2.4. *DNA-PAINT*

Finally, with the recent development of **DNA-PAINT**, SMLM can be achieved by transiently binding conjugated DNA strands to complementary target-bound strands (Dai et al., 2016; Schnitzbauer et al., 2017; Strauss et al., 2018). The complementary strands can be attached to any kind of probes, for instance to regular antibodies, in order to target **endogenous proteins**. Yet, this approach can introduce linkage error and limit the accessibility of the target by the probe due to steric hindrance. These limitations can be overcome with the use of smaller probes such as nanobodies or **aptamers** (Opazo et al., 2012; Ries et al., 2012; Strauss et al., 2018).

The strong advantage of this technique is the ability of **multiplexing**: indeed, different targets can be probed sequentially by washing the acquisition medium and changing the imager conjugated-DNA strand in solution. Therefore, the technique is limited only by the number of orthogonal DNA sequences and not the number of spectrally distinct dyes. Moreover, for each target the same dye providing the best signal to noise ratio, in the wavelength range with minimal auto-fluorescence (i.e. red shifted) can be used. Finally, as the DNA binding is predictable and tunable, it allows the assessment of quantitative information, technique known as the **quantitative PAINT** (qPAINT). DNA-PAINT applications are currently limited to fixed samples, as the effect of introducing nucleic acid strands in living cells are ill-defined, and may be problematic; however, targeting cell-surface proteins could be theoretically possible.

Probes	Photophysics	quantitative SMLM	Main advantages	Main drawbacks
<i>Intrinsic</i> Fluorescent proteins	(-)	(+++)	Specificity	Over-expression/ large proteic insertion
<i>extrinsic</i> Semi conductors	(+++)	none	Long trajectories	Large size and multivalence
Antibodies	(+)	(- -)	Endogenous	Large size and divalent
Nanobodies	(+)	(-)	Small and monovalent	Not available for all proteins
Enzymatic tags	(+)	(-)	Small and monovalent	Over-expression/ Large proteic insertion
mSA	(+)	(-)	Small and monovalent	Over-expression
DNA-PAINT	(+)	(+++)	Small and monovalent	Endogenous

FIGURE 21: SUMMARY OF THE DIFFERENT PROBES FOR SMLM WITH THEIR PROPERTIES.

1.5. Labeling-induced biases in organization and diffusion studies

Each probe presenting different properties in terms of size and valence, it is fundamental to identify the different biases that can be instigated by the labeling, especially when comparing diffusion or organization of proteins labeled with different probes, or in different compartments.

In 2013, Nair and colleagues found that the diffusion of Eos-conjugated GluA2 AMPA receptor subunits differed from the one measured in uPAINT on endogenous GluA2 (Nair et al., 2013). Indeed, it seems that the diffusion coefficient of GluA2 was shifted towards lower values when labeled with antibodies compared to the recombinant version, suggesting an effect of the labeling on the diffusion. Yet it remains unclear if the observable effect was due to steric hindrance and cross-linking induced by antibody labeling slowing down the target diffusion, or if the altered diffusion was the one measured with the Eos-labeling. Indeed, the protein of interest GluA2 interacts with numerous synaptic partners, that may slow down its diffusion (Bats et al., 2007; Delgado and Selvin, 2018). When over-expressed, the receptor may outnumber its partners, and therefore freely diffuse inside and outside the synapse, resulting in an increase in the measured diffusion coefficient. To be noted that besides the strong immobilization observed with the antibody labeling, more Eos-GluA2 were tracked inside and outside the synapse, with a largely denser population.

Surprisingly, it seems that labeling with big probes led to opposite effects in a more recent study. Indeed, Lee and colleagues found that GluA2 was highly diffusive and extra-synaptic when labeled with big commercial QD, but immobilized and synaptic when labeled with streptavidin conjugated to small QD or organic fluorophores (Lee et al., 2017). The authors hypothesized that not only big QD could not enter the narrow synaptic cleft and label intra-synaptic GluA2, but also extra-synaptic GluA2 labeled with big QD were constrained outside the synapse. As a large number of GluA2 partners are located at the synapse, and therefore would slow down the diffusion of the protein at this location, the immobile population was not assessable with the big probe, biasing the diffusion measurements. Yet, big QD are highly multivalent, coated with numerous streptavidin, and this study does not take into account the impact of this parameter on such measurements.

A more systematic study, comparing the diffusion of the dimeric cell adhesion protein neuroligin1 labeled with a small monovalent mSA, a small tetravalent streptavidin and a big

divalent antibody, highlighted that not only the size of the antibody was affecting the diffusion and localization of the synaptic membrane protein but also the multivalence of the, yet small, streptavidin (Chamma et al., 2016b). Yet, the specific membrane topology of the synapse, with the numerous synaptic partners may be at cause in the effect of the labeling.

For now, it remains unclear what effects are due to the size or the valence of the probe and how the biases identified are actually caused by the environment of the study. There is still a need for a thorough comparison study of probe size and valence specific biases in a more controlled environment.

1.6. Experimental design in the synaptic context

To unravel the key cellular processes at stake in synapse formation and transmission, studying protein interactions and turnover in living cells is a requisite. The dynamic of synaptic proteins gives information about their function, the mechanisms of diffusion/trapping behind their establishment, and their activity in terms of interaction with synaptic partners.

Being a central node for synaptic actors, synaptic cell adhesion molecules (SCAMs) participate highly in the regulation of synapse morphology and function. The existence of a dialogue between SCAMs, scaffold proteins and neurotransmitter receptors highlights the importance of those three actors and reinforce the need for a better understanding of the phenomenon hidden behind their establishment. In order to build an appropriate model of the synapse structure and formation, it is fundamental to develop technics assessing the absolute numbers of the proteins involved. To understand the effect of probe binding on protein diffusion and organization, I chose 3 stereotypical proteins of the excitatory synapse: the trans-synaptic complex **Neurxin/Neurologin**, as they are among the most studied SCAMs, and a glutamatergic receptor: the kainate receptor **GluK2**.

The PSD of excitatory synapses forms a large protein network, which components have been identified and characterized over the past twenty years, using various techniques, from immuno-cytochemistry to mass spectrometry on synaptosome extracts (Boeckers, 2006). Overall, the proteins in the PSD can be classified in 6 categories: cytoskeleton proteins, G-protein and their adaptors, signalization proteins (including kinases and phosphatases), adherence proteins, scaffolding proteins, and finally, receptors and channels.

1.6.1. Glutamatergic receptors

Two types of neurotransmitter receptors exist: the ionotropic receptors, which form ionic channels, and the metabotropic receptors coupled to G-proteins.

Ionotropic receptors can be activated by different agonists, which allows them to be classified in 3 groups: the AMPA receptors, the NMDA receptors and the kainate receptors.

AMPA receptors are heteropentameric structures, from the combination of 4 subunits (GluA1-4), responsible for the vast majority of rapid excitatory response, whereas NMDA receptors have slower kinetics and play a key role in the induction of long term potentialisation and depression involved in learning and memory (Malinow and Malenka, 2002).

Finally, **kainate receptors** are implicated in excitatory and inhibitory synapse modulation brain wide and have been identified in multiple neurological diseases, from mood disorders to epilepsy (Contractor et al., 2011; Lerma and Marques, 2013). These tetrameric glutamate receptors are composed of a combination of five sub-units (GluK1-5), and regulates the activity of synaptic circuits at the pre- and post-synaptic level, through their ionotropic or metabotropic actions. While AMPA and NMDA receptors are predominantly found in excitatory post-synaptic signaling complexes, kainate receptors are largely present at the pre-synapse, where they act principally as modulators of synaptic transmission and neuronal excitability. For instance, kainate receptors can induce excitatory synaptic plasticity by increasing synaptic release probability. Interestingly, both short term and long term potentiation of mossy fiber synaptic transmission are impaired in the GluK2 KO and GluK3 KO mice. (For review: Contractor et al., 2011).

1.6.2. Synaptic cell adhesion molecules

A single neuron receives multiple types of afferences, and mis-alignment of the pre- and post-synaptic partners would lead to a non-functional synapse. The expression of synaptic cell adhesion molecules in pre- and post-synapses allows the stabilization of the interaction between the two corresponding partners, as well as the initiation of the synaptic differentiation and maturation phenomenon.

Many trans-synaptic interactions have been identified in the shaping of synapse formation, ranging from a role in initial contacts formation to the differentiation of the pre- and post-

synaptic compartments. As the SCAMs interact with a large number of intra- and extra-cellular partners, they are involved in both the morphology and function of the synapses.

Among the SCAMS, the trans-synaptic complex **Neurexin/Neuroigin** has been widely studied. This complex seems to be a key node in synapse formation and differentiation, and genetic mutations in these molecules have been associated with autism and schizophrenia, suggesting that it is centrally involved in neuropsychiatric diseases.

Briefly, **neurexins** (*nrxn*) are type I membrane proteins, expressed from three genes (*nrxn1-3*) in mammals, under the control of three different promoters, producing three classes of *nrxn*: α -neurexin, β -neurexin, and γ -neurexin. With its 3 genes, 3 promoters, and 6 alternative splice sites (from SS1 to SS6), thousands of *nrxn* isoforms can be differentially expressed (Schreiner et al., 2014; Treutlein et al., 2014). *Nrxn* are now known to interact with at least 7 post-synaptic families, and soluble adaptor proteins. Three ligand binding sites have been identified on *nrxn*. Although ligands cannot bind at the same time on the same site, different sites can be bound simultaneously, and each ligand is linked to its own partners, therefore anchoring a massive network both at the pre- and post-synaptic surface. Because they are colossal ligand platforms, *nrxn* are involved in a wide range of regulatory functions (For review: Südhof, 2017).

Neuroigin (*nlgns*), on the other hand, are type I proteins, composed of a single large extra-cellular domain, which constitutively dimerize and is composed of an inactive esterase homology domain, a transmembrane domain (TMD), followed by a small cytoplasmic tail (Chen et al., 2008).

Nlgns were discovered as *nrxn* endogenous ligands, as they co-immunoprecipitate from brain extract (Ichtchenko et al., 1995). The *nrxn/nlgn* complex is formed by the calcium-dependent interaction of one dimer of *nlgn* with two molecules of *nrxn*, from their extra-cellular domains (Araç et al., 2007). Like the *nrxns*, the *nlgns* can be alternatively spliced on two sites: the site A and the site B (SSA and SSB). While *nlgn4* has a ubiquitous expression in humans, the *nlgns* 1, 2 and 3 are exclusively expressed in the central nervous system, and their expression profile is correlated with synapse development (Irie, 1997; Song et al., 1999). In accordance with their presumed role in synapse differentiation, the different isoforms of *nlgn* are segregated differently at the post-synapse: *nlgn1* is mainly found at the excitatory post-synapse (Song et al., 1999), whereas *nlgn2* is present at inhibitory synapses, dopaminergic and cholinergic

synapses (which use GABA as a co-transmitter) (Graf et al., 2004). Nlgn3, on the other hand, is found at both excitatory and inhibitory synapses (Budreck and Scheiffele, 2007), and nlgn4 at glycinergic contacts. Despite their differential localization, all nlgns can interact equally well with PSD-95 and gephyrin *in vitro*, since the motifs are extremely conserved (Irie et al., 1997; Pouloupoulos et al., 2009). Suggesting, there are additional mechanisms that exist *in vivo*, which explain their different localization profiles (Giannone et al., 2013b; Letellier et al., 2018). At excitatory post-synapses, PSD-95 and S-SCAM, another post-synaptic partner of nlgn1, interact directly with NMDA receptors, while PSD-95 can also interact with AMPA receptors indirectly, through the AMPA receptor auxiliary subunits (TARPs) (Bats, Groc, & Choquet, 2007; Shi et al., 2009). At inhibitory synapses, gephyrin is involved in the clustering of the GABA receptors (Kneussel and Betz, 2000). On top of playing a role in synaptic differentiation *via* the recruitment of scaffolding proteins and therefore of synaptic receptors, the interaction of the nlgn with its post-synaptic partner can play a role in synapse function. For instance, it has been suggested that the binding of nlgn1 with the PSD-95 could affect the release probability of glutamate, thus regulating the pre-synapse through trans-synaptic signaling (Futai et al., 2007).

Overall, the synaptic regulatory functions of nlgn are isoform specific, with no general rule as differential effect throughout the different brain structures are observed, highlighting the multiple enigmatic mechanisms in action (for review: Südhof, 2017).

Objectives

With the major breakthrough of super-resolution microscopy, it is now possible to study at nanoscale resolution, the synapse structure and specificity, and its component dynamics. In a general effort to refine tool efficiency, and limit the biases, probes are continuously being developed, each one of them with their advantages and drawbacks. This gives rise to a crucial need to understand the different biases induced by the experimentation on the observed mechanisms. Recent studies highlighted the crucial importance of choosing the right probe to characterize synaptic protein diffusion and organization, yet it is unclear what effect belongs to the size or to the valence of the probe. Indeed, most of the studies are performed to assess the dynamics of neuronal membrane protein, and the synapse topology being as it is with its very narrow synaptic cleft, probes of large size might have exacerbated effects due to steric hindrance. Moreover, synapses are very dense compartments, highly crowded with proteins, and probe-induced crosslinking of the protein of interest might have worsened effects on protein diffusion and organization in presence of binding partners.

In my thesis, I focused on the effect of **probe size** and **valence**, on the diffusion and organization of receptors having different transmembrane configurations, in a **controlled environment**. To that end, I first compared the diffusion of AP-tagged proteins in heterologous cells using uPAINT and FRAP, getting rid of the synapse membrane topology and partner interaction effects, labeled with probes of 2 different sizes and 3 different valences. In a second part, I characterized the effect of probe size and valence on protein aggregation levels using dSTORM in the same experimental conditions.

Finally, I used the technique developed in the second part, to assess the protein levels of the three synaptic proteins: the synaptic adhesion proteins β -neurexin1 and neuroligin1, and the GluK2 receptor, in dissociated neuronal cultures.

– CHAPTER 2 –
Materials and Methods

2.1. Slide and coverslip preparation

2.1.1. Culture support preparation

In order to be able to illuminate the sample in TIRF configuration, a refractive index of the culture substrate superior to the observation medium is required (1.33-1.38). Cells are plated on 18 mm glass borosilicate Marienfield 1.5H coverslips (thickness: 0.170 mm \pm 0.005 mm, refractive index: 1.52). Coverslips are cleaned before use, to insure the absence of non-specific fluorescent particles. Coverslips are placed in nitric acid (65% m/m) for at least 12 hrs, followed by 6 baths of ultrapure water of at least 30 min. After a quick absolute ethanol rinse, coverslips are sterilized placing them in an oven at 240°C for 8 hrs. These steps are performed weekly by qualified technicians in the laboratory (R. Sterling).

2.1.2. Slide and coverslip preparation for single molecule pull down

Slides and coverslips were prepared as described in Reza Vafabakhsh PhD thesis (Reza Vafabakhsh, 2013).

Surface passivation is essential to achieve specific trapping of single molecule on surface tethered samples. The most efficient and robust passivation to date relies on the high-density covalent binding of polymer chain, such as Polyethyleneglycol (PEG) to the glass surface.

The protocol for preparing PEGylated surface has three steps (Jain et al., 2012):

- 1- Cleaning of the slides and coverslips,
- 2- Aminosilanization of the surfaces,
- 3- Pegylating surfaces.

2.1.2.1. Slide and coverslip cleaning

In order to achieve homogenous and efficient passivation, surfaces must be exempt of impurities and dirt. Borosilicate coverslips and standard microscope slides manufactured by Knittel were used, and holes are drilled in the slides to prepare the future channel entries and exits.

First, slides and coverslips are rinsed with MilliQ water and microwaved for 10 min, then, placed in separate glass jar for sonication. Both coverslips and slides are rinsed with MilliQ water and sonicated for 30 min in acetone, followed by 30 min in methanol. After 4 rinses

with MilliQ water, slides and coverslips are sonicated for 20 min in 5 M KOH, then rinsed again 4 times with MilliQ water and sonicated twice in methanol for 2 min.

In the meantime, a glass flask is cleaned for preparing the silane solution. The flask is sonicated with 1 M KOH for 30min, followed by 30 min in methanol.

2.1.2.2. *Aminosilanization*

Aminosilanization of the clean glass surface of slides and coverslips allows the covalent binding of the m-PEG.

The aminosilane solution is prepared in the clean glass flask by mixing 150 mL methanol, 7.5 mL acetic acid and 2 mL aminosilane, then, poured in the slide and coverslip jars, and sonicated for 20 min.

2.1.2.3. *PEGylation*

Slides and coverslips treated with aminosilane are rinsed 4 times with methanol, with water, and dried with gentle nitrogen blow.

For 6 coverslip/slide pairs, 157 mg of mPEG-SVA and 1-2 mg of mPEG-biotin are mixed in 540 μ L of 0.1 M sodium hydrogen carbonate, and centrifuged at 10,000 rpm for 1 min. 98 μ L of this PEGylation solution is applied on each slide, and the coverslip is placed on top. Coverslip/slide pairs are kept assembled overnight in a dark, flat humid environment, then disassembled, rinsed thoroughly with MilliQ water, and dried with gentle nitrogen blow.

Each slide and coverslip pair is stored in a clean 50 mL tube, at -20°C, with the PEGylated surfaces facing away from each other.

2.2. Cell culture and transfection

2.2.1. COS-7 cells

The synapse is a very crowded environment, with specific membrane topology, where numerous synaptic partners can be found for nrxn, nlgn, GluK2. To avoid an exacerbation of probe size and valence effects due to membrane topology and binding to synaptic partners, proteins of interest were expressed in African green monkey kidney (COS-7), as this cell model do not express endogenously the protein of interest and presents a homogenous membrane surface.

After an electroporation with 4-6 μg of DNA, using Amaxa nucleoporation kit (Lonza), following the constructor's instructions, cells were plated on 18 mm coverslips and maintained in Dulbecco's modified eagle's medium supplemented with 10% fetal calf serum, glutamine (2mM), antibiotics (Invitrogen), and biotin (10 nM) at 36°C and 5% CO₂ atmosphere. For the dSTORM experiments, coverslips were coated for 3 hrs with 0.1 mg/ml of poly-lysine. Experiments are carried out 24-48 hrs after electroporation.

2.2.2. HEK 293 cells

Human embryonic kidney 293 (HEK 293) cells were grown on 12-well plastic plates 24 hrs before transfection and maintained in Dulbecco's modified eagle's medium supplemented with 10% fetal calf serum, glutamine (2mM) and antibiotics (Invitrogen) at 36°C and 5% CO₂ atmosphere. Lipofectamine (Invitrogen) was used for the transfection. The experiments were performed 36 to 48 hrs after transfection.

2.2.3. Primary neuronal cultures

Primary Banker's cultures of hippocampal neurons are prepared from embryonic rats at day 18, in accordance with the French Ministry of Agriculture and the Direction Départementale des services vétérinaires de Bordeaux, based on the following protocol (Kaech and Banker, 2006). Neuron dissection and culture are performed weekly by several dedicated technicians and engineers in the laboratory (B. Tessier, S. Benquet, E. Verdier...).

2.2.3.1. *Coating, and dissection of the glia for Banker's cultures*

At least 24 hrs before dissection, 60 mm diameter dishes are coated with 1 mL/dish of PLL at 0.1 mg/mL. After 15 min of incubation at 36°C and 5% CO₂ atmosphere, the coated dishes are washed twice with 5 ml of ultrapure water and 5 mL of MEM-Horse Serum is added. Dishes are placed at 36°C and 5% CO₂ atmosphere until cell plating.

Dissection is carried out in HBSS containing Penicillin-Streptomycin and HEPES. Hippocampus is placed in a 15 ml falcon and incubated in 5 mL of trypsin-EDTA/Penicillin-Streptomycin/HEPES, for 15 min at 36°C and 5% CO₂ atmosphere, before being washed twice in warm HBSS. Cells are dissociated with a Pasteur pipet pre-coated with Horse Serum. 10 μL of cell suspension is diluted in 90 μL of trypan blue 50%. Cells are counted in a Malassez chamber and \sim 20K – 40K cells are plated on the coated 60 mm diameter dish.

The medium of the glia is changed at day in vitro 10 (DIV10): dish is washed with 2 mL of complete Neurobasal medium, then 5 mL of complete Neurobasal medium is added.

Glia are in culture for 15 days before being used for Banker's cultures.

2.2.3.2. *Coating, and dissection of the neurons for Banker's cultures*

Four 18 mm diameter cleaned coverslips are placed in a 60 mm diameter dish.

At least 24 hrs before dissection, 18 mm diameter coverslips are coated with 200 μ L/coverslip of PLL at 1 mg/mL. After 2 hrs of incubation at 36°C and 5% CO₂ atmosphere, the coated coverslips are washed twice with 5 ml/dish of ultrapure water and 5 mL/dish of MEM-Horse Serum is added. Dishes are placed at 36°C and 5% CO₂ atmosphere until cell plating.

Dissection is carried in HBSS containing Penicillin-Streptomycin and HEPES. Hippocampi from several embryos are placed in a 15 ml falcon and incubated in 5 mL of trypsin-EDTA/ Penicillin-Streptomycin/HEPES, for 15 min at 36°C and 5% CO₂ atmosphere, before being washed twice in warm HBSS. Cells are dissociated with a Pasteur pipet pre-coated with Horse Serum. 10 μ L of cell suspension is diluted in 90 μ L of trypan blue 50%. Cells are counted in a Malassez chamber and ~ 500 K per condition are used for electroporation. Dissected neurons are electroporated with 1-2 μ g of DNA using Amaxa kit (Lonza), before being plated on 18mm coated coverslips.

Half of the neuron medium was mixed with fresh medium every 7 days.

For dSTORM experiments, cells were labelled and fixed, at 14 DIV, and imaging sessions were performed within 3 weeks after fixation.

2.3. Expression constructs

The AP- β -nrxn1, AP-nlgn1, pDisplay-HA-6His-AP-CFP (TMD) and BirA^{ER} constructs were kindly provided by A. Ting (MIT, Boston) (Howarth and Ting, 2008; Liu et al., 2013). Human GFP- β -nrxn1 was a gift from M. Missler, (Münster University, Germany), and Flag-LiGluR439C and LiGluR439C-GFP were kindly given by E. Isacoff (Berkeley University, USA). AP-LiGluR439C was generated using the extraction kit GeneJet (ThermoFisher), fusing the AP Tag (amino-acid sequence GLNDIFEAQKIEWHE) to the NotI/notI restriction sites of the Flag-LiGluR439C. The AP tag sequence was amplified by PCR from pDisplay-HA-6His-AP-CFP. Oligonucleotides used for the PCR amplification, were as follows: AP-11F, 5'-

ATAAGAATgcgccgcGATCTTCAGGAGGCCTGAACG-ATATCTTCG-3; AP-12R, 5'-
ATAAGAATgcgccgcAATCCAGACGACTCGTGCCACTCGATCTT-3'.

Nlgn1 with GFP insertion at position -21 amino acids (nlgn1-GFP) was created in the laboratory and described previously (Giannone et al., 2013). Homer1cGFP was a kind gift from S. Okabe (Tokyo; Okabe et al., 2001).

Vglut1mCherry was generously provided by Etienne Herzog (IINS, France).

2.4. Labeling strategies and fixation

2.4.1. Fluorescent probes

Monovalent streptavidin (mSA), divalent streptavidin (dSA), and anti-biotin conjugated to atto594 or alexa647, as well as the atto594 conjugated streptavidin were generously provided by M. Sainlos (IINS, University of Bordeaux, France). Streptavidin conjugated to alexa647 was purchased to Invitrogen (S32357).

Briefly, all proteins (mSA, dSA, streptavidin (85878, Sigma-Aldrich), mouse monoclonal anti-biotin (03-3700, Invitrogen) were prepared in PBS at 1 mg/mL. Probes were coupled to Atto 594 and Alexa 647 with the corresponding NHS ester derivatives of each dye as described in the recommended procedures from the manufacturers (ATTO-TEC and Life Technologies, respectively), in the dark at room temperature for 1 hr. Sephadex G-25 medium (PD MiniTrap G-25, GE Healthcare) was used to remove excess dye with PBS elution. Further purification of the probes was achieved by size exclusion chromatography with a Superdex 75 HiLoad 16/60 column (GE Healthcare) on an AKTA purifier system (GE Healthcare) using PBS as a running buffer. Amicon Ultra centrifugal filters with a 10-kDa cutoff was used to obtain final labeled-protein concentration of 0.2 mg/mL. All proteins were stored -80 °C until use, after being aliquoted and flash-frozen (Chamma et al., 2016b, 2017).

2.4.2. Labeling

AP-tagged constructs are co-electroporated with the biotin ligase enzyme BirA^{ER} (Howarth and Ting, 2008). While protein traffic through the endoplasmic reticulum, BirA^{ER} covalently links a biotin group to a lysine residue present in the AP tag. The protein is then addressed to the

membrane with the biotinylated AP tag facing the extracellular space. Labeling can be achieved by incubating the conjugated probes targeting the biotin in the extracellular medium (Figure 22).

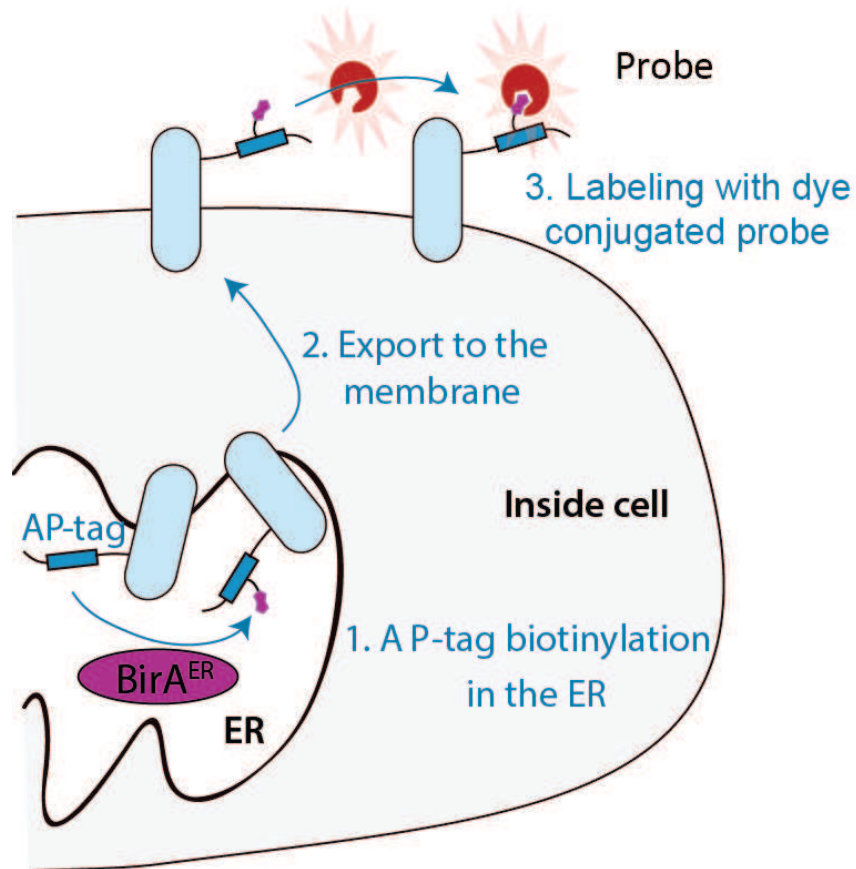


FIGURE 22. SCHEME ILLUSTRATING THE LABELING OF AP-TAGGED MEMBRANE PROTEIN.

1. The resident biotin ligase enzyme BirA^{ER} covalently binds biotin (in purple) to the lysine residue in the AP tag of the protein trafficking through the endoplasmic reticulum. **2.** The protein is addressed to the plasma membrane, **3.** where it can be labeled by conjugated probes targeting the biotinylated AP-tag.

Modified from (Chamma et al., 2017)

2.4.2.1. *uPAINT labeling*

To isolate single molecules, probes conjugated to atto594 are diluted at the same labeling concentration, ranging from 0.1 to 0.3 nM depending on the level of expression of the protein of interest, in 500 μ L of Tyrode (15 mM D-Glucose, 108 mM NaCl, 5 mM KCl, 2 mM MgCl₂, 2 mM CaCl₂, 25 mM HEPES, pH 7.4) globulin-free BSA 1% (Sigma), centrifuged at 13,600 rpm for

5 min to get rid of aggregates, and added directly into an open Inox observation chamber (Life Imaging Services, Basel, Switzerland) (Ludin) containing the coverslip with the cells.

58 nM of non-conjugated neutravidin (Invitrogen, A2666) was added to the 0.3 nM of streptavidin atto594, mimicking the dSTORM labelling concentration, to check the effect of the concentration on the crosslinking,

2.4.2.2. FRAP and dSTORM labelling

To provide the best signal to noise ratio, limiting at maximum the risks of non-specific labelling, cells are incubated for 10 min in tyrode globulin-free BSA 3%. Probes conjugated to atto594 (for FRAP experiments) or alexa647 (for dSTORM experiments) are diluted at 58 nM in tyrode BSA globulin-free 3%, and centrifuged for 10 min at 13,600 rpm, to get rid of the aggregates. Coverslips containing the cells are incubated with the 100 μ l of the labelling solution on parafilm, for 10 min, at 37°C, 5 % CO₂ atmosphere. Then, cells are rinsed 3 times in tyrode globulin-free BSA 3%, which removes the probes in solution.

2.4.3. Fixation for dSTORM

After the labelling of the proteins, cells are rinsed one more time in tyrode, and fixed with PFA 4% glutaraldehyde 0.2%, for 15 min, at room temperature. Cells are rinsed 3 times with PBS, and 50 mM of glycine is used to neutralize the aldehyde functions, thus, preventing the auto-fluorescence of the fixative agents. Cells are rinsed 3 more times with PBS, and stored in PBS at 4°C (Bates et al., 2013).

2.5. Microscopy

2.5.1. Setup configuration

Samples are visualized on an inverted microscope (Nikon Ti-E Eclipse) equipped with an EMCCD camera (Evolve, Roper Scientific, Evry, France), an apochromatic (APO) total internal reflection fluorescence (TIRF) $\times 100 / 1.49$ numerical aperture (NA) oil objective, and a perfect focus system allowing long acquisition both in TIRF and oblique illumination mode. A thermostatic box (Life Imaging Services) provides air at 37 °C for live imaging. GFP-tagged proteins are detected using a mercury lamp (Nikon Xcite) and the following filter sets (SemROCK, USA): EGFP (excitation: FF01-472/30; dichroic: FF-495Di02; emission: FF01-525/30). A four-colour laser bench (405, 488, 561, 100 mW each, and 642 nm, 1W; Roper Scientific) is connected through an optical fiber to the TIRF illumination arm of the microscope.

The Metamorph software (Molecular Devices, USA) allows the control of laser powers through acousto-optical tunable filters. GFP, Atto594, and alexa647 are excited with the 488-, 561- and 642-nm laser lines through a four-band beam splitter (Di02-R405/488/561/635, SemRock). Samples are imaged by oblique or TIRF illumination. Fluorescence is collected using FF01-593/40, FF01-617/73 emission filters (SemRock), placed on a filter wheel (Suter) for photobleaching step counting, uPAINT and FRAP.

2.5.2. Single photobleaching step counting

Using TIRF, sparse receptors immobilized on a substrate can be imaged, and their fluorescence collected until totally bleached. The fluorescence intensity of a protein complex being directly proportional to the number of fluorescent molecules attached (here, GFP), the discrete steps of photobleaching that can be observed correspond to the number of fluorescent proteins in the receptor complex (Jain et al., 2012).

The photobleaching step distributions are compared to the theoretical binomial distributions for complexes formed of 1, 2 or 4 subunits with an 80% probability of detection of the GFP.

2.5.2.1. Cell lysate preparation

HEK cells transfected with Lipofectamine 36 to 48 hrs before experiment, expressing the GFP-tagged constructs, are rinsed with PBS, knocked off the coverslips with incubation in PBS for 20 min at 36°C, 5% CO₂ atmosphere, and centrifuged for 5 min at 5,000 rpm. The supernatant is removed, and the cell pellet is dissolved by adding 100 µl of lysis buffer (150 mM NaCl, 10 mM Tris-HCl, 1mM EDTA, protease inhibitor cocktail, and 1-2% Igepal detergent), and aliquots are tumbled gently at 4°C to solubilize proteins, for 30 min to 2 hrs.

Solubilized proteins are centrifuged at 10,000 g for 20 min, and the supernatant containing the proteins is kept.

To obtain single molecules well separated on the substrate, while optimizing the fluorescence signal, the cell lysate is diluted in observation buffer: Trolox solution (135 mM NaCl, 5.4 mM KCl, 2 mM CaCl₂, 1 mM MgCl₂, 10 mM HEPES, 4 mM Trolox, 444 mM D-glucose; pH 7.4, kept in the dark) containing 0.03% Igepal detergent.

2.5.2.2. Observation chamber preparation

The pair of PEGylated slide and coverslip is assembled, and channels are delineated using double-sided scotch tape, while epoxy glue is used to clog the holes on the side.

All antibodies and neutravidin are diluted in T50 (10 mM Tris-HCl, pH 7.5-8.0, 50 mM NaCl). Channels are rinsed in T50. First, a layer of neutravidin (Invitrogen, A2666) targeting the biotinylated-PEG is made by flooding the channel with 50 μ L of 1 μ M neutravidin, for 5 min. After rinsing with T50, 15-20 nM of biotinylated anti-GFP (ABCAM, ab6658) is incubated into the channels for 20 min. Channels are rinsed again with T50.

Different controls of specificity were made, removing the neutravidin, the antibody, or incubating with a non-relevant antibody.

2.5.2.3. *Acquisition and analysis*

Sample is imaged by TIRF illumination, allowing the excitation of individual fluorophores bound to the glass surface, without illuminating ligands in solution.

Stacks of 600-1,500 consecutive frames are obtained for each acquisition, with an integration time of 20-50 ms, until complete photobleaching of the sample.

Photobleaching steps are manually counted in the Metamorph software (Molecular Devices, USA), and a distribution of photobleaching steps is made for each protein.

2.5.3. Single molecule tracking: uPAINT

2.5.3.1. *Acquisition*

uPAINT experiments were carried out as previously reported (Giannone et al., 2010). COS-7 are electroporated 24-48 hrs prior to the experiment. Cells expressing the different AP-constructs are mounted in the Tyrode-labelling solution in a Ludin chamber placed on the inverted microscope.

Samples are imaged by oblique laser illumination, allowing the excitation of individual Atto-conjugated ligands bound to the cell surface, without illuminating ligands in solution. Protein diffusion is recorded on the edge of the COS-7 cells, allowing to assess the background noise of each probe, and improving the signal to noise ratio by limiting signal coming from cellular structure auto-fluorescence. Stacks of 4,000 consecutive frames are obtained from each cell, with an integration time of 20 ms. Laser power is adjusted to obtain good signal to noise ratio, while avoiding photobleaching as much as possible.

2.5.3.2. *Trajectory analysis and image reconstruction*

Trajectories were reconstructed from the image stacks using a custom program running on Metamorph described earlier and generously provided by JB Sibarita and his group (Izeddin et

al., 2012; Kechkar et al. , 2013). This program relies on wavelet segmentation for the localization of single molecules and simulated annealing algorithms to reconnect trajectories. The diffusion coefficient, D , is extracted for each trajectory by fitting the first 4 point of the MSD function of time, with the linear equation $r^2(t) = 4Dt$, where r^2 is the mean area explored during the time t (Sibarita, 2014).

2.5.3.3. Localization precision and $D_{threshold}$

Localization precision was calculated as followed:

$$\sigma_{xy} = \sqrt{\sigma_x^2 + \sigma_y^2} \sim 0.05 \mu\text{m}$$

Molecules were sorted as mobile or immobile defined by: $D_{immobile} < D_{threshold} < D_{mobile}$, as molecules with $D < D_{threshold}$ would explore an area smaller than the one defined by the localization precision (0.05 μm):

$$D_{threshold} = \frac{\sigma_{xy}^2}{n \times 4\Delta t} = \frac{(0.05\mu\text{m})^2}{4 \times 4 \times 0.02\text{s}} \sim 0.008 \mu\text{m}^2 \text{ s}^{-1}$$

where σ_{xy} is the localization precision, n the number of points measured and Δt the elapsed time.

2.5.4. Fluorescent Recovery After Photobleaching: FRAP

COS-7 cells expressing the different AP-tagged constructs are labelled 24-48 hrs after electroporation as described in the labeling section. Cells are mounted in Tyrode globulin-free BSA 1% in a Ludin chamber placed on the inverted microscope. An illumination device containing galvanometric scanning mirrors (ILAS, Roper Instrument) steered by MetaMorph is connected to a second optical fiber output on the laser bench. A mirror is used to switch in the millisecond range between the two fibers, allowing to alternate imaging and bleaching. 561 nm laser oblique illumination at low power is used to image molecules accumulated at the cell surface. FRAP is recorded on the edge of the COS-7 cells, allowing us to assess the background noise of each probe and observational photobleaching, providing an improved signal to noise ratio by limiting auto-fluorescence signal coming from cellular structures. After acquiring a 3-s baseline at 1 Hz frame rate, rapid selective photobleaching of three regions of diameter 13 pixels (pixel size=160 nm; real bleached region diameter after measurement: 3.52 μm) is achieved at higher laser power during 192 ms. Fluorescence recovery was then

recorded immediately after the bleach sequence for 5 s at 1 Hz frame rate, followed by 30 s at 0.5 Hz and 145 s at 0.2 Hz. Photobleaching induced by the image sampling was kept very low, as assessed by observing non-photobleached areas.

As described in Matthieu Lagardère PhD thesis (Lagardère, 2018), the mean fluorescence signal is measured in each photobleached areas, in the cell excluding the photobleached areas giving the total fluorescent signal of the cell f_{total} , as well as outside the cell to obtain the background fluorescent level $f_{background}$. Once the background fluorescent level is subtracted, the fluorescence recovery $f(t)$ is then corrected from observational photobleaching using the following formula:

$$F(t) = \frac{(f(t) - f_{background}(t))}{f_{total}(t) - f_{background}(t)} \bigg/ \frac{f_{total}(0) - f_{background}(0)}$$

Then, the corrected signals are normalized between 0 (signal after photobleaching: F^+) and 1 (mean signal before photobleaching: F^-), using the following formula:

$$\tilde{F}(t) = \frac{F(t) - F^+}{F^- - F^+}$$

Data can be averaged to obtain the photobleaching recovery by acquisition, cell or condition.

Data were plotted as normalized fluorescence intensity versus time and fitted by the diffusion formula:

$$\tilde{F}(t) = e^{-\frac{2\tau_D}{t}} \left(J_0 \left(\frac{2\tau_D}{t} \right) + J_1 \left(\frac{\tau_D}{t} \right) \right)$$

Where J_0 and J_1 are the modified Bessel functions of order 0 and 1. τ_D is the characteristic diffusion time of the species, for a circular profile: $\tau_D = R^2/4D$, with R being the the radius of the photobleached circle. The details of the calculation leading to this equation are given in reference (Soumpasis, 1983).

2.5.5. dSTORM

COS-7 cells and primary culture neurons expressing the AP-tagged constructs (AP-neurexin1 β , AP-neuroigin1, or AP-GluK2) are surface-labeled as described in the labeling section.

Multicolor fluorescent 100 nm beads (Tetraspeck, Life Technologies) are used to register long-term acquisitions and correct for lateral drifts (**Figure 23**). Image acquisition is performed on the edge of the COS-7 cells, allowing us to assess the background noise of each probe, and improving the signal to noise ratio by limiting auto-fluorescence signal from the cell. To facilitate the stochastic emission of the alexa647, the cells are placed in a hermetic chamber to isolate them from oxygen, and the following imaging-buffer was used: for COS-7 cells experiments 925 μL of glucose based solution (D-glucose 0.56 M and glycerol 1.36M) + 125 μL of enzyme solution (catalase 4 $\mu\text{L}/\text{mL}$, TCEP 8 mM, glycerol 13.6 M, KCl 0.05 mM, Tris HCl pH 7.5 0.04 mM, glucose oxidase 2 mg/mL; pH adjusted to 7.4) + 200 μL of MEA solution (1 M; pH adjusted to 7.4); for neuron experiments 1 mL of glucose based solution + 125 μL of enzyme solution +125 μL of MEA solution (Bates et al., 2013).

The WaveTracer module generously provided by the group of JB Sibarita (Kechkar et al., 2013), allows online single molecule localization and image, enabling optimal adjustment of laser intensities to obtain the best single-molecule density during the acquisition. High laser power of 647 nm (around 6 mW at the front of the objective) is used to switch fluorophores to the triplet state, while the acquisition laser power is set to around 3 mW at the front of the objective. The power of 405 nm is gradually increased along the experiment, to promote the probe return to the singlet state, then kept at maximal power until extinction of fluorescence, to ensure complete cycles for all the fluorophores (Bates et al., 2013). The acquisition and localization sequences are driven by MetaMorph (Molecular Devices) at 50 frames per second (20-ms exposure time) using a region of interest equal to 256×256 pixels (center quadrant). Super-resolution reconstructions are generated with the PalmTracer software (Izeddin et al., 2012; Kechkar et al. , 2013), based on wavelet segmentation for detection, combined with a 2D isotropic Gaussian fit on each detected localization (**Figure 23**).

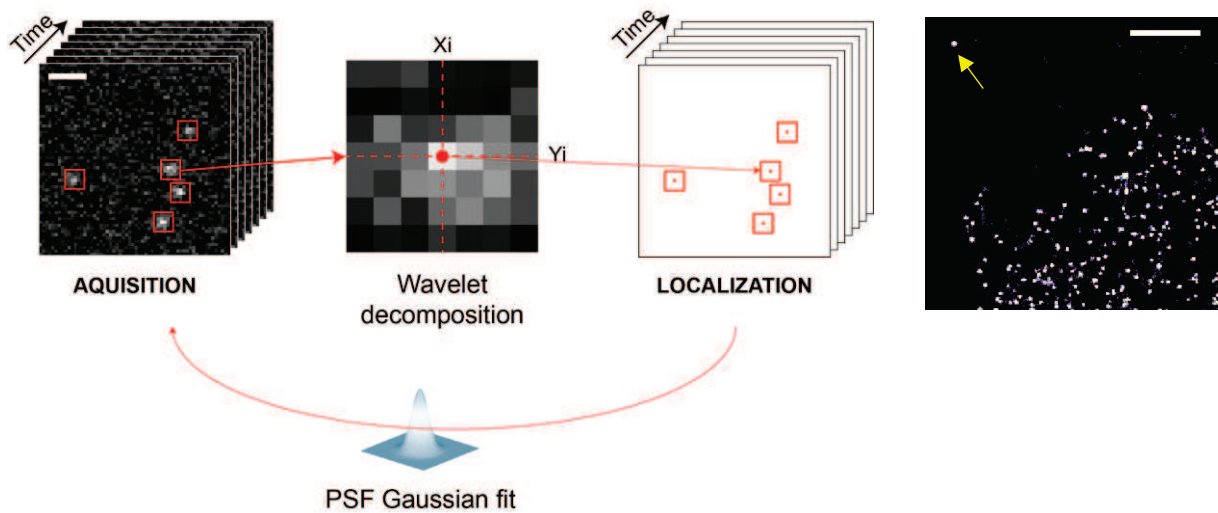


FIGURE 23: LOCALIZATIONS AND IMAGE RECONSTRUCTION.

After wavelet segmentation of the detections, a 2D isotropic Gaussian fit is applied on each PSF to determine the precise localization of the molecules. (scale bar: 2 μm).

After all fluorescent molecules have been imaged, corresponding localization points are summed to form the super-resolved pointillist image. (Right) example of a super-resolved image, with its fiducial marker (yellow arrow).

Enrichment of clusters is determined by wavelet segmentation based on areas with strong signal intensity compared with neighboring areas on the super-resolved dSTORM images (Izeddin et al., 2012; Kechkar et al., 2013). Domains are fitted with a 2D isotropic Gaussian, and domain size is extracted as the average full-width at half-maximum. The mean integrated intensity of a single probe non-specifically attached to the coverslip around each cell (removing the 5% smallest and largest domains) is used to normalize the integrated intensity of protein domains inside the cell (Figure 24), in order to estimate the number of probes in each cluster, using the following formula:

$$\text{number of objects per cluster} = \frac{\text{cluster integrated intensity}}{\text{mean integrated intensity of isolated probe}}$$

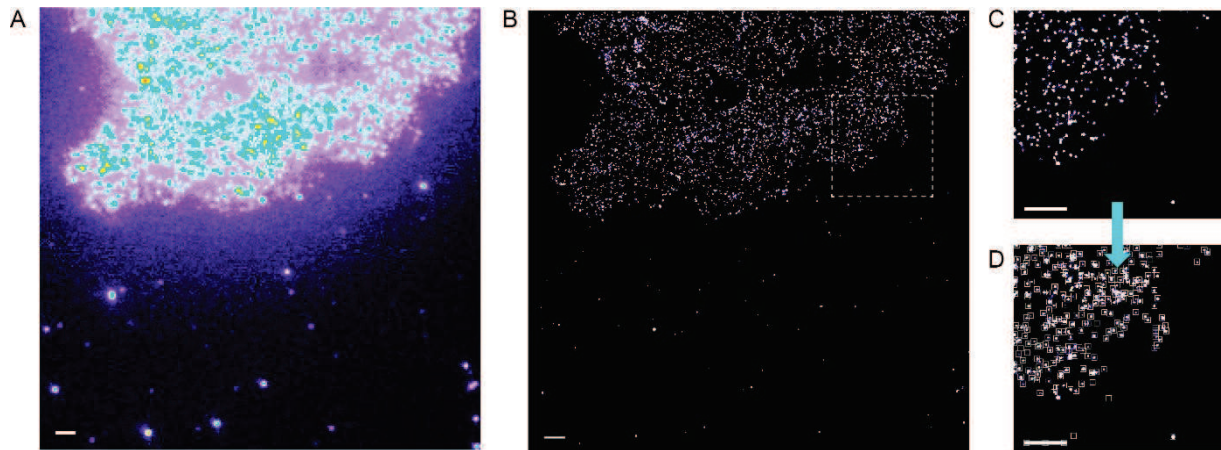


FIGURE 24: CLUSTER ANALYSIS

Representative cluster analysis on AP-GluK2 expressing COS-7, labeled with 58 nM of streptavidin-Alexa647.

(A) Low resolution streptavidin-Alexa647 labeling of AP-GluK2 expressed in COS-7. **(B)** dSTORM reconstructed image. **(C)** Zoom on a sub region. **(D)** Automatic cluster detection by the PalmTracer software. (Scale bar = 2 μ m)

In primary culture neurons, constructs are co-expressed with Homer1c-GFP as a post-synaptic marker or Vlut1-mCherry as a pre-synaptic marker, and an intensity threshold is applied on those signals to identify the post-synapse and the pre-synapse, respectively. The corresponding binary masks are used to sort single-particle data analyses to specific synaptic regions.

2.6. Statistical analysis

Every statistical analysis has been done with the non-parametric rank comparison Mann-Whitney test, using the GraphPad Prism 7 software. The corresponding P values are indicated as followed: ns: $P > 0,05$; *: $0,01 < P < 0,05$; **: $0,001 < P < 0,01$; ***: $0,0001 < P < 0,001$; ****: $P < 0,0001$.

Data are generally expressed as the mean \pm SEM, unless otherwise indicated.

– CHAPTER 3 –
Results

3.1. Characterization of the receptor stoichiometry

In order to ensure that the effect of the probe labeling on the diffusion and aggregation of the different receptors was due to the probe itself and not to a mis-folding of the proteins, I verified the stoichiometry of the β -neurexin1, neuroligin1 and GluK2 receptors in our hands, using a single photobleaching step counting technique.

Two days after transfection with the constructs GFP- β -nrxn1, nlg1-GFP or GluK2-GFP, HEK cells were lysed, and GFP-tagged receptors were immobilized on a passivated substrate to allow isolation of protein fluorescence. The coverglass was passivated with PEG containing 1% of biotinylated PEG on which neutravidin can attach. Neutravidin has 4 binding sites to biotin, allowing the binding of biotinylated antibodies against GFP on the passivated surface, which therefore, pull down the GFP-tagged protein of interest (**Figure 25A**). The average frequency distribution of the number of bleaching steps was plotted (**Figure 25B-D**). The observed distribution for GFP- β -nrxn1, nlg1-GFP and GluK2-GFP were best accounted for by a binomial calculated for 1 subunit, 2 subunits and 4 subunits respectively, with a probability of 0.8 that GFP is fluorescent. This probability of GFP maturation has been found in several previous studies (Bharill et al., 2014; Hastie et al., 2013; McGuire et al., 2012; Reiner, Arant, & Isacoff, 2012; M. H. Ulbrich & Isacoff, 2008; Maximilian H. Ulbrich & Isacoff, 2007). This result, in accordance with the literature, confirms that β -nrxn1, nlg1 and GluK2 form monomers, dimers, and tetramers in the plasma membrane. However, the neuroligin1-GFP elicits substantially more single photobleaching steps than the description by the binomial distribution for a dimer, suggesting that some of the neuroligins are still present in a monomeric fashion (**Figure 25C**). These results were compared with the GFP subunit counting of a nlg1 mutant that contains two point mutations (E584A/L585A) in the extracellular coiled-coiled region involved in the dimerization interface, designed to impair dimer formation (Dean et al., 2003): although the nlg1-E584A/L585A-GFP mutant, exhibits more single photobleaching steps, the single photobleaching step distribution of this mutant does not follow the description by the binomial distribution for a monomer either, suggesting that this mutant is still capable of forming a small fraction of dimers (**Figure 25E**).

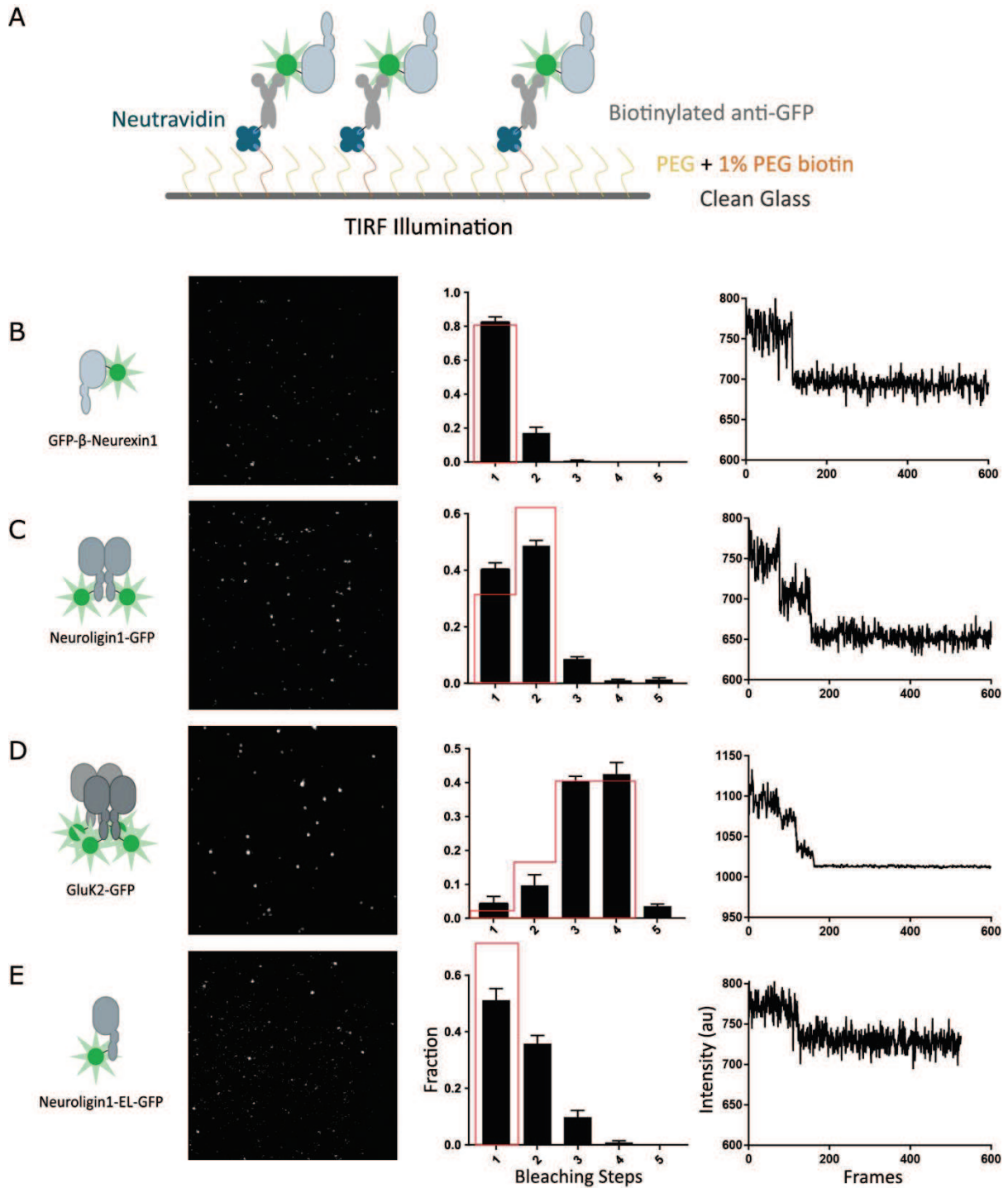


FIGURE 25. SINGLE-MOLECULE SUBUNIT COUNTING ON THE THREE MEMBRANE PROTEINS.

(A) Schematic of the single molecule pull down strategy. **(B-D)** Single-molecule irreversible photobleaching to count the number of GFP per fluorescent spot (e.g., number of subunits per labeled protein) in β -neurexin1 **(B)**, neuroligin1 **(C)**, GluK2 **(D)**, and neuroligin1-EL mutant **(E)**. (Left) Images show the first frame of the movie to indicate the density of molecules. (Middle) Average frequency distributions of the number of photobleaching steps (black bars) with error bars indicating SEM (GFP- β -nrxn1 N=5; nlgn1-GFP N=8; GluK2-GFP N=3; nlgn1-EL-GFP N=5). Red lines indicate the theoretical binomial distributions for complexes formed of 1, 2, and 4 subunits, respectively, with the probability of 0.8 that GFP is fluorescent. (Right) Representative fluorescence traces from single molecules showing one step **(B,E)**, two steps **(C)**, and four photobleaching steps **(D)**.

3.2. Effect of probe binding on the protein diffusion using uPAINT

To assess the impact of the probe valence and size on protein dynamics, I used uPAINT and measured the diffusion of **AP- β -nrxn1**, **AP-nlgn1** and **AP-GluK2** in COS-7 labeled with Atto-conjugated **monovalent streptavidin (mSA)**, **divalent anti-biotin antibody** or **tetravalent streptavidin**. The three probes were added at a low concentration to isolate single molecule diffusing at the plasma membrane, with a small risk of false-reconnection between two trajectories from different molecules.

The measured diffusion coefficient of the AP- β -nrxn1 labeled by the anti-biotin antibody is shifted towards lower values compared to the tracking with mSA-Atto594 or streptavidin-Atto594 (**Figure 26C,D,F**), and there is a concomitant increase in the percentage of slowly diffusing proteins (**Figure 26E**), defined as $D < 0.01 \mu\text{m}^2\text{s}^{-1}$. However, there was no significant effect of the probe valence, since AP- β -nrxn1 labeled with mSA-Atto594 and streptavidin-Atto594 exhibit similar diffusion coefficients D (**Figure 26F**). Interestingly, labeling with mSA-Atto594 leads to a small but statistically significant increase in the percentage of slowly diffusing AP- β -nrxn1 compared to streptavidin-Atto594 (**Figure 26E**). A first hypothesis, based on the lower biotin affinity of the mSA ($K_d = 2.8 \text{ nM}$ versus 10^{-15} M for streptavidin, Chamma et al., 2016; Weber et al., 1989), is that unspecific binding of the mSA is contaminating the diffusion coefficient measured, highlighting the importance of specific labeling when using uPAINT (Giannone et al., 2013a). A second hypothesis, consistent with the FRAP results (e.g. **3.3. Effect of probe binding on the protein diffusion using FRAP, Figure 32**), would be that the labelling with streptavidin, but not with the small mSA-Atto594 leads to the covering of a non-specific binding site on the AP- β -nrxn1, preventing its interaction with the substrate or coverglass.

Together, these results suggest that the size more than the valence of the probe affect the diffusion of AP- β -nrxn1, when measured in uPAINT experiments.

On the other hand, the diffusion of the AP-nlgn1 and AP-GluK2 remained unchanged whatever the valence and the size of the probe used (**Figure 27, Figure 28**), suggesting that this parameter has little no effect on the diffusion of freely moving membrane proteins measured in uPAINT experiments. One explanation for these unexpected results is that at low ligand

concentration such as the one used for uPAINT, the ligand does not have the power to cross-link target proteins and may bind to only a couple (antibodies) or to four molecules (streptavidin), which is not sufficient to significantly decrease the diffusion coefficient of the complex. Interestingly, two distinct populations can be visible, for the diffusion of AP-nlgn1 and AP-GluK2, probably corresponding to freely diffusing protein *versus* diffusion of bound molecules (**Figure 27D, Figure 28D**).

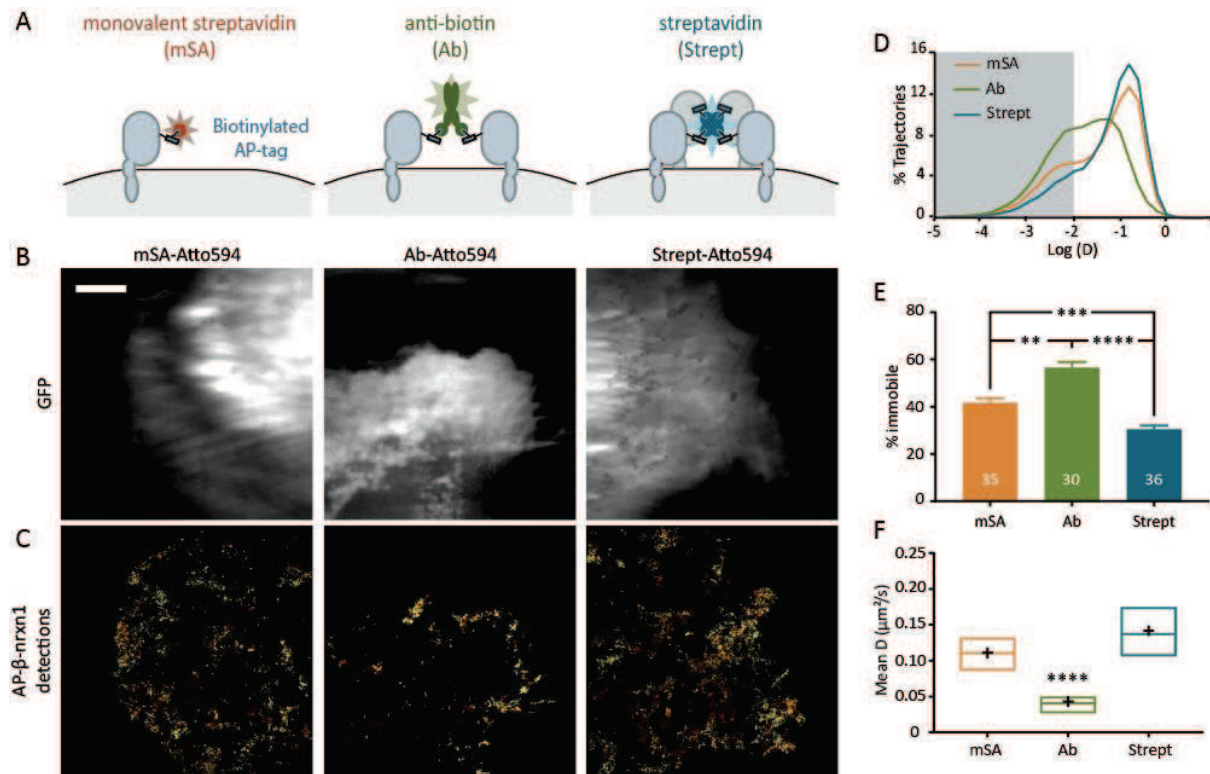


FIGURE 26. UPaint of AP-β-nrxn1 with MSA or biotin antibody or streptavidin.

(A) Schematic diagram of AP-β-nrxn1 labeled with three different probes (mSA, monoclonal biotin antibody or streptavidin), conjugated to Atto 594. **(B)** Examples of COS-7 cells co-expressing GFP as a volume marker, AP-β-nrxn1 and BirA^{ER}, and labeled as described above (Scale bar, 10 μm). **(C)** AP-β-nrxn1 trajectories in the same cells, calculated from stacks of 4,000 images with 20 ms exposure time. **(D)** Distribution of AP-β-nrxn1 diffusion coefficient in a semi-log plot, where the grey shaded area represents slow trajectories ($D < 0.016 \mu\text{m}^2/\text{s}$). **(E)** Corresponding percentage of slow trajectories measured in the three different conditions (**** $p < 0.0001$; *** $p < 0.001$; ** $p < 0.01$). **(F)** Corresponding diffusion coefficient median for the three different conditions, the means are marked by a + on the graph (**** $p < 0.0001$). Numbers in the bar charts represent the number of cells analyzed.

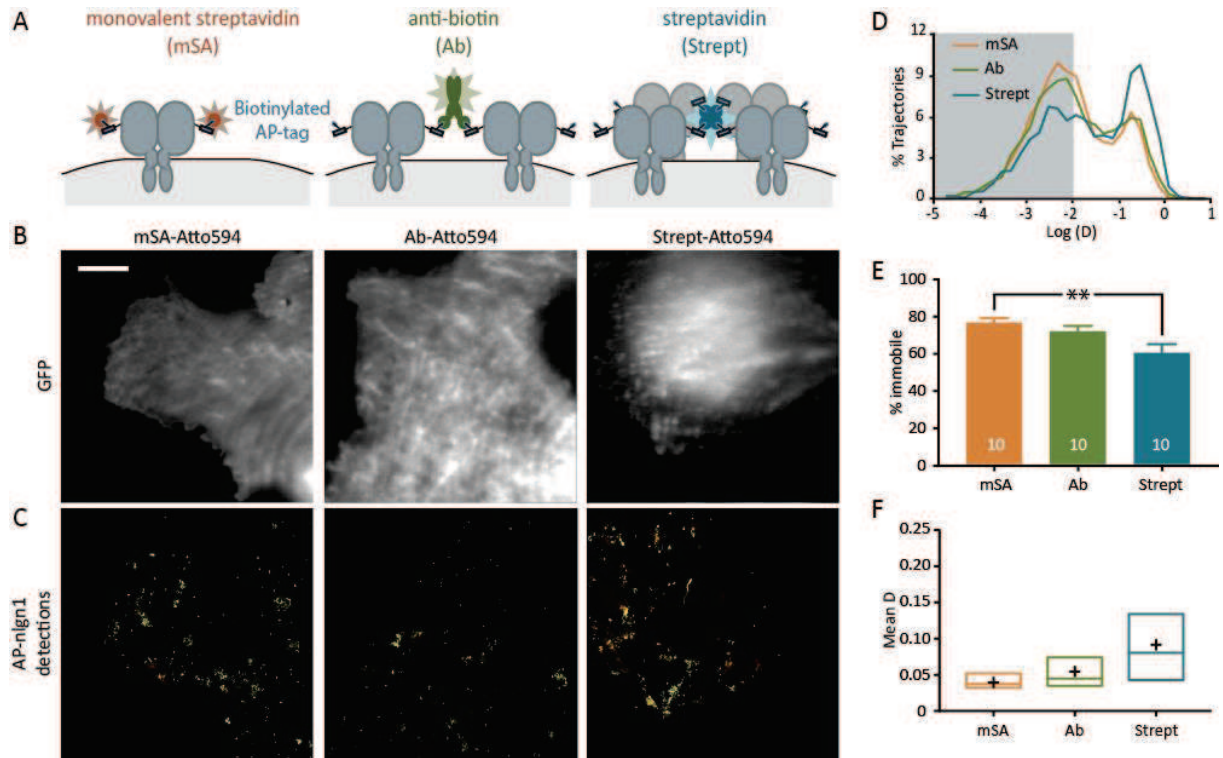


FIGURE 27. UPaint of AP-NLGN1 with mSA or biotin antibody or streptavidin.

(A) Schematic diagram of AP-nlgn1 labeled with three different probes (mSA, monoclonal biotin antibody or streptavidin), conjugated to Atto 594. **(B)** Examples of COS-7 cells co-expressing EGFP as a volume marker, AP-nlgn1 and BirA^{ER}, and labeled as described above (Scale bar, 10 μm). **(C)** AP-nlgn1 trajectories in the same cells, calculated from stacks of 4,000 images with 20 ms exposure time. **(D)** Distribution of AP-nlgn1 diffusion coefficient in a semi-log plot, where the grey shaded area represents slow trajectories ($D < 0.016 \mu\text{m}^2/\text{s}$). **(E)** Corresponding percentage of slow trajectories measured in the three different conditions (** $p < 0.01$). **(F)** Corresponding diffusion coefficient median for the three different conditions, the means are marked by a + on the graph. Numbers in the bar charts represent the number of cells analyzed.

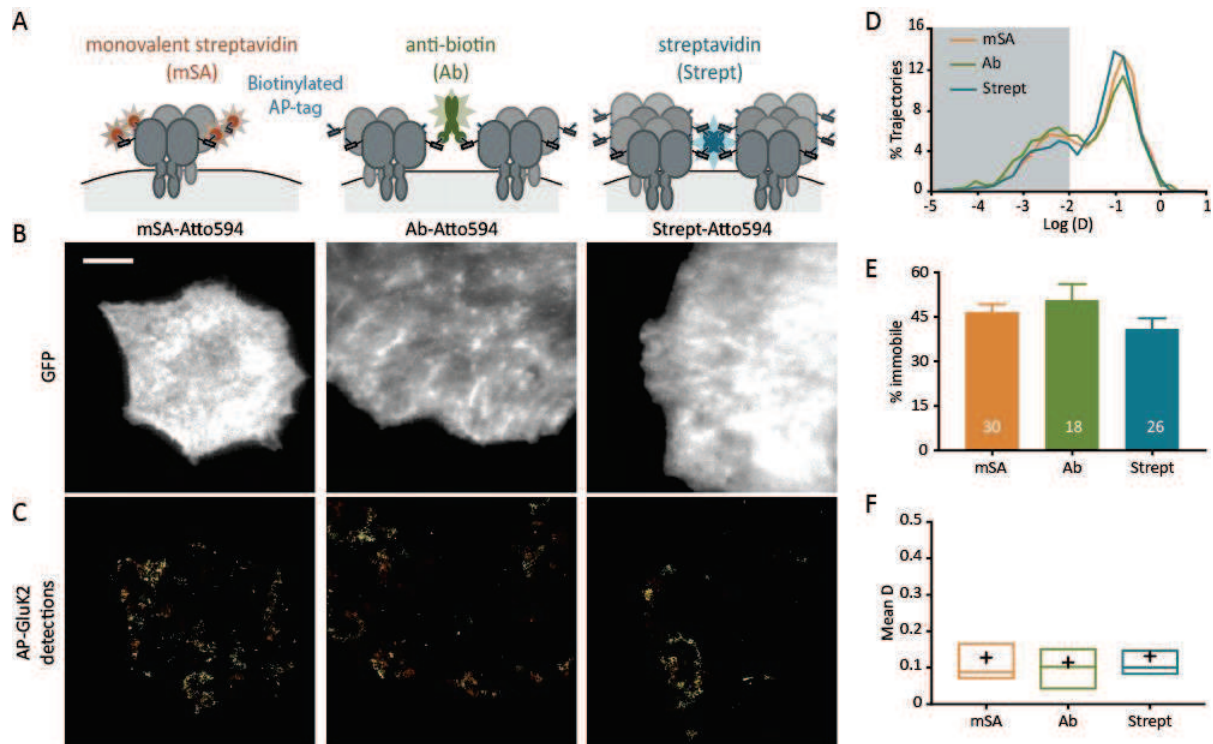


FIGURE 28. UPaint of AP-Gluk2 with mSA or biotin antibody or streptavidin.

(A) Schematic diagram of AP-Gluk2 labeled with three different probes (mSA, monoclonal biotin antibody or streptavidin), conjugated to Atto 594. (B) Examples of COS-7 cells co-expressing EGFP as a volume marker, AP- Gluk2 and BirA^{ER}, and labeled as described above (Scale bar, 10 μm). (C) AP- Gluk2 trajectories in the same cells, calculated from stacks of 4,000 images with 20 ms exposure time. (D) Distribution of Gluk2 diffusion coefficient in a semi-log plot, where the grey shaded area represents slow trajectories ($D < 0.016 \mu\text{m}^2/\text{s}$). (E) Corresponding percentage of slow trajectories measured in the three different conditions. (F) Corresponding diffusion coefficient median for the three different conditions, the means are marked by a + on the graph. Numbers in the bar charts represent the number of cells analyzed.

Importantly, comparison between AP-GluK2 diffusion at the beginning of the experiment, shortly after incubation with streptavidin-Atto594 and after 30 min show no difference, nor in the percentage of slow trajectories, nor in the mean diffusion coefficient measured, suggesting that equilibrium in terms of interaction complexes is already reached (**Figure 29**).

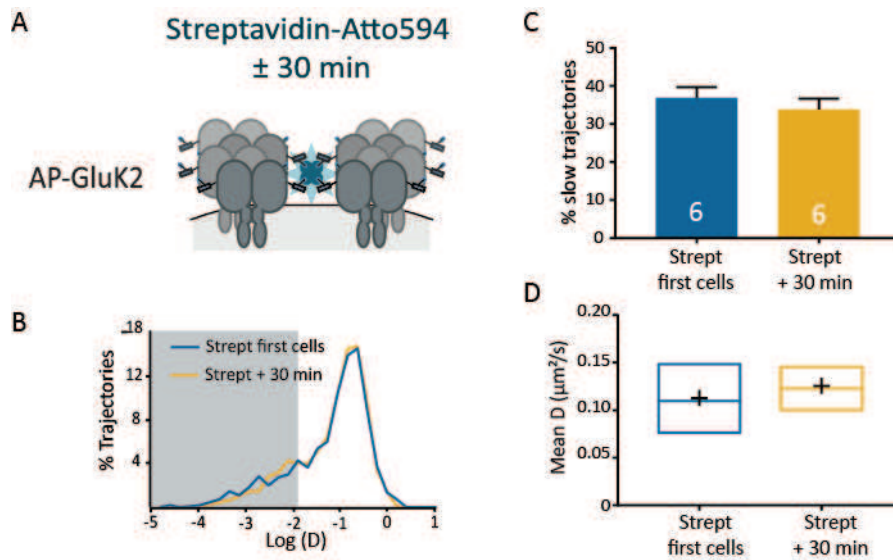


FIGURE 29: EFFECT OF INCUBATION TIME OF STREPTAVIDIN-ATTO594 ON THE DIFFUSION OF AP-GLUK2 USING uPAINT.

(A) Schematic diagram of AP-GluK2 labeled with streptavidin-Atto 594. (B) Distribution of GluK2 diffusion coefficient at $t = 0$ (first two cells of the experiment) and after 30 min in a semi-log plot, where the grey shaded area represents slow trajectories ($D < 0.01 \mu\text{m}^2/\text{s}$). (C) Corresponding percentage of slow trajectories, measured in the two different conditions. (D) Corresponding diffusion coefficient median for the two different conditions, the means are marked by a + on the graph. Numbers in the bar charts represent the number of cells analyzed.

To assess the impact of the probe concentration on the diffusion of the proteins, I performed uPAINT on AP-GluK2 using streptavidin-Atto594 at low concentration and non-conjugated neutravidin at saturating concentration (58 nM), compared with streptavidin-Atto594 alone. The measured diffusion coefficient of the AP-GluK2 is shifted towards lower values (**Figure 30C-D**), and there is a concomitant increase in the percentage of slowly diffusing protein (**Figure 30E**), defined as $D < 0.01 \mu\text{m}^2/\text{s}^{-1}$, when neutravidin is added to the labeling solution.

Altogether, these results suggest that even if the probe valence and size do not seem to affect the diffusion of freely moving membrane protein measured by uPAINT experiments, it might affect the diffusion measured by techniques relying on saturating labeling.

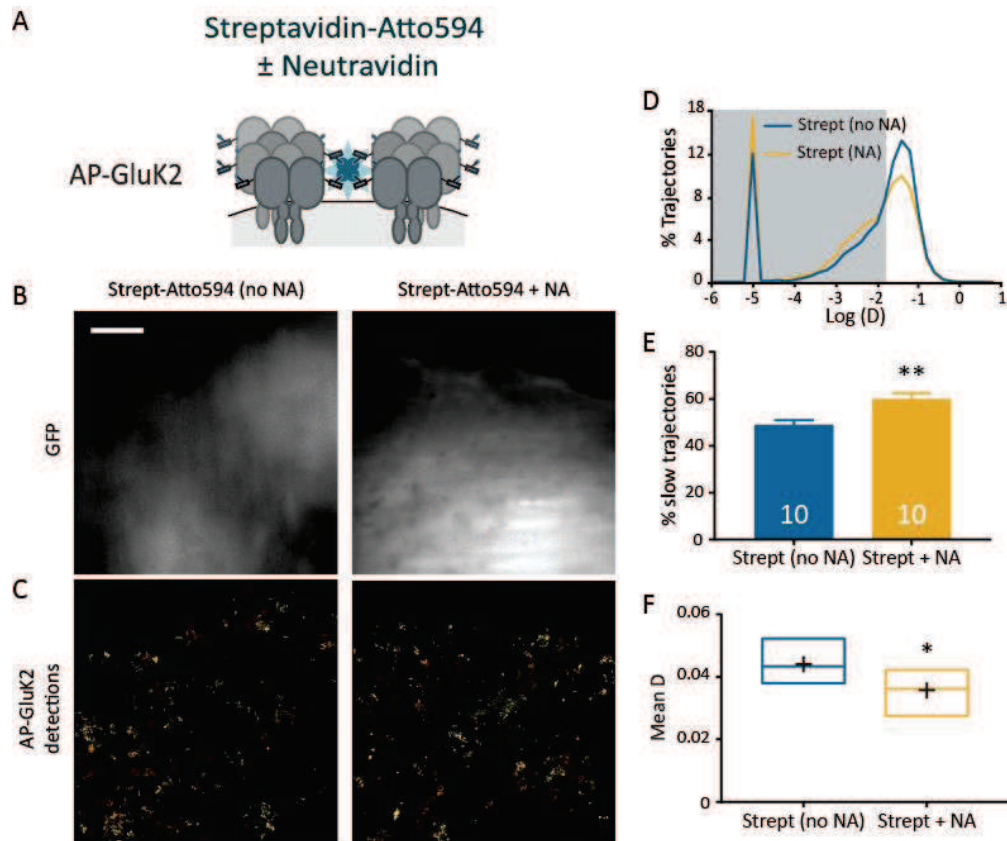


FIGURE 30: EFFECT OF THE CONCENTRATION OF THE PROBE ON THE DIFFUSION OF AP-GLUK2 USING uPAINT.

(A) Schematic diagram of AP-GluK2 labeled with streptavidin-Atto 594. Non-fluorescent neutravidin (NA) was added or not to the labeling medium to mimic clustering induced by saturating labeling. **(B)** Examples of COS-7 cells co-expressing EGFP as a volume marker, AP- Gluk2 and Bir^{ER}, and labeled as described above (Scale bar, 10 μm). **(C)** AP- Gluk2 trajectories in the same cells, calculated from stacks of 4,000 images with 20 ms exposure time. **(D)** Distribution of Gluk2 diffusion coefficient in a semi-log plot, where the grey shaded area represents slow trajectories. **(E)** Corresponding percentage of slow trajectories ($D < 0.01 \mu\text{m}^2/\text{s}$), measured in the two different conditions (** $p < 0.01$). **(F)** Corresponding diffusion coefficient median for the two different conditions, the means are marked by a + on the graph (** $p < 0.001$). Numbers in the bar charts represent the number of cells analyzed.

3.3. Effect of probe binding on the protein diffusion using FRAP

While uPAINT allows a precise determination of diffusion coefficients in specific sub-domains, FRAP has the salient advantage to access long dwell times, and dynamics at the population level. If FRAP is usually performed on recombinant proteins tagged with a fluorescent protein such as GFP or RFP, some studies prefer to use conjugated antibodies to assess the diffusion of endogenous proteins. In this case, proteins of interest are labeled using a saturating concentration of specific conjugated antibodies. As suggested by the uPAINT results (Figure 30), the labeling with saturating concentration of multivalent probes may lead to clustering of the proteins, and therefore, a slowing down of protein diffusion.

To study the impact of probe valence and size on protein diffusion measured by FRAP, COS-7 cells expressing AP- β -neurexin1, AP-neurologin1 or AP-GluK2 were labeled with a saturating concentration (58 nM) of **monovalent** streptavidin (mSA), **divalent** streptavidin (dSA), **divalent** anti-biotin antibody, or streptavidin (**tetravalent**), all conjugated to Atto594 (Figure 31). FRAP was measured for 3 min (Figure 31A-D), and recovery curves were fitted with a diffusion equation to obtain the diffusion coefficient D (Figure 31E), and the immobile fraction (Figure 31F).

Surprisingly, AP- β -nrxn1 exhibited a higher immobile fraction when labeled with mSA-Atto594 than with streptavidin-Atto594. However, AP-nlgn1 and AP-GluK2 labeled with mSA exhibit lower immobile fraction than when labeled with streptavidin, suggesting the mSA labeling is not responsible for protein immobilization (Figure 31A,B,F). To understand if this behavior was specific for β -nrxn1, I compared the FRAP on the AP- β -nrxn1 labeled with mSA-Atto594, with the one on GFP- β -nrxn1 (Figure 32). GFP- β -nrxn1 seems to have a higher diffusion coefficient (to be confirmed with bigger N) than AP- β -nrxn1 labelled with mSA-Atto594 (Figure 32B,C), which can be due to unspecific binding of the probe to other targets, and exhibits a very small immobile fraction (<10%) (Figure 32B,D). Interestingly, GFP- β -nrxn1 lacks 4 amino acids from the original sequence of β -nrxn1 (GLAN located at 1088 amino acids from the N-terminal), while AP- β -Nrnxn-1 has those 4 amino acids. Our hypothesis is that the presence of this stretch of amino-acids is linked to the slowing down of AP- β -nrxn1. Labeling with streptavidin-Atto594, induced a slowing down in the AP- β -nrxn1 diffusion measured by FRAP (Figure 32B,C), but restored the immobile fraction to levels comparable to the GFP- β -nrxn1 (Figure 32B,D), suggesting that the clustering induced by streptavidin labeling masked the

unspecific binding sequence of the β -nrxn1 to the substrate. To have a better understanding of the effect of probe valence and size on monomeric transmembrane proteins, we used an AP-Transmembrane-domain (AP-TMD) construct, which showed similar diffusion coefficient and immobile fraction as GFP- β -nrxn1 ([Figure 32](#)).

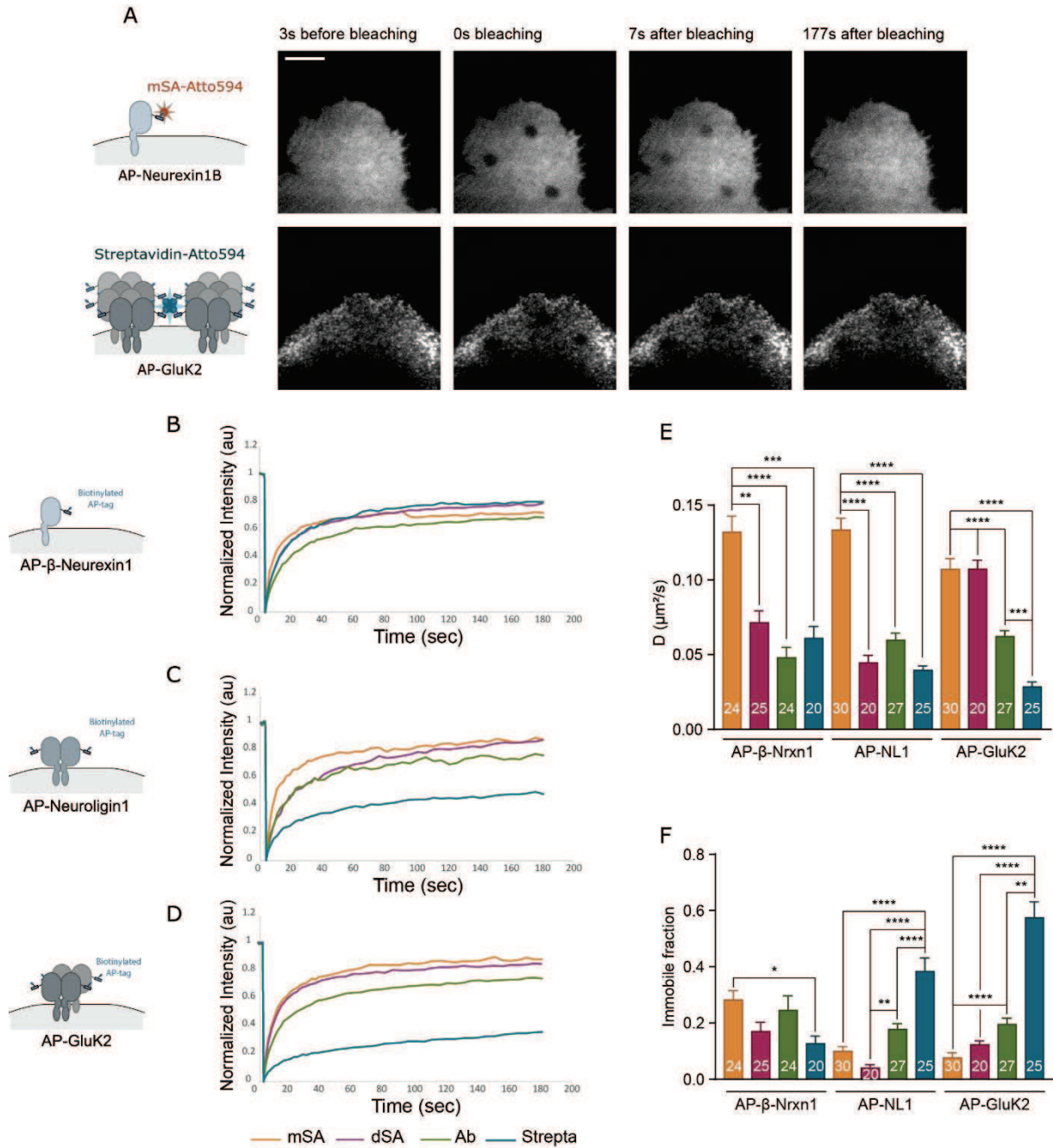


FIGURE 31. FRAP EXPERIMENTS ON AP-β-NRXN1, AP-NLGN1 AND AP-GLUK2, LABELED WITH MSA, DSA, ANTI-BIOTIN ANTIBODY, OR STREPTAVIDIN.

(A-F) FRAP experiments performed on AP-β-Neurexin1 (B), AP-Neuroigin1 (C), and AP-GluK2 (D) labelled with mSA-Atto594 (brown), dSA-Atto594 (violet), Anti-biotin-Atto594 (green) or Streptavidin-Atto594 (Blue). (A) Images show the first frame 3 s before photobleaching, the fifth frame during photobleaching, the eighth frame 7 s after photobleaching and the last frame of a standard FRAP experiment movie (Scale bar, 10 μm). (B-D) corresponding normalized fluorescence recovery curves. (E-F) Bar graph of the diffusion coefficients D (E) and the immobile fractions (F) obtained after fitting each data point with a diffusion equation. (Three different experiments per condition, mean with SEM represented, one-way analysis of variance followed by Kruskal-Wallis test, * $p < 0.05$; ** $p < 0.01$; *** $p < 0.001$, **** $p < 0.0001$). Numbers in the bar charts represent the number of cells analyzed.

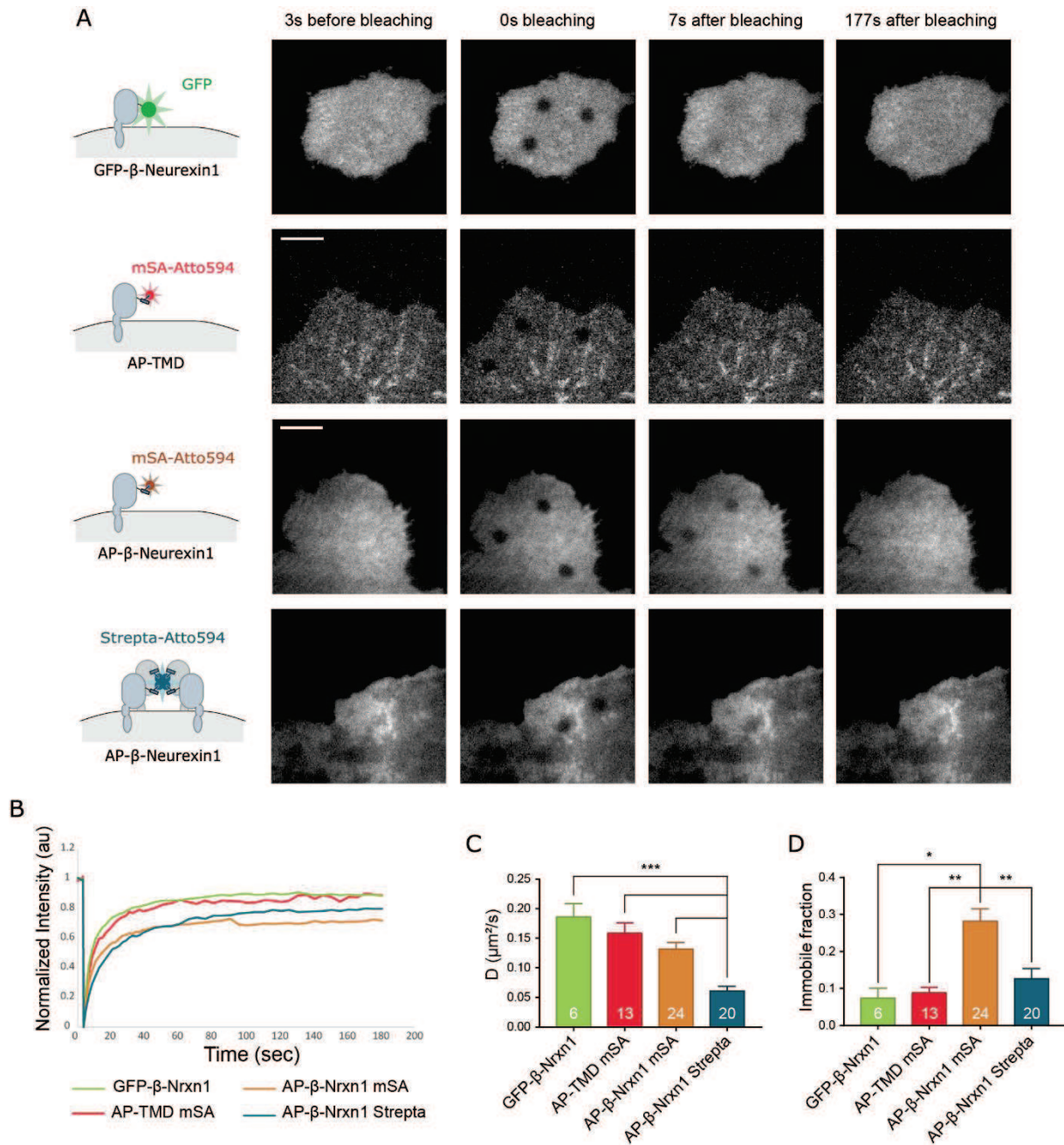


FIGURE 32. FRAP EXPERIMENTS ON AP-β-NRXN1 LABELED WITH MSA OR STREPTAVIDIN COMPARED TO GFP-β-NRXN1 AND AP-TMD LABELED WITH MSA.

(A) (left) Schematic diagram of the different proteins with their label. (Right) Images show the first frame 3s before photobleaching, the fifth frame during photobleaching, the eighth frame 7s after photobleaching and the last frame of a standard FRAP experiment movie (Scale bar 10 μm). (B) corresponding normalized fluorescence recovery curves. (C-D) Bar graph of the diffusion coefficients D (C) and the immobile fractions (D) obtained after fitting each data point with a diffusion equation. (Mean with SEM represented, one-way analysis of variance followed by Kruskal-Wallis test, * $p < 0.05$; ** $p < 0.01$; *** $p < 0.001$). Numbers in the bar charts represent the number of cells analyzed.

FRAP experiments on COS-7 expressing AP-TMD, AP-neurologin1 or AP-GluK2 labeled with either Atto594 conjugated mSA, dSA, divalent anti-biotin antibody, or streptavidin showed that even if probe size and valence does not seem to affect protein diffusion when low concentrations are used (uPAINT), saturating concentration leads to severe cross-linking of the proteins (**Figure 33**). Indeed, a drastic reduction of the diffusion coefficient can be measured (**Figure 33E**), as well as an increased immobile fraction (**Figure 33F**), when multivalent probes were used. However, it seems that doubling the size of the diffusing transmembrane complex does not affect significantly their diffusion, as AP-TMD labeled with mSA, dSA or AP-nlgn1 labeled with mSA have similar diffusion coefficients (**Figure 33E**). It is to be noted that AP-TMD labeled with streptavidin-Atto594 and AP-GluK2 labeled with mSA-Atto594 display similar diffusion coefficients, in accordance with the presumed stoichiometry of the transmembrane proteins (**Figure 33E**). On the other hand, labeling with antibody affects monomeric, dimeric and tetrameric protein diffusion in the same way, with a concomitant decrease in diffusion coefficients and increase of the immobile fractions of the proteins (**Figure 33E**). However, although dSA labeling leads to a twofold decrease in the diffusion coefficient of AP-nlgn1 compared to mSA, it does not impact AP-GluK2 diffusion (**Figure 33E**). One hypothesis is that the AP-sites on GluK2 are close enough for the dSA to bind two subunits of the same receptor, thus there would be no clustering due to the labeling. Clustering with the streptavidin leads to a general decrease in the measured diffusion coefficient of membrane proteins, that intensifies when the number of binding sites augments on the targeted protein (**Figure 33E**).

Likewise, the immobile fraction correlates with the coefficient diffusion of the labeled protein, and is drastically increased with protein clustering (**Figure 33F**). Surprisingly, the immobile fraction of the AP-TMD labeled with the antibody is extremely high, comparable to that of the AP-GluK2 clustered by the streptavidin, suggesting unspecific binding of the probe or changes in the protein organization (**Figure 33E**).

Finally, labeling with mSA leads to highest diffusion coefficient and least protein immobilization, consistent with its small size and monovalence (**Figure 33E,F**).

Overall, these results suggest that, while low concentration labeling used for uPAINT relies on probe specificity, techniques using saturating concentration of probes should take into

account probe size and valence, especially when targeting multiple sites on the protein of interest (e.g. polyclonal antibodies, or monoclonal antibodies targeting a multimeric protein).

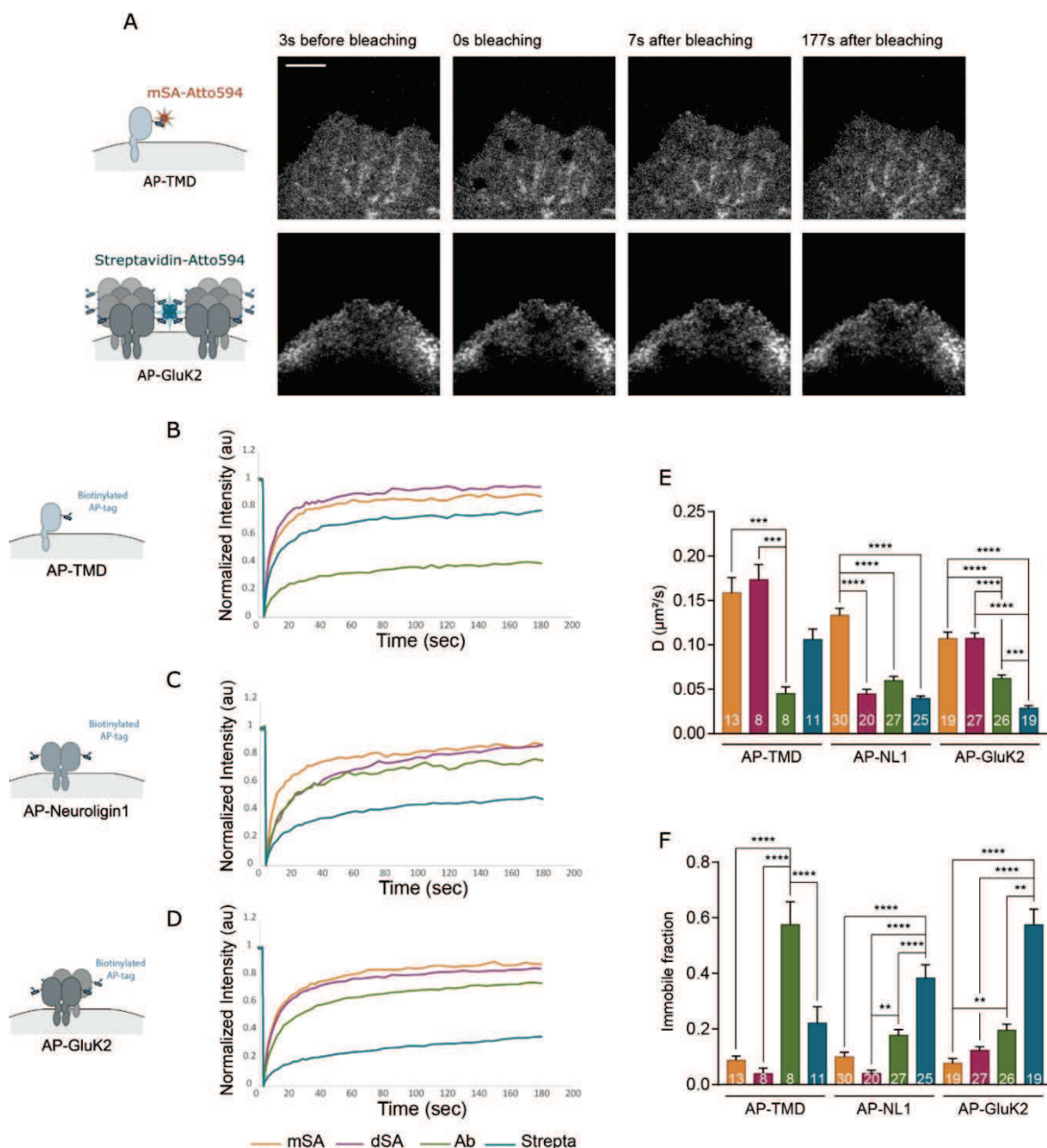


FIGURE 33: FRAP EXPERIMENTS ON AP-TMD, AP-NLGN1 AND AP-GLUK2, LABELED WITH MSA, DSA, ANTI-BIOTIN ANTIBODY, OR STREPTAVIDIN.

(A-F) FRAP experiments performed on AP-TMD (B), AP-Neuroigin1 (C), and AP-GluK2 (D) labelled with mSA-Atto594 (brown), dSA-Atto594 (violet), Anti-biotin-Atto594 (green) or Streptavidin-Atto594 (Blue). (A) Images show the first frame 3s before photobleaching, the fifth frame during photobleaching, the eighth frame 7s after photobleaching and the last frame of a standard FRAP experiment movie (Scale bar 10 μm). (B-D) corresponding normalized fluorescence recovery curves. (E-F) Bar graph of the diffusion coefficients D (E) and the immobile fractions (F) obtained after fitting each data point with a diffusion equation. (Mean with SEM represented, one-way analysis of variance followed by Kruskal-Wallis test, *p<0.05; **p<0.01; ***p<0.001, ****p<0.0001). Numbers in the bar charts represent the number of cells analyzed

3.4. Effect of probe binding on protein aggregation level

In order to build appropriate models of complex cellular activities, such as synapse formation or even synaptic transmission, it is fundamental to obtain absolute numbers of the proteins involved. While dSTORM has the striking advantage to be a technique that can be applied on endogenous proteins, *via* labeling with conjugated antibodies, this method relies on saturating labeling, therefore the use of multivalent probes may lead to protein clustering or mislocalization. To study the impact of probe valence and size on protein aggregation in dSTORM, COS-7 cells expressing AP-TMD, AP- β -nrxn1, AP-neurologin1 or AP-GluK2 were labeled with a high concentration (58 nM) of **monovalent** streptavidin (mSA), **divalent** streptavidin (dSA), **divalent** anti-biotin antibody, or **tetravalent** streptavidin, all conjugated to alexa647 (**Figure 34**).

The AP-TMD labeled with anti-biotin-Alexa647 displays a labeling of the protein enriched at the “edge”, suggesting that TMDs labeling with the antibody leads to changes in the localization and organization of the protein at the cell surface (**Figure 34A**). Yet, this behavior is not observed for the other proteins labeled with this probe (**Figure 34B-D**). This result is consistent with the low diffusion coefficient and large immobile fraction of the TMD labeled with the biotin antibody conjugated to Atto594 observed during FRAP experiments (**Figure 33B,E,F**).

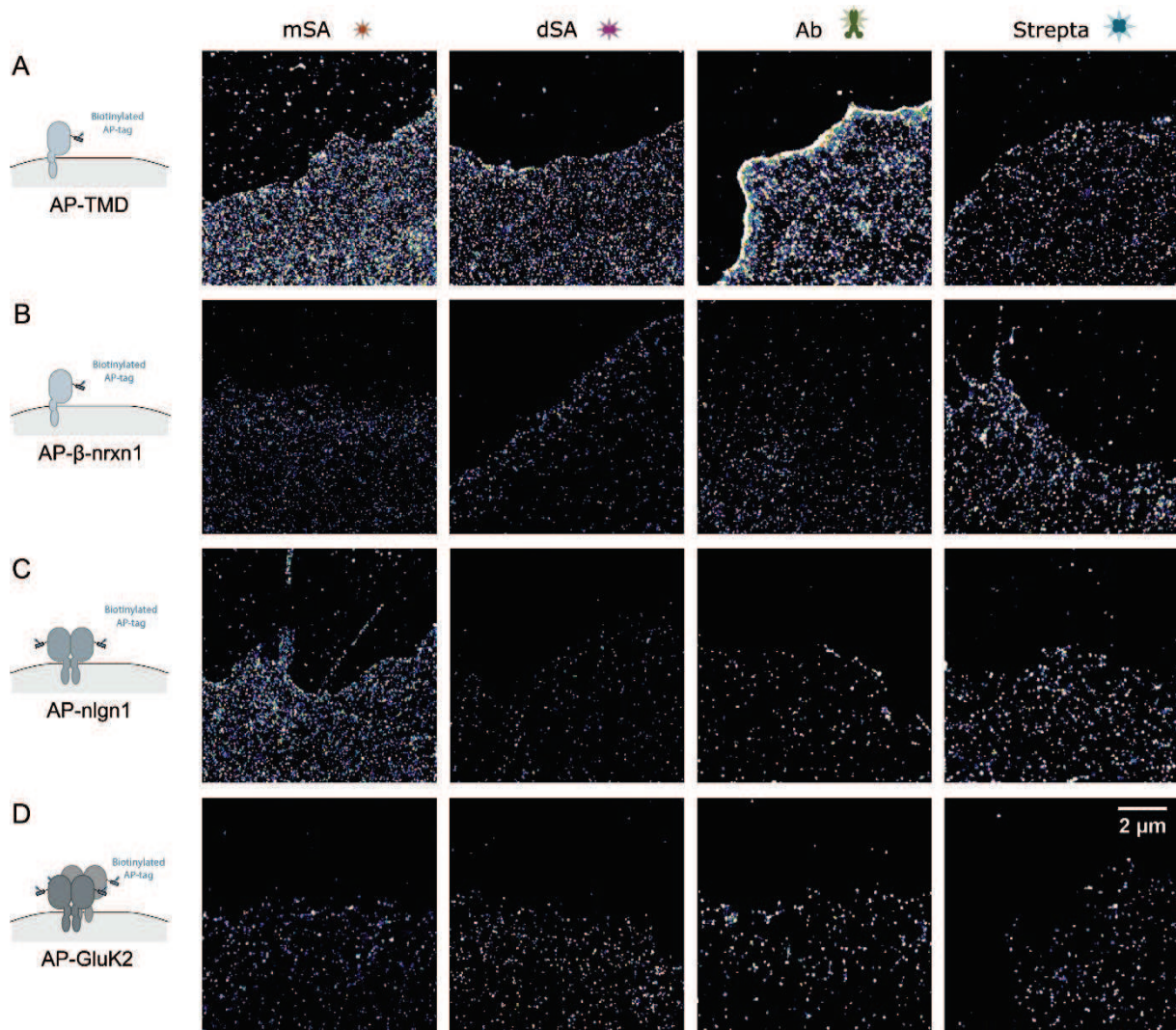


FIGURE 34: dSTORM OF AP-TMD, AP-β-NRXN1, AP-NLGN1 AND AP-GLUK2, LABELED WITH MSA, DSA, ANTI-BIOTIN ANTIBODY, OR STREPTAVIDIN.

(left) Schematic diagram of the different proteins, (Right) typical dSTORM image reconstruction of COS-7 cells expressing AP-TMD (A), AP-β-nrxn1 (B), AP-nlgn1 (C) and AP-GluK2 (D), labeled with four different probes (mSA, dSA, monoclonal anti-biotin antibody, or streptavidin) conjugated to alexa647.

3.4.1. Effect of probe size and valence on nanoscopic organization of the monomeric proteins AP-TMD and AP- β -nrxn1

The AP-TMD possesses only one AP-tag, therefore, allowing the binding of one probe at a time (**Figure 35A**), which is consistent with an average number of mSA per cluster close to 1. Surprisingly, around 8 streptavidins and 7 anti-biotin antibodies can be counted per cluster, suggesting a clustering of those probes (**Figure 35D**). Clustering can be triggered by the aggregation of TMD itself, however, it is unclear why the protein would not cluster when labeled with mSA (**Figure 35D**). A hypothesis is that the TMD is clustered the same way with all the different probes, but due to a lower degree of labeling for mSA and dSA, some of the probes bound are not conjugated to Alexa647, and therefore, not visible. Indeed, the approximation of the number of probes in each cluster, by normalizing the cluster integrated intensity by the mean integrated intensity of a single probe non-specifically immobilized on the coverslip next to the cell studied, can lead to an under estimation of a number of objects, since only conjugated probes are visible and taken into account. However, TMD labeled with the small monovalent mSA displays a fast diffusion coefficient and a low immobile fraction measured by FRAP, more consistent with TMD being in a monomeric form (**Figure 33B,E,F**). The TMD used for the different experiments is a pdisplay containing multiple tags (HA-6His-AP-CFP). To ensure its stoichiometry, photobleaching step counting could be performed, for example on its CFP tag.

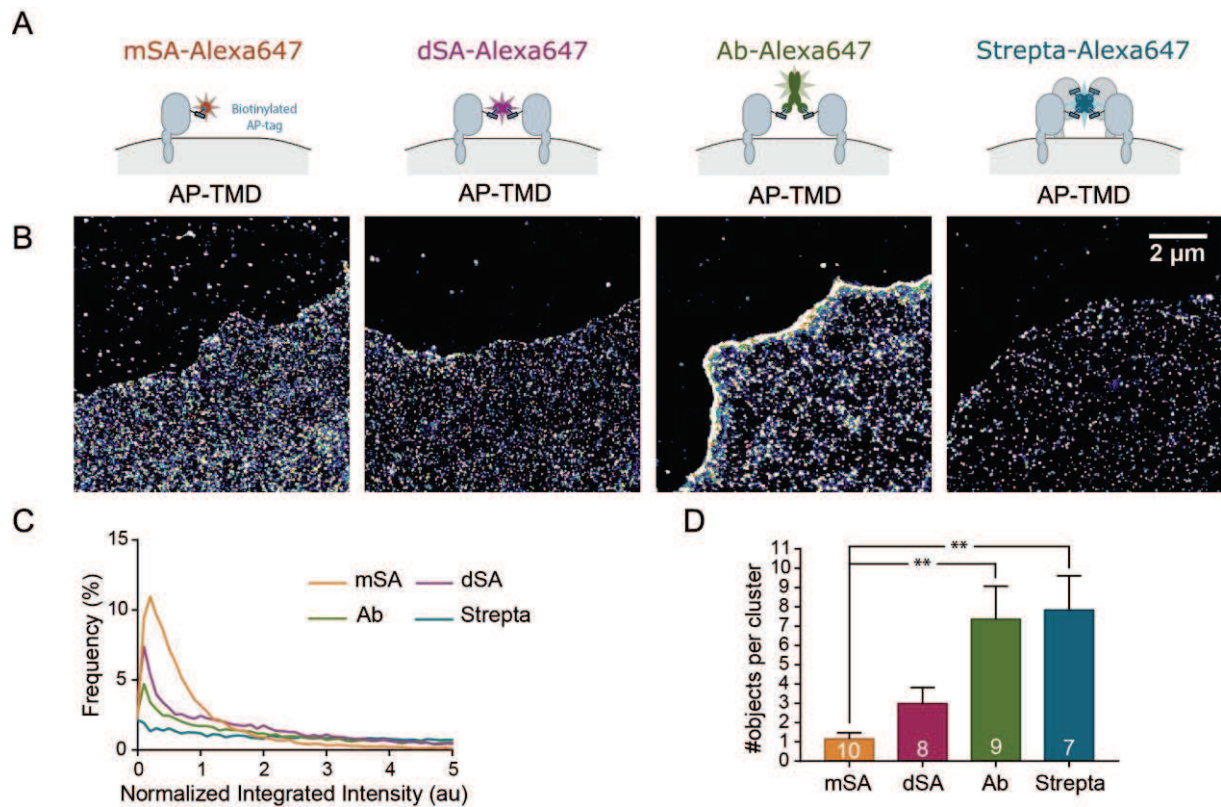


FIGURE 35: dSTORM OF AP-TMD LABELED WITH mSA, dSA, ANTI-BIOTIN ANTIBODY, OR STREPTAVIDIN CONJUGATED TO ALEXA647.

(A) Schematic diagram of the AP-TMD labeled with the four different probes conjugated to alexa647. **(B)** Typical dSTORM image reconstruction of AP-TMD expressing cos-7 labeled with mSA-Alexa647, dSA-Alexa647, monoclonal anti-biotin antibody-Alexa647 (Ab), or streptavidin-Alexa647 (Strepta). **(C)** Frequency distribution of the normalized integrated intensity measured for the four different probes (mSA N=10; dSA N=8; Ab N=9; Strepta N=7 cells). **(D)** Bar graph of the number of object per cluster measured for the four different probes. (Mean with SEM represented, one-way analysis of variance followed by Kruskal-Wallis test, $**p < 0.01$). Numbers in the bar charts represent the number of cells analyzed.

As for the AP-TMD, AP- β -nrxn1 possesses only one AP-tag, therefore, allowing the binding of one probe at a time (Figure 36A). Yet, it seems that the protein aggregates independently from the probe valence, as shown by the very wide distribution of the normalized integrated intensity for the different probes (Figure 36C), interestingly, those results are consistent with the diffusion behaviors and immobilization observed with uPAINT and FRAP (Figure 26, Figure 31B,F). No significant effect of the probe size and valence can be observed on the number of objects per cluster, with on average 2 mSA, 2 dSA, 2 streptavidins, and around 5 anti-biotin antibodies counted per cluster of labeled AP- β -nrxn1 (Figure 36D).

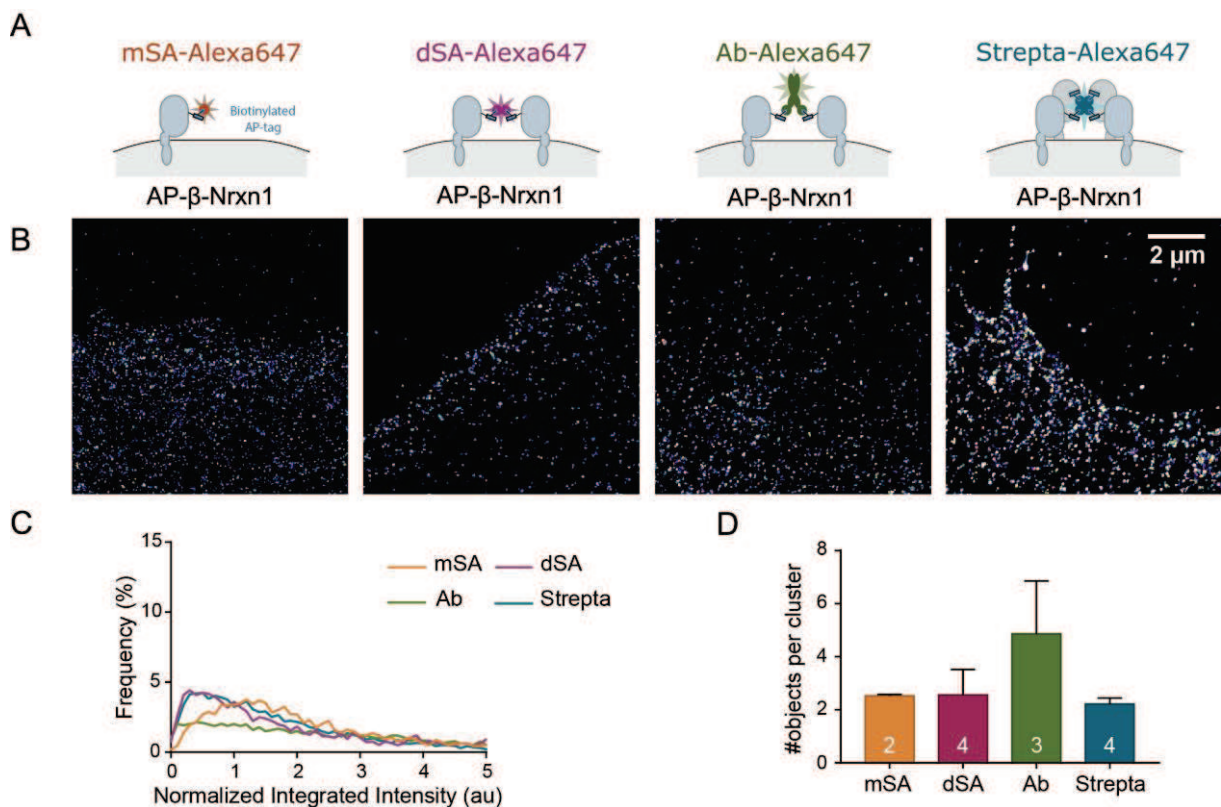


FIGURE 36: dSTORM OF AP- β -NRXN1 LABELED WITH MSA, dSA, ANTI-BIOTIN ANTIBODY, OR STREPTAVIDIN CONJUGATED TO ALEXA647.

(A) Schematic diagram of the AP- β -nrxn1 labeled with the four different probes conjugated to alexa647. (B) Typical dSTORM image reconstruction of AP- β -nrxn1 expressing cos-7 labeled with mSA-Alexa647, dSA-Alexa647, monoclonal anti-biotin antibody-Alexa647 (Ab), or streptavidin-Alexa647 (Strepta). (C) Frequency distribution of the normalized integrated intensity measured for the four different probes (mSA N=2; dSA N=4; Ab N=3; Strepta N=4 cells). (D) Bar graph of the number of object per cluster measured for the four different probes. (Mean with SEM represented). Numbers in the bar charts represent the number of cells analyzed.

3.4.2. Effect of probe size and valence on AP-nlgn1 dimer nanoscopic organization

On the other hand, photobleaching step counting showed that nlgn1 forms a majority of dimers (**Figure 25C**). Therefore, labeling with mSA-Alexa647 should lead to a one to two ratio, whereas labeling with dSA, antibiotin and streptavidin can lead to further protein clustering by reaching out other dimers (**Figure 37A**). Yet, no significant difference can be noticed in the number of objects when AP-nlgn1 is labeled with mSA, dSA or anti-biotin antibody conjugated to Alexa647 (**Figure 37D**). On average, one mSA per cluster of nlgn1 can be counted, suggesting that some of the mSA is not conjugated to Alexa647 or the labeling is not saturating the AP sites (**Figure 37D**). However, the high non-specific binding of the mSA-Alexa647 on the coverglass dissuades from using higher concentrations, and suggests that the saturating levels are reached (**Figure 37B**). Clusters of nlgn1 labeled with dSA and anti-biotin antibody conjugated to Alexa647 contained on an average 2 visible objects, suggesting that the probes do not reach for more than 3 nlgn1 dimers, and/or are not all conjugated to alexa647. Finally, on the average, 7 streptavidins can be counted per cluster suggesting a clustering of the nlgn1 dimers by the tetravalent probe (**Figure 37D**), in accordance with the result obtained in FRAP experiment (**Figure 33**).

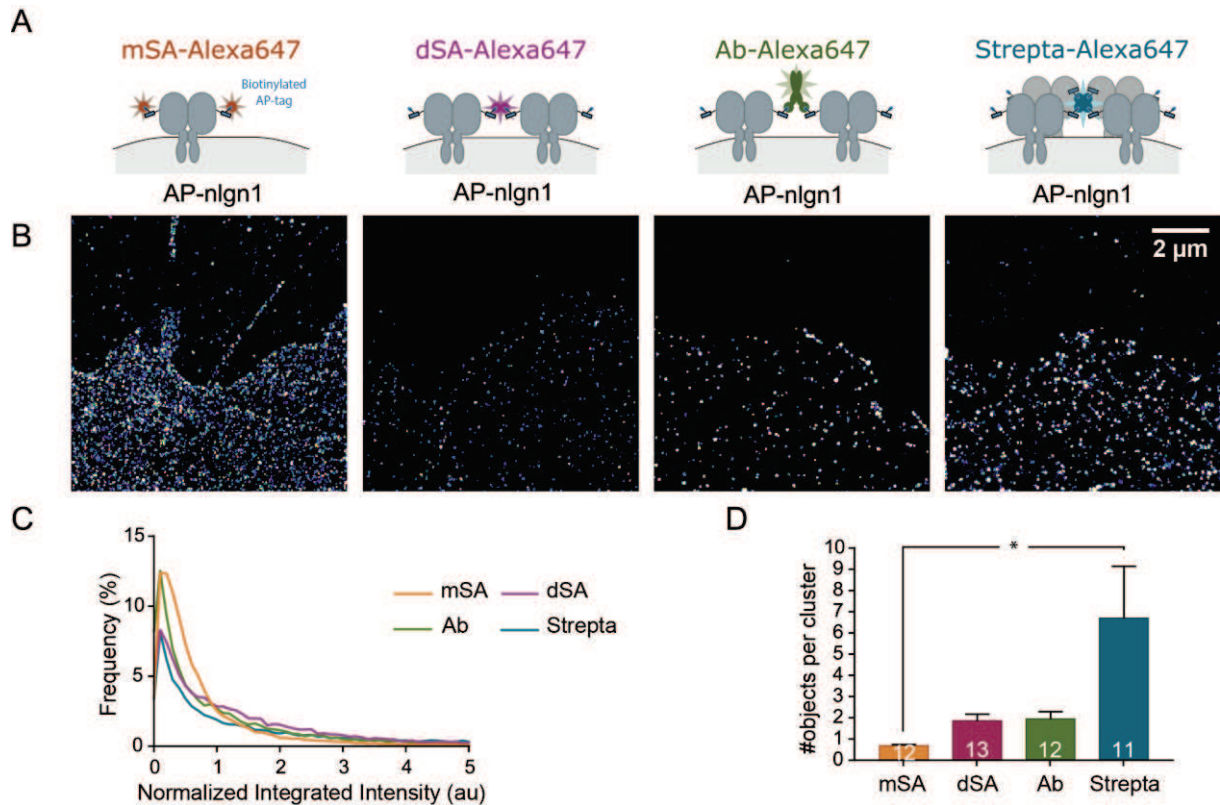


FIGURE 37: dSTORM OF AP-NLGN1 LABELED WITH mSA, dSA, ANTI-BIOTIN ANTIBODY, OR STREPTAVIDIN CONJUGATED TO ALEXA647.

(A) Schematic diagram of the AP-nlgn1 labeled with the four different probes conjugated to alexa647. (B) Typical dSTORM image reconstruction of AP-nlgn1 expressing cos-7 labeled with mSA-Alexa647, dSA-Alexa647, monoclonal anti-biotin antibody-Alexa647 (Ab), or streptavidin-Alexa647 (Strepta). (C) Frequency distribution of the normalized integrated intensity measured for the four different probes (mSA N=12; dSA N=13; Ab N=12; Strepta N=11 cells). (D) Bar graph of the number of objects per cluster measured for the four different probes. (Mean with SEM represented, one-way analysis of variance followed by Kruskal-Wallis test, * $p < 0.05$). Numbers in the bar charts represent the number of cells analyzed.

3.4.3. Effect of probe size and valence on the tetrameric AP-GluK2 nanoscopic organization

Photobleaching step counting of GluK2 subunit shows a preferred tetrameric conformation of the receptor, in agreement with its crystallized structure (Figure 25D). Saturating labeling of each subunit of the tetramer with a monovalent probe such as mSA-Alexa647 should lead to a 1:4 ratio, whereas labeling with dSA, anti-biotin and streptavidin can lead to even further protein clustering than with the dimer, by reaching out other tetramers (Figure 38A). However, the valence of the probe does not affect significantly the number of objects that can

be found in each cluster (**Figure 38C,D**). On average, 1 to 3 probes per cluster can be counted (**Figure 38D**), suggesting that, surprisingly, there is not much clustering induced by the dSA, anti-biotin nor streptavidin labeling, although the same labeling protocol had striking effects on the parameters measured by FRAP experiments.

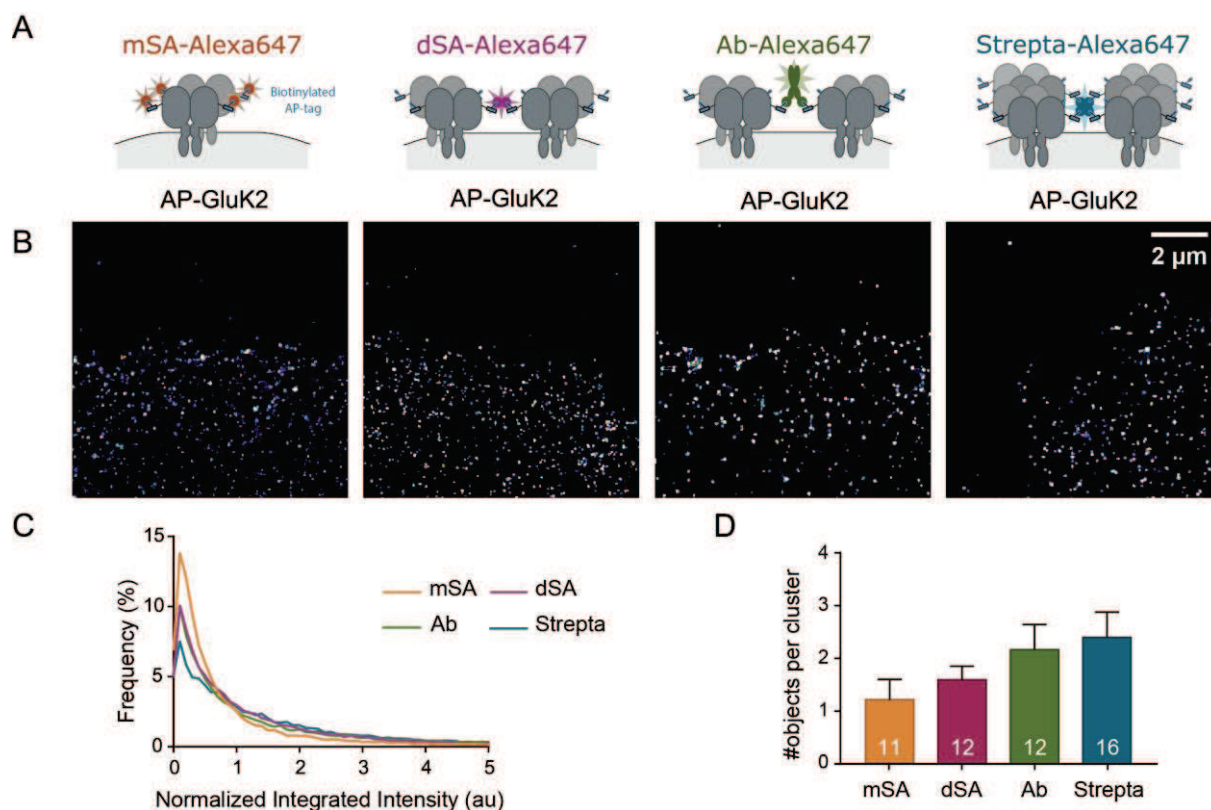


FIGURE 38: dSTORM OF AP-GLUK2 LABELED WITH mSA, dSA, ANTI-BIOTIN ANTIBODY, OR STREPTAVIDIN CONJUGATED TO ALEXA647.

(A) Schematic diagram of the AP-GluK2 labeled with the four different probes conjugated to alexa647. **(B)** Typical dSTORM image reconstruction of AP-GluK2 expressing cos-7 labeled with mSA-Alexa647, dSA-Alexa647, monoclonal anti-biotin antibody-Alexa647 (Ab), or streptavidin-Alexa647 (Strepta). **(C)** Frequency distribution of the normalized integrated intensity measured for the four different probes (mSA N=11; dSA N=12; Ab N=12; Strepta N=16). **(D)** Corresponding bar graph of the number of objects per cluster measured for the four different probes. (Mean with SEM represented, one-way analysis of variance followed by Kruskal-Wallis test, * $p < 0.05$; *** $p < 0.001$). Numbers in the bar charts represent the number of cells analyzed.

3.4.1. Effect of probe size and valence on the cluster size measured with dSTORM

Finally, no significant effect of the probe size and valence could be measured on the cluster size for the 4 different proteins (**Figure 39**). Indeed, the measured sizes on the dSTORM images correspond to the resolution of the setup, suggesting that the size of the objects is below the achievable resolution, and so are the possible changes.

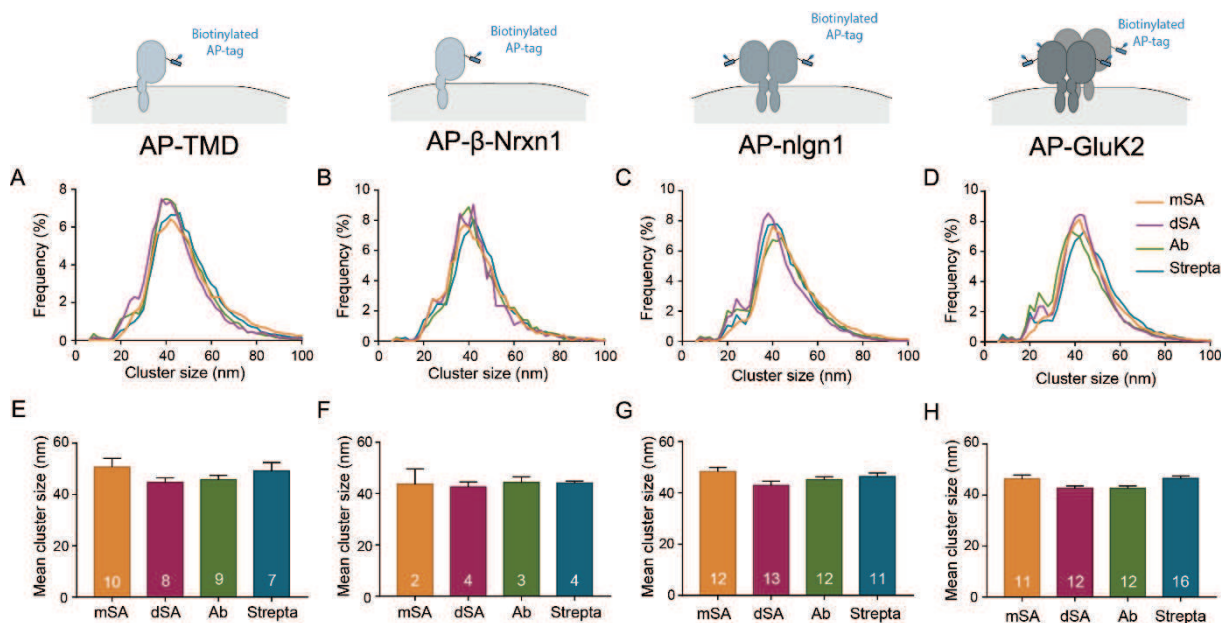


FIGURE 39: CLUSTER SIZE OF AP-TMD, AP-β-NRXN1, AP-NLGN1 AND AP-GLUK2, LABELED WITH MSA, DSA, ANTI-BIOTIN ANTIBODY, OR STREPTAVIDIN ON dSTORM POINTILLIST IMAGES.

(A-D) Frequency distribution of the cluster size of AP-TMD (A), AP-β-nrxn1 (B), AP-nlgn1 (C) and AP-GluK2 (D), measured for the four different probes. (E-H) Corresponding bar graph measured for the four different probes. (Mean with SEM represented, one-way analysis of variance followed by Kruskal-Wallis test, * $p < 0.05$; *** $p < 0.001$). Numbers in the bar charts represent the number of cells analyzed.

3.4.2. Effect of probe concentration and incubation time on the nanoscopic organisation of AP-GluK2

The difference in the diffusion coefficients measured by uPAINT and FRAP highlighted the importance of probe concentration on protein clustering. Instinctively, we understand that low concentration would not lead to protein clustering, since statistically, each probe would have more chance to reach only one protein than several proteins. However, totally saturating concentration would lead to a 1:1 ratio in the probe-protein binding, and therefore, would not lead to protein clustering as well. Conventional probe concentration were used for the experiment (around 1:100 as advised by provider recommendation). To ensure that this concentration was in the right range of clustering effect, I compared the number of objects and cluster size measured in the super-resolved reconstructed images of AP-GluK2 expressing COS-7 cells, labeled with 3 different concentrations of streptavidin-Alexa647: 5.8 nM, 58 nM and 580 nM, corresponding to the 0.1X, 1X and 10X of the regular labeling (**Figure 40A**). The concentration of the streptavidin-Alexa has no effect on cluster size (**Figure 40C,E**). Since the same probe with the same degree of fluorophore conjugation is used to compare the different concentrations, normalization is not necessary. Furthermore, differences in the concentration used can affect how isolated the probe is on the background and may lead to wrong normalization. For these reasons, cluster integrated intensities measured for the different concentrations on the dSTORM images were directly compared, showing that the concentration of streptavidin has no effect on the number of objects counted per cluster, suggesting low effect on protein clustering (**Figure 40B,D**).

Another parameter that can affect the level of protein aggregation caused by streptavidin labeling is the incubation time of the probe. Therefore, COS-7 expressing AP-GluK2 were labeled with streptavidin-Alexa647 with 3 different incubation times (10 min, 20 min and 40 min), and the integrated intensity distribution and size of the clusters on the dSTORM images were compared (**Figure 41A**). Although no significant difference can be sorted in the measured integrated intensity for the 3 incubation times, 40 min incubation tends to increase the number of detection in the clusters of the reconstructed images (**Figure 41B,D**). The cluster size on the pointillist image remains unchanged between the different incubation time (**Figure 41C,E**).

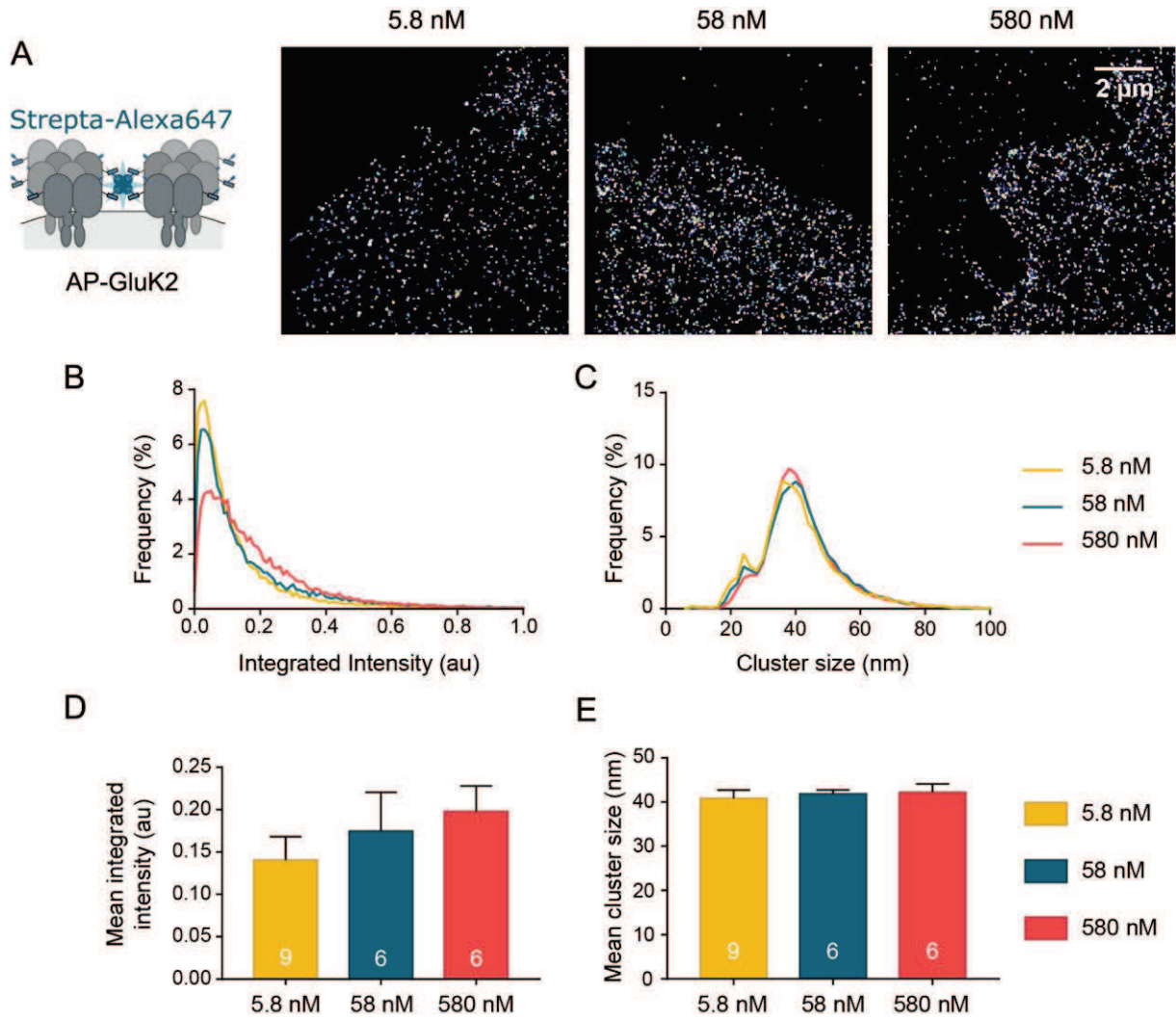


FIGURE 40: dSTORM OF AP-GLUK2 LABELED WITH 5.8 nM, 58 nM, OR 580 nM, OF STREPTAVIDIN CONJUGATED TO ALEXA647.

(A) (left) Schematic diagram of the AP-GluK2 labeled with streptavidin conjugated to alexa647, (right) typical dSTORM image reconstruction of AP-GluK2 expressing cos-7 labeled with 3 different concentrations (5.8 nM, 58 nM, or 580 nM) of streptavidin-Alexa647. **(B,C)** Frequency distribution of the integrated intensity **(B)**, and cluster size **(C)**, measured for the 3 different concentrations (5.8 nM N=9; 58 nM N=6; 580 nM N=6). **(D,E)** Bar graph of the mean integrated intensities **(D)** and cluster size **(E)** measured for the 3 different concentrations. (Mean with SEM represented). Numbers in the bar charts represent the number of cells analyzed.

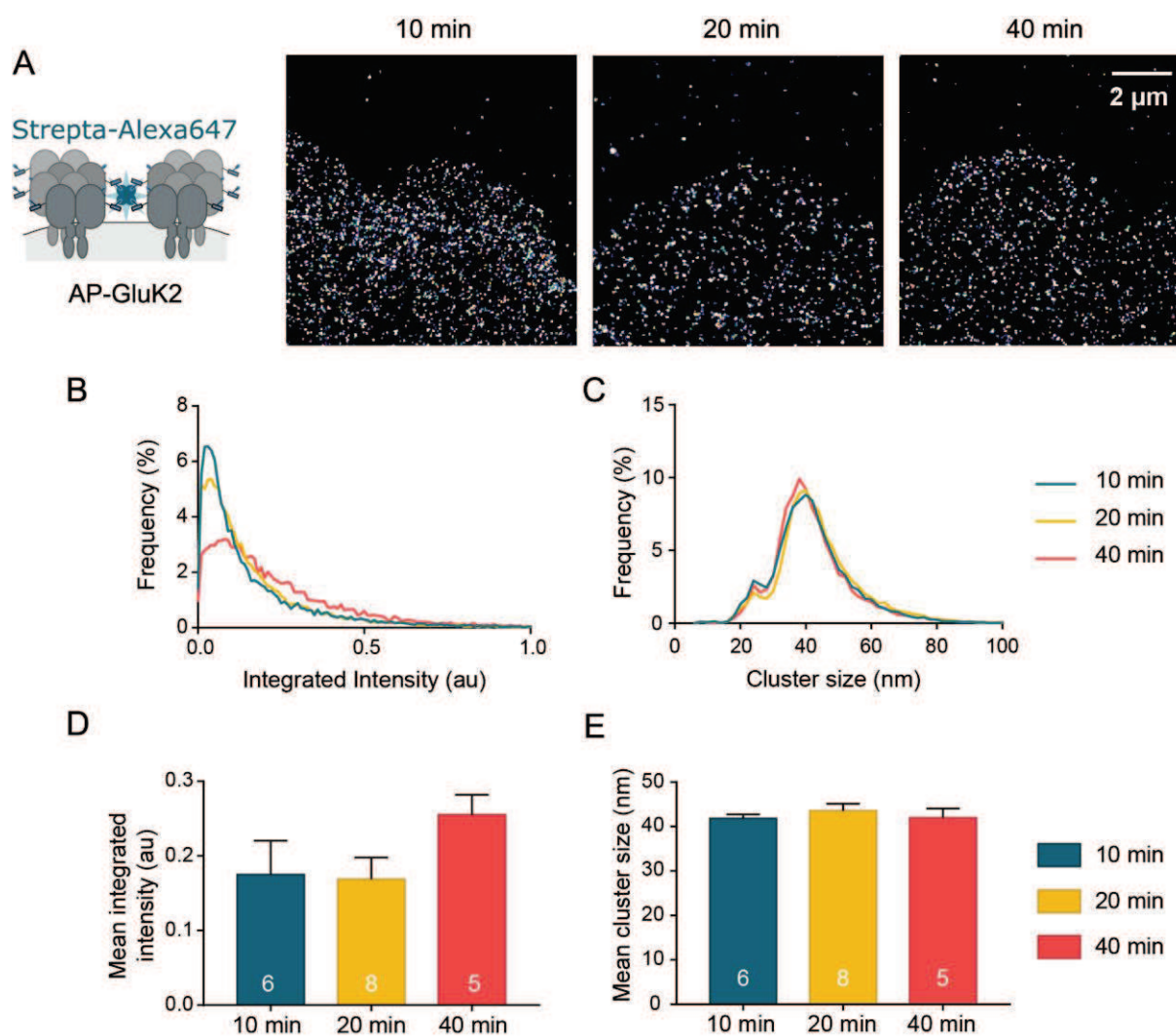


FIGURE 41: dSTORM OF AP-GLUK2 LABELED WITH STREPTAVIDIN CONJUGATED TO ALEXA647 FOR 10 MIN, 20 MIN, OR 40 MIN.

(A) (left) Schematic diagram of the AP-GluK2 labeled with streptavidin conjugated to alexa647, (right) typical dSTORM image reconstruction of AP-GluK2 expressing cos-7 labeled with streptavidin-Alexa647 (10 min, 20 min, 40 min) for 3 different incubation times. (B,C) Frequency distribution of the integrated intensity (B), and cluster size (C), measured for the 3 different incubation times (10 min N=6; 20 min N=8; 40 min N=5). (D,E) Bar graph of the mean integrated intensity (D) and cluster size (E) measured for the 3 different incubation times. (Mean with SEM represented). Numbers in the bar charts represent the number of cells analyzed.

3.5. Quantification of protein levels in neurons

To image β -nrxn1 at pre-synapses, primary rat hippocampal neurons were electroporated at the time of plating (DIV0) with AP- β -nrxn1, together with the endoplasmic reticulum-resident biotin ligase BirA^{ER} and Vglut1-mCherry pre-synaptic reporter. At DIV 14, neurons were labeled with mSA conjugated to Alexa647, and fixed for dSTORM experiment. An excellent colocalization of the mSA-Alexa647 with Vlut1-mCherry can be observed, indicating that mSA-labeled AP- β -nrxn1 efficiently reaches pre-synapses. Zooming on the pre-synapse, a sub population of AP- β -nrxn1 is condensed in nano-clusters with high protein density. Cluster analysis, using PalmTracer software, showed a cluster size laying in the range of 30 to 100 nm (mean 60 nm \pm SD 12.59 nm) and on an average 12 mSA-Alexa647 were counted per nano-clusters (**Figure 42**).

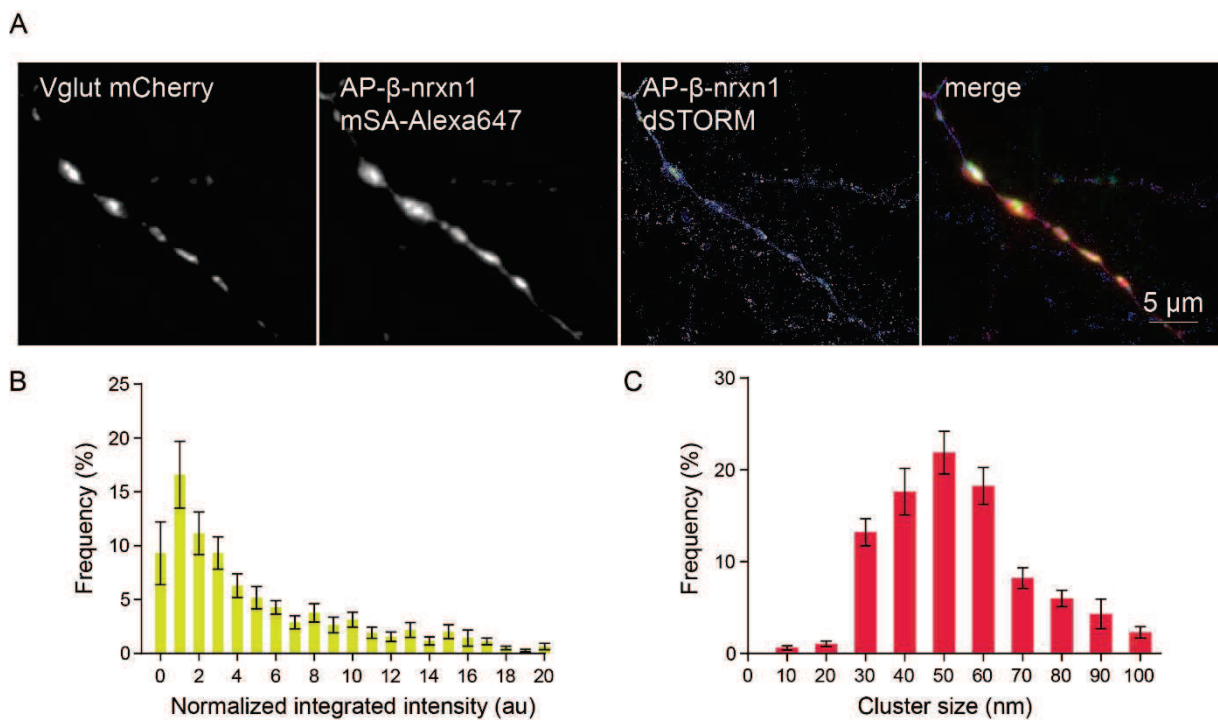


FIGURE 42: NANOSCALE ORGANIZATION OF AP- β -NRXN1 LABELED WITH MSA-ALEXA647 AT THE PRE-SYNAPSE USING dSTORM.

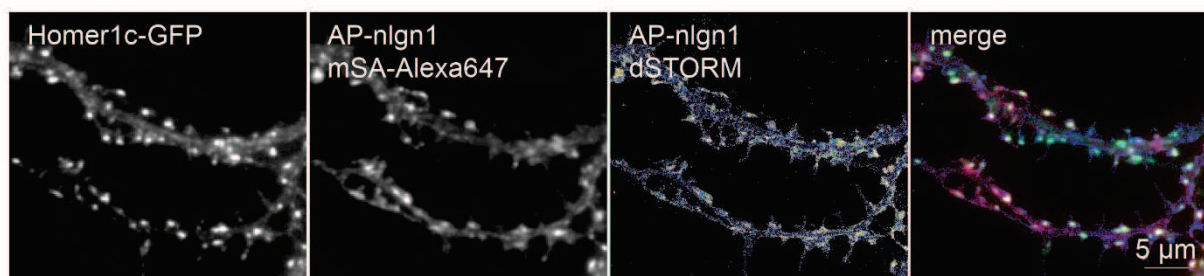
(A) DIV 14 neurons expressing the pre-synaptic marker Vglut1-mCherry, AP- β -nrxn1 and BirA^{ER} were labeled with 58 nM of mSA-Alexa647 and fixed for dSTORM.

(B) Frequency distribution of the normalized integrated intensity, (C) and cluster size measured at pre-synaptic puncta on the pointillist image. (N=13; Mean with SEM represented).

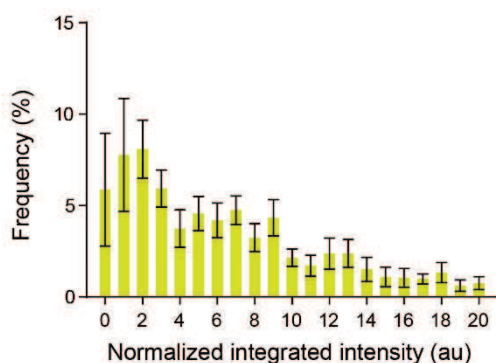
To assess the distribution of nlg1 and GluK2 at post-synapses, primary rat hippocampal neurons were electroporated at the time of plating (DIV0) with AP-nlg1 or AP-GluK2, together with the endoplasmic reticulum-resident biotin ligase BirA^{ER} and Homer1c-GFP as a post-synaptic reporter. At DIV 14, neurons were labeled with mSA conjugated to Alexa647, and fixed for dSTORM experiment.

AP-nlg1 and AP-GluK2 labeled with mSA-Alexa647 are found both in the shaft and in the spine, indicating that the labeled proteins efficiently reach pre-synapses. Zooming on the pre-synapse, sub populations condensed in nano-clusters with high protein density can be found. The cluster size measured *via* PalmTracer software, also lays in the range of 30 to 100 nm for the two post-synaptic proteins with bigger clusters for the AP-nlg1 (mean cluster size 86 nm \pm SD 31 nm for AP-nlg1; vs 57 nm \pm SD 11 nm). Interestingly, the size of AP-nlg1 nano-clusters correlates with the size of PSD scaffold molecules domains measured by PALM (Nair et al., 2013). Nano-cluster of AP-nlg1 and AP-GluK2 are enriched with an average of 25 *versus* 8 mSA-Alexa647, respectively (**Figure 43, Figure 44**).

A



B



C

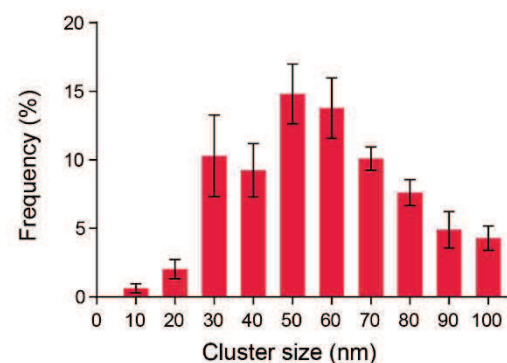
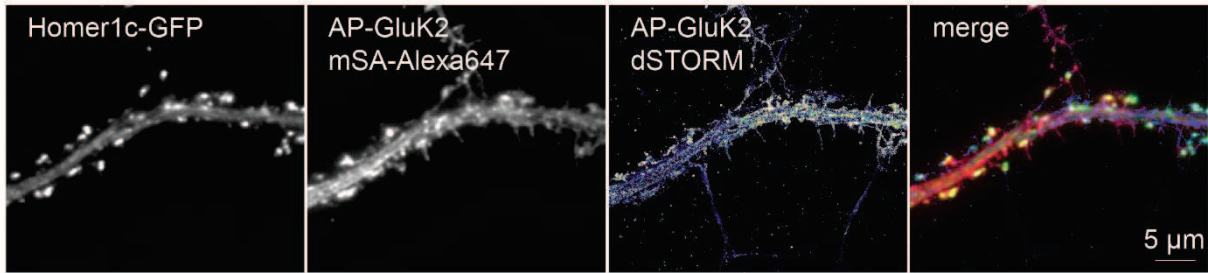


FIGURE 43: NANOSCALE ORGANIZATION OF AP-NLGN1 LABELED WITH mSA-ALEXA647 AT THE POST-SYNAPSE USING dSTORM.

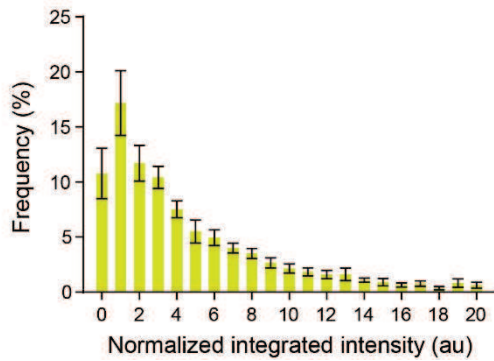
(A) DIV 14 neurons expressing the post-synaptic marker Homer1c-GFP, AP-nlg1 and BirA^{ER} were labeled with 58 nM mSA-Alexa647 and fixed for dSTORM.

(B) Frequency distribution of the normalized integrated intensity, (C) and cluster size measured at post-synaptic puncta on the pointillist image. (N=9; Mean with SEM represented).

A



B



C

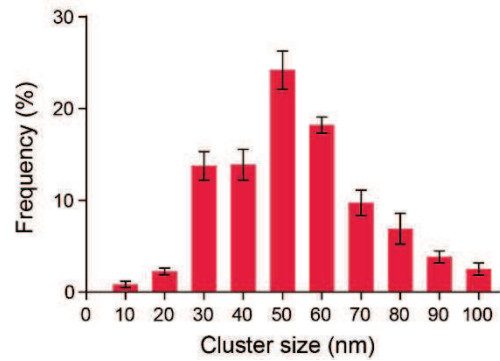


FIGURE 44: NANOSCALE ORGANIZATION OF AP-GLUK2 LABELED WITH MSA-ALEXA647 AT THE POST-SYNAPSE USING dSTORM.

(A) DIV 14 neurons expressing the post-synaptic marker Homer1c-GFP, AP-GluK2 and BirA^{ER} were labeled with 58 nM mSA-Alexa647 and fixed for dSTORM.

(B) Frequency distribution of the normalized integrated intensity, (C) and cluster size measured at post-synaptic puncta on the pointillist image. (N=12; Mean with SEM represented).

– CHAPTER 4 –
Discussion

Critical cellular functions including synaptic transmission occur at dynamic macromolecular platforms of the cell membrane, where protein concentration is extremely high and lies in a very confined and compartmentalized space. Recent development in fluorescence microscopy allows the mapping of single molecules with a 20-50 nm resolution. To accompany such progress, there is a pressing need for efficient labeling strategies relying on small penetrating probes with minimum linkage error with respect to target proteins. While antibodies have the strong advantage to be able to target endogenous proteins, their large size and divalence might affect protein aggregation level and diffusion behaviors. For now, very few studies have thoroughly compared the effect of probe size and valence in super-resolution imaging. Recently in the team, a comparison of monomeric (mSA), dimeric (antibody) and tetrameric (streptavidin) labeling of nlgn1 in dissociated neurons suggested that probe multivalence affects the measurements by generating artificial nanoscale clusters and biasing protein diffusion (Chamma et al., 2016).

In this thesis, I proposed a comparative study of probe valence and size impact on the diffusion and aggregation of proteins with different stoichiometry, with regard to the microscopy technique used. Proteins of 3 different conformations: **monomeric** (AP-TMD and AP- β -nrxn1), **dimeric** and **tetrameric**, were labeled with probes of different size and valence. While the anti-biotin antibody is a large divalent probe, mSA, dSA and streptavidin are small **monovalent**, **divalent** and **tetravalent** probes respectively. Effect of probe size and valence on protein diffusion was assessed with two complementary techniques relying on **low concentration** for the **uPAINT** and **high concentration** of the probe for the **FRAP**. **dSTORM** was used to investigate the effect on protein organization and aggregation. In order to assess the effect of the probe valence, the concentrations of the probes were kept identical, to have the same number of mSA, dSA, anti-biotin and streptavidin. Nevertheless, it could have been interesting to maintain the same concentration in terms of binding domains ([Figure 45](#)).

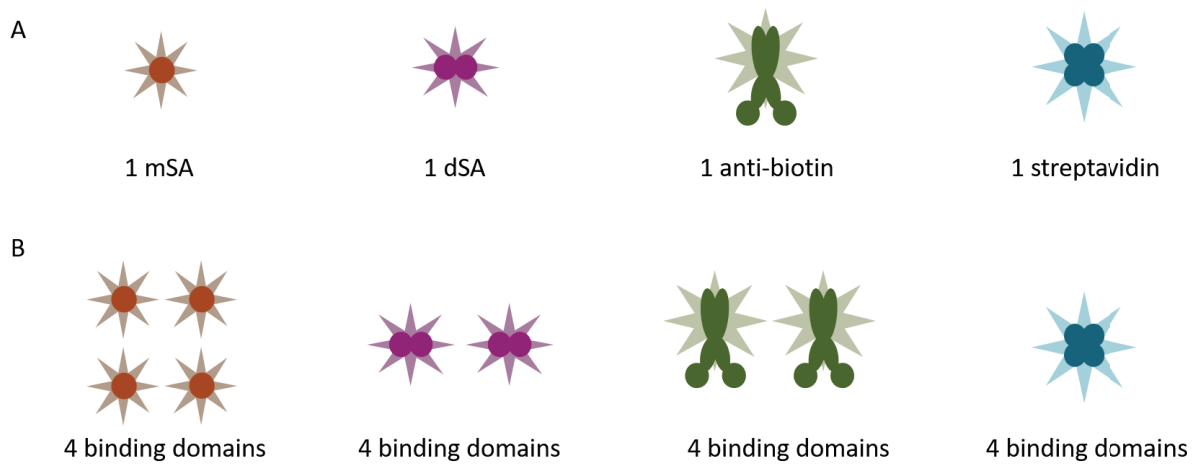


FIGURE 45: ALTERNATIVE LABELING STRATEGIES.

(A) Labeling strategy where the concentrations of the probes are identical.

(B) Labeling strategy where the number of binding domains is used to set the concentration, in this case mSA, dSA, anti-biotin antibody, and streptavidin concentration are 4X, 2X, 2X, and 1X respectively.

4.1. Receptor stoichiometry

Although receptor stoichiometry has been well established and described in previous work for β -nrxn1, nlg1 and GluK2, in order to ensure the effect of labeling, I determined the distribution of receptor subunit by counting irreversible photobleaching steps of GFP-labeled constructs at hundreds of individual receptors immobilized on a passivated surface. Our analysis of GFP- β -nrxn1 single photobleaching steps was consistent with the expectation that β -nrxn1 forms monomers at the cell surface. Also, consistent with earlier work, GluK2-GFP forms tetramers and nlg1-GFP forms dimers (Dean et al., 2003; Sobolevsky, 2015). However, a small fraction of nlg1-GFP exhibits a single photobleaching step, suggesting that some of the proteins remain in a monomeric form. In this single molecule pull down experiment, immobilization of proteins on the passivated substrate is conducted by lysing cells, although proteins are supposed to keep their conformation since they remain in a small fragment of plasma membrane, the lysis might cause a disassembly of nlg1 dimers, biasing the real fraction of monomers present at the cell surface. Previous work on nlg1 showed that the dimerization of nlg1 is required for its synaptogenic function, however, pull down assays also show a fraction of nlg1 monomers, in accordance with the results found with photobleaching step counting (Dean et al., 2003), suggesting that the nlg1 is not exclusively forming dimers, or that detergent used both for photobleaching step counting and pull down assays, may alter the dimeric structure of the neuroligin1. As Fluorescence Resonance Energy Transfer (FRET)

can occur even between 2 GFP molecules, one functioning as a donor and the other one as an acceptor, homo-FRET may be responsible for the decrease in the photobleaching step counting for the neuroligin1 dimer, especially considering the close proximity of the GFP on each C-tail of the protein construct (Gautier et al., 2001).

On the other hand, GFP subunit counting of a nlgn1 mutant that contains two point mutations (E584A/L585A) designed to impair dimer formation showed that the single photobleaching step distribution of this mutant does not follow the description by the binomial distribution for a monomer, although it exhibits more single photobleaching steps than the nlgn1 wild type, suggesting that this mutant is still capable of forming a small fraction of dimers (**Figure 25E**). This result also complies with pull down assays from a previous study (Dean et al., 2003).

Steps counting become challenging when reaching 4 steps, as for the kainite receptor complex, and alternative detergents may be considered to improve the signal to noise ratio. For instance, the use of n-Dodecyl β -D-maltoside seems to help improving the photobleaching step counting.

4.2. Probe size and valence affects protein diffusion when high labeling concentration are used but not with low concentration

To assess the effect of probe size and valence on protein diffusion, I used two powerful and complementary techniques: uPAINT and FRAP. While uPAINT allows for access, heterogeneous movements at the molecule level with high statistics, FRAP has the strong advantage to access long dwell times. One technique cannot replace the other and should be chosen very consciously depending on the type of information searched and the time window considered. Yet, because of their opposed experimental design, sparse labeling to achieve single molecule detection for the uPAINT *versus* near-saturating labeling for the ensemble FRAP method, we can safely hypothesize that probe size and valence may have distinct effects regarding those two techniques.

4.2.1. Effects of probe size and valence on protein diffusion assessed by uPAINT

First, I investigated the effect of the differential labeling on the diffusion of surface diffusing AP- β -nrxn1, AP-nlgn1 or AP-GluK2 expressed in COS-7 cells using uPAINT experiments. A previous study in the team found that, in DIV7 neurons, AP-nlgn1 labeled with multivalent

probes (anti-biotin antibody or streptavidin) exhibit diffusion coefficients shifted towards lower values and a concomitant increase in the fraction of slowly diffusing molecules ($D < 0.01 \mu\text{m}^2/\text{s}$) (Chamma et al., 2016). This result suggests that divalent and tetravalent probes alter AP-nlgn1 distribution and dynamics through a combination of protein cross-linking and steric hindrance. Surprisingly, when expressed in COS-7 cells, I found that AP-nlgn1 and AP-GluK2 diffusion remained unchanged, no matter the valence or the size of the probe used to label the protein (Figure 27, Figure 28). Several biological limitations are to be taken into account when addressing synaptic protein mobility (Delgado and Selvin, 2018). Indeed, the PSD is a very crowded environment with a high density of surface expressed proteins, coupled with an abundance of scaffolding proteins, as seen in freeze-fracture electron microscopy images (Budisantoso et al., 2012; Choquet and Triller, 2013; Fukazawa and Shigemoto, 2012; Holderith et al., 2012; Shinohara and Hirase, 2009; Tarusawa et al., 2009). For instance, the intracellular scaffolding proteins can slow down the diffusion in two ways: by interacting, directly or indirectly, with the protein of interest (Bats et al., 2007), and by creating barriers to free diffusion (Choquet & Triller, 2013; Li et al., 2016; Li & Blanpied, 2016). For those reasons, protein crosslinking might lead to severe decrease in protein diffusion inside synapses, bringing a large number of associated proteins, with the protein of interest. On top of this crosslinking effect, the steric hindrance of large probes can impair the penetration of the labeled protein to the synaptic cleft (Chamma et al., 2016; Howarth & Ting, 2008; Lee et al., 2017), and even when probes manage to reach proteins there, their diffusion would be largely limited by the narrowness of the synaptic cleft ($\sim 20 \text{ nm}$ thick). These differences in the membrane composition and properties between dissociated neurons and COS-7 cells might explain why the effects of probe valence and size on receptor diffusion, as measured with uPAINT, are more striking when assessed in neuronal cultures than in heterologous cells.

On the other hand, the impact of anti-biotin antibody labeling on AP- β -nrxn1 diffusion surprisingly differs largely from the two other proteins. Indeed, the measured diffusion coefficient of AP- β -nrxn1 expressed in COS-7 cells is shifted toward lower values when the protein is labeled with anti-biotin antibody compared to the tracking with mSA or streptavidin, and a concomitant increase in the percentage of slowly diffusing proteins (defined as $D < 0.01 \mu\text{m}^2\text{s}^{-1}$) can be noticed. Although there is no difference in the diffusion coefficient, labeling with mSA leads to a small yet statistically significant increase in the percentage of slowly

diffusing AP- β -nrxn1 compared to streptavidin labeling. Unspecific binding due to lower biotin affinity of mSA *versus* streptavidin contaminating the diffusion coefficient cannot be ruled out, however, mSA labeling leads to this type of behavior only for AP- β -nrxn1, and this result is consistent with the FRAP results (Figure 31). Another hypothesis is that labeling with streptavidin, but not with the small mSA leads to the shielding of a non-specific binding site on the AP- β -nrxn1, thereby lowering its interaction with the substrate or coverglass. This hypothesis would also explain the striking effect of anti-biotin antibody labeling observed on the diffusion coefficient and immobile fraction, as even a small interaction of the protein with the substrate would complicate the binding and diffusion of such a large probe. One critical experiment to verify those hypotheses would be to insert a photo-activatable or photo-convertible protein into the construct in order to simultaneously track and compare unlabeled and labeled proteins.

Overall, several limitations are to be taken into account regarding the uPAINT results. First, multiple labeling can occur on the dimeric and tetrameric proteins, which would lead to multiple tracking of the same protein. Although this fact may seem of little importance regarding the tracking of the protein, since all proteins should be similarly over-labeled, it is important to consider that immobile proteins are easier to track, due to the decrease of missed-reconnections, and therefore longer trajectories, together with the over-labeling of the proteins, a potential mis-calculation of the proportion of immobile/mobile protein may occur. Another important point to discuss is the possibility to have a biased measurement due to the region of interest: indeed, to limit the auto-fluorescence coming from cellular structures and therefore increase the signal to noise ratio, proteins are tracked at the periphery of the cell, yet the molecular composition of the cell membrane, which may differ from the center to the periphery of the cell, is critical in the behavior of diffusive proteins.

One critical parameter in the diffusion measurement to also be taken into account is the incubation time, as minimal time may be required for multivalent probes to reach other proteins. Yet, recordings at the beginning of the experiments and at the end on the same coverslip show similar diffusion properties (~45 min delay between the first and the last recording) (Figure 29).

Overall, the modest effect of probe valence on receptor diffusion, that was contrary to our initial expectation, led me to hypothesize that the ligand concentration used to perform

uPAINT experiments was not high enough to induce significant cross-linking of the receptors. Thus, I focused on the receptor of highest valence, AP-GluK2, and tracked its diffusion properties by uPAINT using a small amount of Atto-647-conjugated streptavidin, while inducing cross-linking with a large concentration of unlabeled streptavidin. Under those conditions, I found that clustering with saturating concentration of neutravidin leads to a decrease in the diffusion of AP-GluK2. Altogether, these results suggest that although the probe valence and size do not seem to affect the diffusion of surface diffusing membrane proteins measured by uPAINT experiments, it can affect the behavior observed by techniques relying on saturating labeling concentration.

4.2.2. Effect of probe size and valence on protein diffusion assessed by FRAP

Although FRAP can be performed on recombinant proteins tagged with a fluorescent protein such as GFP or RFP, some studies prefer to assess the diffusion of endogenous proteins with conjugated antibodies. In this case, proteins of interest are labelled using a saturating concentration of specific conjugated antibodies, which can lead to protein clustering, therefore biasing the conclusion on measured diffusion parameters.

Surprisingly, the immobile fraction of AP- β -nrxn1 labeled with mSA-Atto594 was much higher than with streptavidin-Atto594, and nothing comparable to the immobile fraction of AP-nlgn1 and AP-GluK2 labeled with mSA, which exhibit lower immobile fraction than when labeled with streptavidin, suggesting the mSA labeling is not responsible for protein immobilization (Figure 31A,B,F). On the other hand, GFP- β -nrxn1 seems to have a higher diffusion coefficient (to be confirmed with larger samples) than its AP-tagged version labelled with mSA-Atto594 (Figure 32B,C). Interestingly, GFP- β -nrxn1 lacks 4 amino acids from the original sequence of β -nrxn1 (GLAN located at 1088 amino acids from the N-terminus), and we hypothesized that the presence of this stretch of amino-acids is linked to the slowing down of AP- β -nrxn1, e.g. by promoting some non-specific interaction with an immobile protein or the substrate. When labeled with streptavidin-Atto594, AP- β -nrxn1 diffusion measured by FRAP is slowed down (Figure 32B,C), but the immobile fraction is restored to levels comparable to the GFP- β -nrxn1 (Figure 32B,D). This result suggests that the clustering induced by streptavidin labeling masked the potential unspecific binding sequence of the β -nrxn1 to the substrate.

The puzzling result of AP- β -nrxn1 diffusion in COS-7 cells measured by FRAP led us reconsider the use of this protein to assess the effect of probe size and valence on monomeric protein diffusion and aggregation, therefore, from this step, AP-TMD was added to the experimental design.

FRAP experiments on COS-7 expressing AP-TMD, AP-neurologin1 or AP-GluK2 labeled with saturating concentrations of either Atto594 conjugated mSA, dSA, divalent anti-biotin antibody, or streptavidin, showed that even if probe size and valence do not affect protein diffusion when low concentrations are used (uPAINT), saturating concentrations lead to major cross-linking of the proteins (**Figure 33**). Indeed, drastic reductions of the diffusion coefficient (**Figure 33E**), as well as increased immobile fractions (**Figure 33F**), can be measured when multivalent probes are used, although simple doubling of the protein transmembrane complex size does not significantly affect their diffusion, as similar diffusion coefficients can be measured for AP-TMD labeled with mSA, dSA or AP-nlgn1 labeled with mSA (**Figure 33E**).

More specifically, labeling with antibody strongly affects the diffusion of monomeric, dimeric and tetrameric receptors, an effect which is probably due to a combination of the fairly large size of the probe and its divalence. According to different mathematical models for Brownian movement of transmembrane molecules inside a biological membrane, the transversal size of the transmembrane cylinder directly affects the diffusion of the object, independently from the extracellular segment longitudinal size (Hughes et al., 1981; Petrov and Schwille, 2008; Saffman and Delbrück, 1975; Saffman and Saffman, 2006). Those models suggest that the valence of the probe, that multiply the surface of the transmembrane segment, would have a greater impact than the probe size on the diffusion of the targeted proteins. Yet, the size of antibodies affects the distance of the two binding domains on the probe, which might be of consequence on the total surface of the transmembrane cylinder. Moreover, those models applied on extracellular compartments with an estimated viscosity that does not take into account the topology of the environment, for instance, a narrow synaptic cleft embedded with multiple proteins having large extracellular domains would affect the diffusivity of proteins with large ectodomains.

Interestingly, the antibody effect on the diffusion of the AP-TMD is much more pronounced than the one of dSA (**Figure 33E**), and streptavidin labeling leads to a general decrease in the measured diffusion coefficient of membrane proteins, that intensifies when the number of

binding sites augments on the targeted protein (Figure 33E). On the other hand, dSA labeling leads to a twofold decrease in the diffusion coefficient of AP-nlgn1 compared to mSA, but does not impact AP-GluK2 diffusion, AP-sites on GluK2 being probably close enough to be bound by the same dSA (Figure 33E). Surprisingly, the immobile fraction of the AP-TMD labeled with the antibody is extremely high (Figure 33E), up to 6-fold the one of AP-TMD labeled with dSA. Interestingly, AP-TMD labeled by anti-biotin antibody conjugated with Atto594 or Alexa647 in FRAP and dSTORM experiments respectively, seem to follow specific cellular structures, with an accumulation at the tip of the lamellipodium (Figure 34A, Figure 35B). AP-TMD is composed of the transmembrane domain of the platelet-derived growth factor receptor, which is a member of the tyrosine kinase receptor family. This fact is interesting considering that upon activation, dimers of receptors are playing a role in actin cytoskeleton rearrangement (Heldin and Westermark, 1995; Nagano et al., 2006). Artificial dimerization caused by antibody binding may be responsible for the stereotypical localization of the AP-TMD in this condition, however, it remains unclear what mechanisms are at stake, considering that only the transmembrane sequence is conserved, and not the tyrosine kinase domain.

The fact that AP-TMD labeled with streptavidin-Atto594 and AP-GluK2 labeled with mSA-Atto594 display similar diffusion coefficients, suggests that the concentration used achieves the best clustering scenario, with one streptavidin binding 4 AP-TMD molecules (Figure 33E), and higher concentration of probe would probably lead to a one-to-one labeling.

Overall, these results suggest that, while low concentration labeling used for uPAINT relies on probe specificity, techniques using saturating concentration of probes should consider probe size and valence, especially when targeting multiple sites on the protein of interest (e.g. polyclonal antibodies, or monoclonal antibodies targeting a multimeric protein).

Finally, labeling with mSA leads to highest diffusion coefficient and least protein immobilization, consistent with its small size and monovalence (Figure 33E,F).

4.3. Probe size and valence impact the aggregation of membrane proteins

The evolution of fluorescence microscopy with the development of super-resolution techniques instigates a strong will to assess synapse composition, protein absolute number and organization, with the hope to reach a better understanding of synapse specificity and function, and more globally, cellular function.

The two main super-resolution techniques available to investigate protein organization and absolute quantification are the PALM and dSTORM, each one of them with their own advantages and drawbacks. While PALM uses irreversible PA probes making the pointillist image easier to translate to absolute number of proteins, dSTORM has the salient advantage to be able to target endogenous protein, *via* the use of conjugated antibodies (Durisic et al., 2014b). However, although those probes remain widely used to study protein organization, recent studies highlighted the impact of such large and multivalent probes on protein behavior (Chamma et al., 2016; Delgado & Selvin, 2018; Howarth & Ting, 2008; S. H. Lee et al., 2017). The fact that the probe size and valence affect protein diffusion suggests that it would also impact protein localization and organization, yet no thorough study has been performed to discriminate the effects of size and valence. Having a better understanding on such parameters is critical to develop better probes, especially in packed and compartmentalized environments such as synapses. From this standpoint, I characterized the effect of probe size and valence on the organization of 4 membrane proteins of different stoichiometry in a neutral environment. The **monomeric** AP-TMD and AP- β -nrxn1, **dimeric** AP-neurologin1 or **tetrameric** AP-GluK2 were expressed in COS-7 cells, and labeled with **monovalent** streptavidin (mSA), **divalent** streptavidin (dSA), **divalent** anti-biotin antibody, or **tetravalent** streptavidin, all conjugated to alexa647, and dSTORM experiments were performed. The main difficulty consists in finding a reliable approach allowing the conversion of cluster of detections in the dSTORM images into molecule numbers. Here, I will briefly present the counting approach I used, then I will discuss the results and their relevance to the understanding of labeling consequences on protein organization. Finally, I will detail some of the limitations that complicate the analysis of quantitative dSTORM-based datasets.

4.3.1. The analytical approach

The correct analysis of SMLM datasets relies on the accuracy to assign groups of detections in the pointillist image to a given molecule (Annibale et al., 2011; Durisic et al., 2014b; Fricke et al., 2015; Patrizio and Specht, 2016), which is largely dependent on the photophysical properties of fluorophores. Several parameters are to be taken into account to avoid over- and under-counting of the proteins. Indeed, the number of detections constituting the super-resolved image is not equal to the number of fluorescent molecules present. For instance, the stochastic fluctuations in the number of emitted photons combined with the fact that fluorophores are usually active for several consecutive frames, are responsible for each fluorophore being in fact represented by a small cluster of points in the pointillist image. The dSTORM experiment relying on reversibly photoswitchable probes that can be switched on and off hundreds of times before being permanently photobleached, makes the translation from bursts of detection to absolute number of molecules even more challenging. Adding a supplemental layer of complexity, the use of polyclonal antibodies can lead to over-labeling, and thus over-counting, while monoclonal divalent antibodies might lead to under-counting through artificial clustering, or under-labeling due to steric hindrance that makes the target out of reach. However, the main advantage of the dSTORM technique is to be able to target endogenous proteins, unraveling a real need for a better characterization of probe size and valence on protein aggregation.

Recurrent fluorophore detections can be corrected from their temporal and/or spatial distribution, based on the behavior of single fluorophores (Annibale et al., 2011; Durisic, Cuervo, & Lakadamyali, 2014; Fricke et al., 2015). In this study, I chose to correct for multiple detections through a normalization by the intensity pattern of single fluorophores immobilized on the background.

On the other hand, high density of fluorophore detection can be responsible for under-counting of proteins, as two different proteins may be mistaken for one. To ensure proper single-molecule density during the acquisition, single-molecule localization and reconstruction were performed online with automatic feedback control of the lasers using the WaveTracer module, generously provided by the group of JB Sibarita.

4.3.2. Aggregation levels

AP-TMD allows the binding of one probe at a time (**Figure 35A**): indeed an average number of 1 mSA per molecule can be counted on the dSTORM super-resolved images (**Figure 35E,F**), surprisingly, around 8 streptavidins and 7 anti-biotin antibodies are found per cluster, suggesting a clustering of the TMD (**Figure 35E**) up to 32 and 14 for the streptavidin and the antibody, respectively. It remains unclear why the protein would cluster when labeled with anti-biotin antibody and streptavidin but not with mSA (**Figure 35E**), although artificial clustering of AP-TMD may be responsible for a delocalization close to the actin filament, in relation with the PDGFR cellular function. A potential clustering with mSA should be ruled out since TMD displays a fast diffusion coefficient and a low immobile fraction measured by FRAP (**Figure 33B,E,F**).

AP- β -nrxn1 also possesses one AP-TAG and should allow the binding of only one probe at a time, yet aggregation of the protein may also be observed independently from the probe valence, characterized by a very sparse distribution of the normalized integrated intensity for the different probes (**Figure 36C**). Although the aggregation is surprising, this result is consistent with the partial (20-30%) immobilization observed with FRAP (**Figure 31B,F**).

On the other hand, AP-nlgn1 labeling with mSA-Alexa647 should lead to a 1:2 ratio given the dimeric nature of nlgn1, or at least to a distribution resembling the one observed with photobleaching step counting, whereas labeling with dSA, anti-biotin and streptavidin should lead to further protein clustering by reaching out other nlgn1 dimers (**Figure 37A**). However, only one mSA per cluster of nlgn1 could be counted, suggesting that some of the mSA is not conjugated to Alexa647, the labeling is not saturating the biotinylated AP sites, or not all the AP-tags are biotinylated (**Figure 37E**). Higher concentrations of mSA-Alexa647 can be used to test this hypothesis, although mSA-Alexa647 already exhibits high non-specific binding on the coverglass at this concentration. The distribution of counts can be fitted with the binomial distribution obtained with photobleaching step counting, the probability of detection would then represent the degree of conjugation of the probe as well as the labeling of the protein (comprising biotinylation as well as probe binding), however, this would not serve to translate to other protein labeling, even with the same probe, since the biotinylation may still differ. While 7 streptavidins can be counted per nlgn1 cluster, highlighting the clustering by the tetravalent probe (**Figure 37E**), on average 2 visible objects can be counted in nlgn1 clusters

labeled with dSA and anti-biotin antibody conjugated to Alexa647, suggesting that those probes do not reach for more than 3 nlg1 dimers, and/or are not all conjugated to alexa647. The GluK2 subunit forming a tetramer, saturating labeling with a monovalent probe such as mSA-Alexa647 should lead to a 1:4 ratio, whereas labeling with dSA, anti-biotin and streptavidin should lead to even further protein clustering by reaching out other tetramers (**Figure 38A**). Surprisingly, there is not much clustering induced by the dSA, anti-biotin nor streptavidin labeling, as on average, 1 to 3 probes per cluster are counted (**Figure 38E**). In contrast, the same labeling protocol had striking effects on the parameters measured by FRAP experiments. However, it is important to keep in mind that even when only one streptavidin molecule is counted, 4 GluK2 subunits can potentially be attached to the same streptavidin tetramer, and although those proteins would not be counted, the diffusion of the complex would still be affected. Because of its tetrameric conformation, AP-GluK2 possesses twice as many binding sites for the different probes, compared to AP-nlg1. This particularity would make the level of aggregation by the multivalent probes even more striking than for a dimeric protein. However, it seems that there is no change in the number of anti-biotin antibody and dSA that can be counted in AP-nlg1 *versus* AP-GluK2 clusters, and fewer streptavidin are found in AP-GluK2 than in AP-nlg1 clusters. The conformation of the GluK2 tetramers makes the 2 AP tags present on the same side very close to each other, and this proximity may allow a single multivalent probe to bind 2 tags on the same protein. Moreover, this can lead to steric hindrance once a probe is bound, which would explain the puzzling results found. Another possibility is that only a fraction of the AP-GluK2 is actually labeled, as only one mSA-Alexa647 is counted per cluster of AP-GluK2. The underlabeling can be due to non-saturating concentration, or to an incomplete biotinylation of the AP-tags. This suggests that 3 out of 4 AP-GluK2 are detectable, and the aggregation levels might in reality be up to 4 times higher than the measurement for the multivalent probes.

It should be noted that a range of different probe concentrations (0.1X, 1X and 10X) were compared to assess probe size and valence effect on protein aggregation, showing little to no effect on protein clustering, while increasing the incubation time tended to enhance protein aggregation. However live labeling is usually restricted to a short incubation time, which makes the 10 min labeling more relevant for this study.

No difference was measured in the size of the clusters throughout this probe testing, with a mean cluster size of around 40 nm. However, this size correlates with the localization precision in X,Y of the system used (measured on isolated fluorophores on the background), suggesting that clusters may actually be smaller than the system resolution allows us to determine.

4.3.3. Main analytical limitations

We estimated that over-counting caused by multiple fluorophores per probe and multiple cycles of activation was corrected through the normalization by the intensity pattern of single fluorophores immobilized on the background. Nevertheless, several complications caused by undercounting may limit the interpretation of the results.

An important parameter for the correct interpretation of quantitative dSTORM datasets, is the probability to visualize the labeled proteins, under the chosen imaging conditions. In general, when doing PALM, the probability of detection of fluorescent molecules depends on their correct folding, as well as the potential bleaching prior to photoconversion. In dSTORM, the probability of detection also relies on the labeling efficacy. For instance, the use of antibodies can lead to important misinterpretation of the results, due to the accessibility of the protein epitope or the quality of the antibody used. During my PhD, I chose to use AP-tagged proteins in order to have a direct comparison of the effect of probe size and valence in the exact same experimental conditions, namely: same protein expression levels in the same cell type, with the same part of the protein targeted, etc. However, this choice added several supplemental layers of complexity, when it comes to absolute protein number. Indeed, this labeling relies on multiple steps. First the protein has to be biotinylated in the ER, then, once it is addressed to the cell surface, it has to be labeled by the probe, and the probe itself needs to be conjugated to a fluorophore, and should not be photobleached prior to the beginning of the acquisition ([Figure 46](#)).

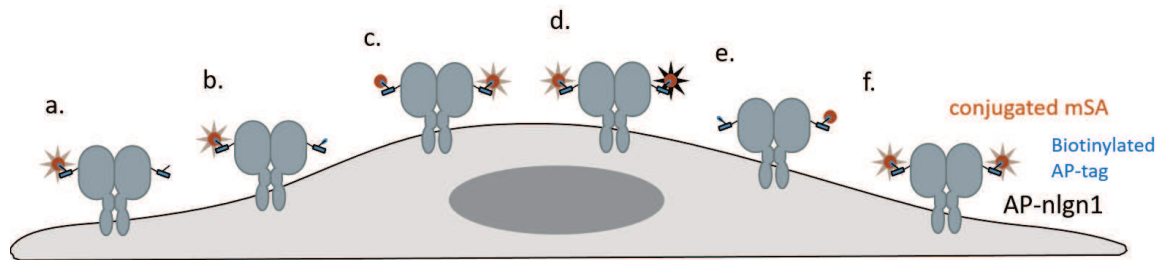


FIGURE 46: LABELING STRATEGY FOR dSTORM AND PROBE UNDERCOUNTING ILLUSTRATED ON AP-NLGN1.

Multiple critical steps in the labeling strategy may be responsible for undercounting of the probe. Undercounting of the probe may occur when the AP-tag is not biotinylated (**A**), the biotinylated AP-tag is not labeled by the probe (**B**), the probe is not conjugated to any fluorophore (**C**), or the conjugated fluorophore has been bleached prior to acquisition (**D**). Therefore, some of the targeted proteins are not visible (**E**). Correct counting occurs only when all the protein AP-tags are biotinylated and targeted by a probe conjugated to a fluorophore (**F**).

While the protein biotinylation and membrane targeting should remain constant between the different labeling conditions, the degree of conjugation of the probes differs. Moreover, the “pumping” of the fluorophores by high laser power at the beginning of the dSTORM experiment in order to reach the triplet state can be responsible for photobleaching of a non-negligible quantity of fluorophores. For these reasons, cluster integrated intensities were normalized by the mean integrated intensity of fluorophores isolated on the background, that possess the same degree of conjugation, have seen the same laser power, and supposedly have been photobleached to the same degree as fluorophores inside clusters. The limitation of this normalization is that only conjugated probes are visible, and therefore taken into account for the normalization, while non-conjugated probes are still able to target the protein of interest, which is leading to an underestimation of the protein number.

Another important limitation in terms of absolute quantification, is the fact that this quantification actually applies to the probe itself but not to the protein, and only an estimation of the number of proteins labeled by the probe can be assessed (**Figure 47**). Even if we can presume that those limitations are dealt the same way between the different conditions, a control in the protein number by adding an intrinsic fluorophore such as mEos2 or Dendra2 as an internal ruler would have been an interesting alternative, allowing a precise comparison between the probe counting and the probe counting.

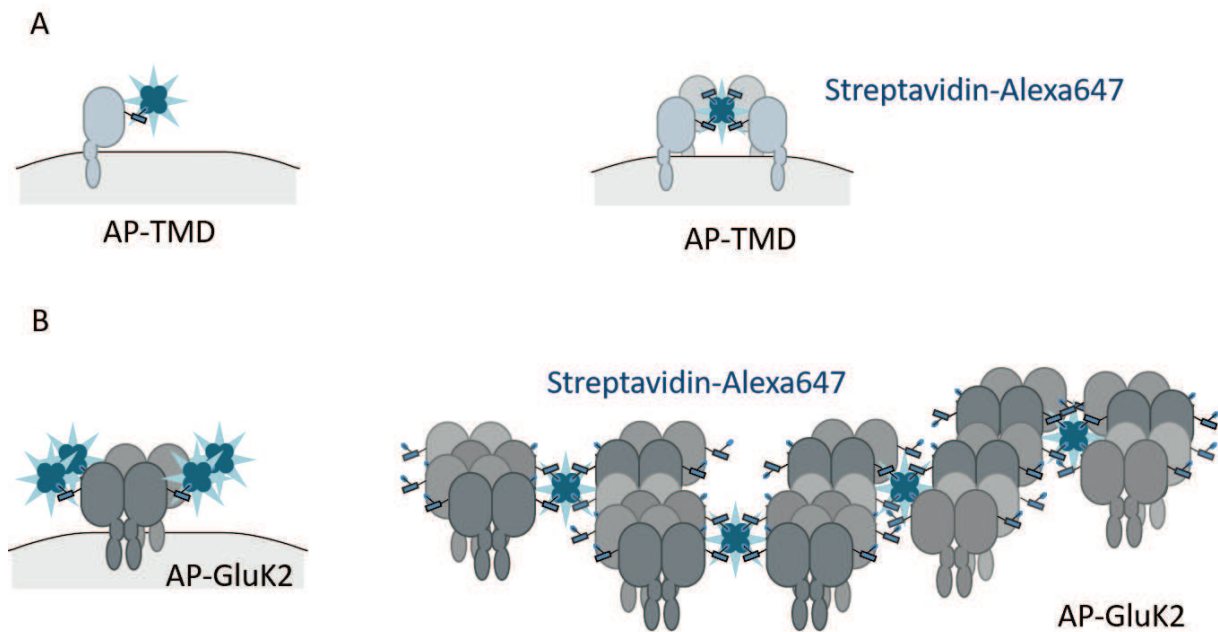


FIGURE 47: ILLUSTRATION OF THE PROBE COUNTING LIMITATIONS ON AP-TMD AND AP-GLUK2 IN dSTORM.

The interpretation of the results in terms of protein counting are limited by the fact that in dSTORM, the probe is counted and not the protein. **(A)** Counting of 1 streptavidin can be interpreted as 1 AP-TMD or 4 AP-TMD, as the streptavidin possesses 4 binding sites. **(B)** The limitations are even more exaggerated when the number of binding domains on the protein increases. Indeed, 4 streptavidins counted can be labeling 1 to 13 tetrameric AP-GluK2.

4.4. Quantification of protein levels in neurons

In this study, I provided a description of the distribution of synaptic adhesion proteins at the nanoscopic scale, namely presynaptic β -nrxn1 and its postsynaptic binding partner nlgn1, as well as the post-synaptic glutamate receptor GluK2, in the membrane of neurons by dSTORM, after live surface labeling with Alexa647-conjugated mSA. This small probe (~3nm) efficiently penetrates into crowded synaptic junctions and reduces the distance to target, as opposed to traditional antibody labeling. The wavelet segmentation based on areas with strong signal intensity compared with neighboring areas, showed enriched clusters of 30 nm to 100 nm with a mean cluster size of 60 nm, 87 nm and 57 nm, containing on an average 12, 25 and 8 mSA-labeled AP- β -nrxn1, AP-nlgn1 and AP-GluK2 respectively. Although this experiment showed that mSA labeling allows an accurate localization in synaptic compartments, quantification is complicated to interpret in terms of absolute protein number. Indeed, not only protein labeled with non-conjugated mSA are not taken into account, but saturating labeling may not be achieved, and endogenous proteins are not counted. A previous study suggests that this electroporation protocol leads to a 1:1 ratio between endogenous nlgn1

and recombinant AP-nlgn1 (Chamma et al., 2016). While this result suggests that the overexpression has little to no effect on protein organization, it has strong consequence on absolute quantification. Moreover, there is no clue about the overexpression levels of AP- β -nrxn1 and AP-GluK2, which makes any comparison problematic.

dSTORM experiments using small monovalent probes such as mSA, has the salient advantage to give access to dual-color PALM-dSTORM experiments, with accurate localization of labeled proteins in synaptic compartments. This technique, combined with wavelet segmentation, allows a precise characterization of the organization for AP-tagged proteins. Implementation with the dedicated polygone-based analysis SR-Tesseler, would go even further into domain characterization with a calculation of the local protein concentration.

However, when aiming at protein quantification, PALM or dSTORM experiments conducted in KI conditions, with one to one labeling and accurate correction for non-detected proteins, should be preferred.

4.5. Conclusion: from COS-7 to synapses

The inconsistency of my uPAINT results with the literature highlights the large variability of probe size and valence effects on protein behavior, depending on the targeted protein, and the cellular environment in terms of confinement and protein interaction.

Overall my findings on protein diffusion suggest that, low concentration labeling used for uPAINT relies on probe specificity and is not subjected to probe size and valence effects, when done in a neutral environment such as COS-7 cells, though it seems to have a greater effect in confined spaces such as synapses according to previous studies (Chamma et al., 2016; Delgado & Selvin, 2018). However, techniques using saturating concentration of probes, such as FRAP, should take into account probe size and valence, especially when targeting multiple sites on the protein of interest (e.g. polyclonal antibodies, or monoclonal antibodies targeting a multimeric protein), as it has a strong impact on protein diffusion and immobilization.

As protein diffusion is largely influenced by the membrane composition, translation of results in COS-7 to behaviors in synapses should be cautious. The different findings in the literature suggest that probe size and valence are to be exacerbated in confined environment with multiple interaction partners such as synapses (Chamma et al., 2016b; Delgado and Selvin, 2018).

In the same vein, labeling with multivalent and large probes seems to affect protein aggregation and localization, an effect which is even greater when proteins are expressed in a confined compartment. However, results are complicated to interpret, since probe size and valence are shown to have a large effect on protein aggregation, and this effect seems to be largely dependent on the targeted protein conformation as well as the cellular model used.

Although it is very tempting to use dSTORM to achieve absolute quantification of endogenous proteins, a multitude of parameters are to be taken into account. Each step in the experimentation as well as during the analysis process are subject to biases, leading to misinterpretations of the results.

Antibodies are very interesting and widely used probes as they allow to assess the diffusion and organization of endogenous protein, therefore limiting biases caused by over-expression. Overall, it is interesting to observe that those same antibodies are for some cases used to assess protein diffusion and organization and in other cases, as protein cross-linkers, to slow down protein diffusion and assess their function (Heine et al., 2008; Mondin et al., 2011). Recently, several studies observed that cross-linking with IgGs induces protein internalization in various cellular models, *in vivo* and *in vitro* (Lee et al., 2014; Peng et al., 2015), highlighting the precious care that should be taken when using such probes.

In general, labeling with mSA leads to highest diffusion coefficient, least protein immobilization, and lowest protein artificial aggregation, consistent with its small size and monovalence. This result encourages the use and development of such small and monovalent probes for super-resolution microscopy. To reach absolute quantification, labeling strategies should limit the labeling steps to minimize the risks for undercounting, yet the use of such probes is still a huge step forward in assessing proper biological function and structures as they do not alter protein localization and properties.

– CHAPTER 5 – Bibliography

- Annibale, P., Vanni, S., Scarselli, M., Rothlisberger, U., and Radenovic, A. (2011). Quantitative Photo Activated Localization Microscopy: Unraveling the effects of photoblinking. *PLoS One* *6*.
- Araç, D., Boucard, A.A., Özkan, E., Strop, P., Newell, E., Südhof, T.C., and Brunger, A.T. (2007). Structures of Neuroligin-1 and the Neuroligin-1/Neurexin-1 β Complex Reveal Specific Protein-Protein and Protein-Ca²⁺ Interactions. *Neuron* *56*, 992–1003.
- Axelrod, D. (2001). Selective imaging of surface fluorescence with very high aperture microscope objectives. *J. Biomed. Opt.*
- Bates, M., Jones, S.A., and Zhuang, X. (2013). Stochastic optical reconstruction microscopy (STORM): A method for superresolution fluorescence imaging. *Cold Spring Harb. Protoc.* *8*, 498–520.
- Bats, C., Groc, L., and Choquet, D. (2007). The Interaction between Stargazin and PSD-95 Regulates AMPA Receptor Surface Trafficking. *Neuron* *53*, 719–734.
- Beheiry, M. El, Dahan, M., and Masson, J.B. (2015). InferenceMAP: Mapping of single-molecule dynamics with Bayesian inference. *Nat. Methods* *12*, 594–595.
- Belleudi, F., Marra, E., Mazzetta, F., Fattore, L., Giovagnoli, M.R., Mancini, R., Aurisicchio, L., Torrisi, M.R., and Ciliberto, G. (2012). Monoclonal antibody-induced ErbB3 receptor internalization and degradation inhibits growth and migration of human melanoma cells. *Cell Cycle* *11*, 1455–1467.
- Benson, D.L., Colman, D.R., and Huntley, G.W. (2001). Molecules, maps and synapse specificity. *Nat. Rev. Neurosci.* *2*, 899–909.
- Bentzen, E.L., Tomlinson, I.D., Mason, J., Gresch, P., Warnement, M.R., Wright, D., Sanders-Bush, E., Blakely, R., and Rosenthal, S.J. (2005). Surface modification to reduce nonspecific binding of quantum dots in live cell assays. *Bioconjug. Chem.* *16*, 1488–1494.
- Betzig, E., Patterson, G.H., Sougrat, R., Lindwasser, O.W., Olenych, S., Bonifacino, J.S., Davidson, M.W., Lippincott-Schwartz, J., and Hess, H.F. (2006). Imaging Intracellular Fluorescent Proteins at Nanometer Resolution. *Science* (80-.). *313*, 1642–1645.
- Bharill, S., Fu, Z., Palty, R., and Isacoff, E.Y. (2014). Stoichiometry and specific assembly of Best ion channels. *Proc. Natl. Acad. Sci.* *111*, 6491–6496.
- Boeckers, T.M. (2006). The postsynaptic density. *Cell Tissue Res.* *326*, 409–422.
- Budisantoso, T., Matsui, K., Kamasawa, N., Fukazawa, Y., and Shigemoto, R. (2012). Mechanisms Underlying Signal Filtering at a Multisynapse Contact. *J. Neurosci.* *32*, 2357–2376.
- Budreck, E.C., and Scheiffele, P. (2007). Neuroligin-3 is a neuronal adhesion protein at GABAergic and glutamatergic synapses. *Eur. J. Neurosci.* *26*, 1738–1748.
- Chamma, A.I., Letellier, M., Rossier, O., and Lim, K.H. Nanoscale mapping of protein dynamics in confined cellular environments using monomeric streptavidin.
- Chamma, I., Levet, F., Sibarita, J.-B., Sainlos, M., and Thoumine, O. (2016a). Nanoscale organization of synaptic adhesion proteins revealed by single-molecule localization microscopy. *Neurophotonics* *3*, 041810.
- Chamma, I., Letellier, M., Butler, C., Tessier, B., Lim, K.H., Gauthereau, I., Choquet, D., Sibarita, J.B., Park, S., Sainlos, M., et al. (2016b). Mapping the dynamics and nanoscale organization of synaptic adhesion proteins using monomeric streptavidin. *Nat. Commun.* *7*, 10773.

- Chamma, I., Rossier, O., Giannone, G., Thoumine, O., and Sainlos, M. (2017). Optimized labeling of membrane proteins for applications to super-resolution imaging in confined cellular environments using monomeric streptavidin. *Nat. Protoc.* *12*, 748–763.
- Chen, X., Liu, H., Shim, A.H.R., Focia, P.J., and He, X. (2008). Structural basis for synaptic adhesion mediated by neuroligin-neurexin interactions. *Nat. Struct. Mol. Biol.* *15*, 50–56.
- Choquet, D., and Triller, A. (2013). The dynamic synapse. *Neuron* *80*, 691–703.
- Chubykin, A.A., Atasoy, D., Etherton, M.R., Brose, N., Kavalali, E.T., Gibson, J.R., and Südhof, T.C. (2007). Activity-Dependent Validation of Excitatory versus Inhibitory Synapses by Neuroligin-1 versus Neuroligin-2. *Neuron* *54*, 919–931.
- Contractor, A., Mulle, C., and Swanson, G.T. (2011). Kainate receptors coming of age: Milestones of two decades of research. *Trends Neurosci.* *34*, 154–163.
- Dai, M., Jungmann, R., and Yin, P. (2016). Optical visualisation of individual biomolecules in densely packed clusters. *Nat. Nanotechnologies* *11*, 798–807.
- Davidson, M.W., and Abramowitz, M. (2002). OPTICAL MICROSCOPY. *Encycl. Imaging Sci. Technol.* 1026–1032.
- Dean, C., Scholl, F.G., Choih, J., DeMaria, S., Berger, J., Isacoff, E., and Scheiffele, P. (2003). Neurexin mediates the assembly of presynaptic terminals. *Nat. Neurosci.* *6*, 708–716.
- Delgado, J.Y., and Selvin, P.R. (2018). A Revised View on the Role of Surface AMPAR Mobility in Tuning Synaptic Transmission: Limitations, Tools, and Alternative Views. *Front. Synaptic Neurosci.* *10*, 1–12.
- Deschout, H., Zanicchi, F.C., Mlodzianoski, M., Diaspro, A., Bewersdorf, J., Hess, S.T., and Braeckmans, K. (2014). Precisely and accurately localizing single emitters in fluorescence microscopy. *11*, 253–266.
- Dickson, R.M., Cubitt, A.B., Tsien, R.Y., and Moerner, W.E. (1997). On/off blinking and switching behaviour of single molecules of green fluorescent protein. *Nature* *388*, 355–358.
- Durisic, N., Laparra-Cuervo, L., Sandoval-Álvarez, Á., Borbely, J.S., and Lakadamyali, M. (2014a). Single-molecule evaluation of fluorescent protein photoactivation efficiency using an in vivo nanotemplate. *Nat. Methods* *11*, 156–162.
- Durisic, N., Cuervo, L.L., and Lakadamyali, M. (2014b). Quantitative super-resolution microscopy: Pitfalls and strategies for image analysis. *Curr. Opin. Chem. Biol.* *20*, 22–28.
- Eggeling, C., Willig, K.I., Sahl, S.J., and Hell, S.W. (2015). Lens-based fluorescence nanoscopy. *Q. Rev. Biophys.* *48*, 178–243.
- Fernández-Suárez, M., and Ting, A.Y. (2008). Fluorescent probes for super-resolution imaging in living cells. *Nat. Rev. Mol. Cell Biol.*
- Fernholm, A., and Jarnestad, J. (2014). How the optical microscope became a nanoscope. *R. Swedish Acad. Sci.* *50005*, 1–15.
- Finan, K., Raulf, A., and Heilemann, M. (2015). A Set of Homo-Oligomeric Standards Allows Accurate Protein Counting. *Angew. Chemie - Int. Ed.* *54*, 12049–12052.
- Fricke, F., Beaudouin, J., Eils, R., and Heilemann, M. (2015). One, two or three? Probing the stoichiometry of membrane proteins by single-molecule localization microscopy. *Sci. Rep.* *5*,

1–8.

Fukazawa, Y., and Shigemoto, R. (2012). Intra-synapse-type and inter-synapse-type relationships between synaptic size and AMPAR expression. *Curr. Opin. Neurobiol.* *22*, 446–452.

Futai, K., Kim, M.J., Hashikawa, T., Scheiffele, P., Sheng, M., and Hayashi, Y. (2007). Retrograde modulation of presynaptic release probability through signaling mediated by PSD-95-neuroigin. *Nat. Neurosci.* *10*, 186–195.

Galbraith, C.G., and Galbraith, J.A. (2011). Super-resolution microscopy at a glance. *J. Cell Sci.* *124*, 1607–1611.

Gautier, I., Tramier, M., Durieux, C., Coppey, J., Pansu, R.B., Nicolas, J.C., Kemnitz, K., and Coppey-Moisan, M. (2001). Homo-FRET microscopy in living cells to measure monomer-dimer transition of GFP-tagged proteins. *Biophys. J.* *80*, 3000–3008.

Giannone, G., Hosy, E., Levet, F., Constals, A., Schulze, K., Sobolevsky, A.I., Rosconi, M.P., Gouaux, E., Tampe, R., Choquet, D., et al. (2010). Dynamic superresolution imaging of endogenous proteins on living cells at ultra-high density. *Biophys. J.* *99*, 1303–1310.

Giannone, G., Hosy, E., Sibarita, J., Choquet, D., Giannone, G., Hosy, E., Sibarita, J., Choquet, D., and High, L.C. (2013a). High content Super-Resolution Imaging of Live Cell by uPAINT . To cite this version : HAL Id : hal-00796947.

Giannone, G., Mondin, M., Grillo-Bosch, D., Tessier, B., Saint-Michel, E., Czöndör, K., Sainlos, M., Choquet, D., and Thoumine, O. (2013b). Neurexin-1 β Binding to Neuroigin-1 Triggers the Preferential Recruitment of PSD-95 versus Gephyrin through Tyrosine Phosphorylation of Neuroigin-1. *Cell Rep.* *3*, 1996–2007.

Gorostiza, P., Volgraf, M., Numano, R., Szobota, S., Trauner, D., and Isacoff, E.Y. (2007). Mechanisms of photoswitch conjugation and light activation of an ionotropic glutamate receptor. *Proc. Natl. Acad. Sci.* *104*, 10865–10870.

Graf, E.R., Zhang, X., Jin, S.X., Linhoff, M.W., and Craig, A.M. (2004). Neurexins induce differentiation of GABA and glutamate postsynaptic specializations via neuroligins. *Cell* *119*, 1013–1026.

Haas, K.T., Compans, B., Letellier, M., Bartol, T.M., Grillo-Bosch, D., Sejnowski, T.J., Sainlos, M., Choquet, D., Thoumine, O., and Hosy, E. (2018). Pre-post synaptic alignment through neuroigin-1 tunes synaptic transmission efficiency. *Elife* *7*, 1–22.

Hastie, P., Ulbrich, M.H., Wang, H.-L., Arant, R.J., Lau, A.G., Zhang, Z., Isacoff, E.Y., and Chen, L. (2013). AMPA receptor/TARP stoichiometry visualized by single-molecule subunit counting. *Proc. Natl. Acad. Sci.* *110*, 5163–5168.

Heine, M., Groc, L., Frischknecht, R., Béique, J.-C., Lounis, B., Rumbaugh, G., Huganir, R.L., Cognet, L., and Choquet, D. (2008). Surface Mobility of Postsynaptic AMPARs Tunes Synaptic Transmission. *Science* (80-). *320*, 201–206.

Heldin, C.-H., and Westermark, B. (1995). Mechanism of Action and In Vivo Role of Platelet-Derived Growth Factor. *Physiol. Rev.* *79*, 1283–1316.

Holderith, N., Lorincz, A., Katona, G., Rózsa, B., Kulik, A., Watanabe, M., and Nusser, Z. (2012). Release probability of hippocampal glutamatergic terminals scales with the size of the active zone. *Nat. Neurosci.* *15*, 988–997.

- Hou, Q., Gilbert, J., and Man, H.Y. (2011). Homeostatic regulation of AMPA receptor trafficking and degradation by light-controlled single-synaptic activation. *Neuron* 72, 806–818.
- Howarth, M., and Ting, A.Y. (2008). Imaging proteins in live mammalian cells with biotin ligase and monovalent streptavidin. *Nat. Protoc.* 3, 534–545.
- Hsiao, E.Y., McBride, S.W., Hsien, S., Sharon, G., Hyde, E.R., McCue, T., Codelli, J.A., Chow, J., Reisman, S.E., Petrosino, J.F., et al. (2013). Microbiota modulate behavioral and physiological abnormalities associated with neurodevelopmental disorders. *Cell* 155, 1451–1463.
- Huang, B., Bates, M., and Zhuang, X. (2009). Super-Resolution Fluorescence Microscopy. *Annu. Rev. Biochem.* 79, 993–1016.
- Hughes, B.D., Pailthorpe, B.A., and White, L.R. (1981). The Translational And Rotational Drag On A Cylinder Moving In A Membrane. *J. Fluid Mech.* 110, 349–372.
- Ichtchenko, K., Hata, Y., Nguyen, T., Ullrich, B., Missler, M., Moomaw, C., and Südhof, T.C. (1995). Neuroligin 1: A splice site-specific ligand for β -neurexins. *Cell* 81, 435–443.
- Invitrogen (2010). The Molecular Probes® Handbook: A guide to fluorescent probes and labeling technologies. In *The Molecular Probes® Handbook*, p.
- Irie, M. (1997). Binding of Neuroligins to PSD-95. *Science* (80-). 277, 1511–1515.
- Izeddin, I., Boulanger, J., Racine, V., Specht, C.G., Kechkar, A., Nair, D., Triller, A., Choquet, D., Dahan, M., and Sibarita, J.B. (2012). Wavelet analysis for single molecule localization microscopy. *Opt. Express* 20, 2081.
- Jain, A., Liu, R., Xiang, Y.K., and Ha, T. (2012). Single-molecule pull-down for studying protein interactions. *Nat. Protoc.* 7, 445–452.
- Janovjak, H., Szobota, S., Wyart, C., Trauner, D., and Isacoff, E.Y. (2010). A light-gated, potassium-selective glutamate receptor for the optical inhibition of neuronal firing. *Nat. Neurosci.* 13, 1027–1032.
- Jüttner, R., and Rathjen, F.G. (2005). Molecular analysis of axonal target specificity and synapse formation. *Cell. Mol. Life Sci.* 62, 2811–2827.
- Kaech, S., and Banker, G. (2006). Culturing hippocampal neurons. *Nat. Protoc.* 1, 2406–2415.
- Kechkar, A., Nair, D., Heilemann, M., Choquet, D., and Sibarita, J.B. (2013). Real-Time Analysis and Visualization for Single-Molecule Based Super-Resolution Microscopy. *PLoS One* 8, e62918.
- Kienzler, M.A., Reiner, A., Trautman, E., Yoo, S., Trauner, D., and Isacoff, E.Y. (2013). A red-shifted, fast-relaxing azobenzene photoswitch for visible light control of an ionotropic glutamate receptor. *J. Am. Chem. Soc.* 135, 17683–17686.
- Kim, S., Kim, H., Yim, Y.S., Ha, S., Atarashi, K., Guan, T., Longman, R.S., Littman, D.R., Choi, G.B., Jun, R., et al. (2017). Maternal gut bacteria promote neurodevelopmental abnormalities in mouse offspring. 549, 528–532.
- Klar, T.A., Jakobs, S., Dyba, M., Egner, A., and Hell, S.W. (2000). Fluorescence microscopy with diffraction resolution barrier broken by stimulated emission. *Proc. Natl. Acad. Sci.* 97, 8206–8210.
- Kneussel, M., and Betz, H. (2000). Receptors, gephyrin and gephyrin-associated proteins:

- Novel insights into the assembly of inhibitory postsynaptic membrane specializations. *J. Physiol.* **525**, 1–9.
- Lagardère, M. (2018). Développement d'un Simulateur fondé sur la Dynamique Brownienne de molécules individuelles et dédié à l'Imagerie de Fluorescence sur Cellules Vivantes.
- Lai, Y., Choi, U.B., Leitz, J., Rhee, H.J., Lee, C., Altas, B., Zhao, M., Pfuetzner, R.A., Wang, A.L., Brose, N., et al. (2017). Molecular Mechanisms of Synaptic Vesicle Priming by Munc13 and Munc18. *Neuron* **95**, 591–607.e10.
- Lee, C.W., Zhang, H., Geng, L., and Peng, H.B. (2014). Crosslinking-induced endocytosis of acetylcholine receptors by quantum dots. *PLoS One* **9**, 1–10.
- Lee, S.H., Jin, C., Cai, E., Ge, P., Ishitsuka, Y., Teng, K.W., Thomaz, A.A. de, Nall, D.L., Baday, M., Jeyifous, O., et al. (2017). Super-resolution Imaging of Synaptic and Extra-synaptic Pools of AMPA Receptors with Different- sized Fluorescent Probes. *Elife* **1–26**.
- Leemans, A., Schryver, M. De, Gucht, W. Van der, Heykers, A., Pintelon, I., Hotard, A.L., Moore, M.L., Melero, J.A., McLellan, J.S., Graham, B.S., et al. (2017). Antibody-Induced Internalization of the Human Respiratory Syncytial Virus Fusion Protein. *J. Virol.* **91**, 1–15.
- Lerma, J., and Marques, J.M. (2013). Kainate receptors in health and disease. *Neuron* **80**, 292–311.
- Letellier, M., Elramah, S., Mondin, M., Soula, A., Penn, A., Choquet, D., Landry, M., Thoumine, O., and Favereaux, A. (2014). MiR-92a regulates expression of synaptic GluA1-containing AMPA receptors during homeostatic scaling. *Nat. Neurosci.* **17**, 1040–1042.
- Letellier, M., Szíber, Z., Chamma¹, I., Saphy, C., Papisideri, I., Tessier, B., Sainlos, Matthieu Czöndör, K., and Thoumine, O. (2018). A unique intracellular tyrosine in neuroligin-1 regulates AMPA receptor recruitment during synapse differentiation and potentiation. *Nat. Commun. in press*.
- Levet, F., Hosy, E., Kechkar, A., Butler, C., Beghin, A., Choquet, D., and Sibarita, J.B. (2015). SR-Tesseler: A method to segment and quantify localization-based super-resolution microscopy data. *Nat. Methods* **12**, 1065–1071.
- Levitz, J., Popescu, A.T., Reiner, A., and Isacoff, E.Y. (2016). A Toolkit for Orthogonal and in vivo Optical Manipulation of Ionotropic Glutamate Receptors. *Front. Mol. Neurosci.* **9**, 1–15.
- Li, T.P., and Blanpied, T.A. (2016). Control of transmembrane protein diffusion within the postsynaptic density assessed by simultaneous single-molecule tracking and localization microscopy. *Front. Synaptic Neurosci.* **8**, 1–14.
- Li, T.P., Song, Y., MacGillavry, H.D., Blanpied, T.A., and Raghavachari, S. (2016). Protein Crowding within the Postsynaptic Density Can Impede the Escape of Membrane Proteins. *J. Neurosci.* **36**, 4276–4295.
- Lichtman, J.W., and Conchello, J.-A. (2005). Fluorescence Microscopy. *Nat. Methods* **2**, 910–919.
- Lim, K.H., Huang, H., Pralle, A., and Park, S. (2013). Stable, high-affinity streptavidin monomer for protein labeling and monovalent biotin detection. *Biotechnol. Bioeng.* **110**, 57–67.
- Liu, D.S., Loh, K.H., Lam, S.S., White, K.A., and Ting, A.Y. (2013). Imaging Trans-Cellular Neurexin-Neuroligin Interactions by Enzymatic Probe Ligation. *PLoS One* **8**.

- Makio Tokunaga, Imamoto, N., and Sakata-Sogawa, K. (2008). Highly inclined thin illumination enables clear single-molecule imaging in cells. *Nat. Methods* 5, 159–161.
- Malinow, R., and Malenka, R.C. (2002). AMPA Receptor Trafficking and Synaptic Plasticity. *Annu. Rev. Neurosci.* 25, 103–126.
- Manley, S., Gillette, J.M., Patterson, G.H., Shroff, H., Hess, H.F., Betzig, E., and Lippincott-Schwartz, J. (2008). High-density mapping of single-molecule trajectories with photoactivated localization microscopy. *Nat. Methods* 5, 155–157.
- Masson, J.B., Dionne, P., Salvatico, C., Renner, M., Specht, C.G., Triller, A., and Dahan, M. (2014). Mapping the energy and diffusion landscapes of membrane proteins at the cell surface using high-density single-molecule imaging and bayesian inference: Application to the multiscale dynamics of glycine receptors in the neuronal membrane. *Biophys. J.* 106, 74–83.
- McGuire, H., Aourousseau, M.R.P., Bowie, D., and Bluncks, R. (2012). Automating single subunit counting of membrane proteins in mammalian cells. *J. Biol. Chem.* 287, 35912–35921.
- Michalet, X., Pinaud, F.F., Bentolila, L.A., Tsay, J.M., Doose, S., Li, J.J., Sundaresan, G., Wu, A.M., Gambhir, S.S., and Weiss, S. (2005). Quantum Dots for Live Cells, in Vivo Imaging, and Diagnostics. *Science* (80-). 307, 538–545.
- Mondin, M., Labrousse, V., Hosy, E., Heine, M., Tessier, B., Levet, F., Poujol, C., Blanchet, C., Choquet, D., and Thoumine, O. (2011). Neurexin-Neurologin Adhesions Capture Surface-Diffusing AMPA Receptors through PSD-95 Scaffolds. *J. Neurosci.* 31, 13500–13515.
- Nagano, K., Bornhauser, B.C., Warnasuriya, G., Entwistle, A., Cramer, R., Lindholm, D., and Naaby-Hansen, S. (2006). PDGF regulates the actin cytoskeleton through hnRNP-K-mediated activation of the ubiquitin E3-ligase MIR. *EMBO J.* 25, 1871–1882.
- Nair, D., Hosy, E., Petersen, J.D., Constals, A., Giannone, G., Choquet, D., and Sibarita, J.-B. (2013). Super-Resolution Imaging Reveals That AMPA Receptors Inside Synapses Are Dynamically Organized in Nanodomains Regulated by PSD95. *J. Neurosci.* 33, 13204–13224.
- Okabe, S., Urushido, T., Konno, D., Okado, H., and Sobue, K. (2001). Rapid Redistribution of the Postsynaptic Density Protein PSD-Zip45 (Homer 1c) and Its Differential Regulation by NMDA Receptors and Calcium Channels. *J. Neurosci.*
- Opazo, F., Levy, M., Byrom, M., Schäfer, C., Geisler, C., Groemer, T.W., Ellington, A.D., and Rizzoli, S.O. (2012). Aptamers as potential tools for super-resolution microscopy. *Nat. Methods* 9, 938–939.
- Orre, T. (2016). MÉCANISMES MOLÉCULAIRES D’ACTIVATION DES INTÉGRINES PAR LA KINDLINE-2 LORS DE L’ADHÉSION CELLULAIRE Sous.
- Patrizio, A., and Specht, C.G. (2016). Counting numbers of synaptic proteins: absolute quantification and single molecule imaging techniques. *Neurophotonics* 3, 041805.
- Patrizio, A., Renner, M., Pizzarelli, R., Triller, A., and Specht, C.G. (2017). Alpha subunit-dependent glycine receptor clustering and regulation of synaptic receptor numbers. *Sci. Rep.* 7, 1–11.
- Peng, X., Hughes, E.G., Moscato, E.H., Parsons, T.D., Dalmau, J., and Balice-Gordon, R.J. (2015). Cellular plasticity induced by anti- α -amino-3-hydroxy-5-methyl-4-isoxazolepropionic acid (AMPA) receptor encephalitis antibodies. *Ann. Neurol.* 77, 381–398.

- Penn, A.C., Zhang, C.L., Georges, F., Royer, L., Breillat, C., Hosy, E., Petersen, J.D., Humeau, Y., and Choquet, D. (2017). Hippocampal LTP and contextual learning require surface diffusion of AMPA receptors. *Nature* *549*, 384–388.
- Pennacchietti, F., Vascon, S., Nieus, T., Rosillo, C., Das, S., Tyagarajan, S.K., Diaspro, A., Del Bue, A., Petrini, E.M., Barberis, A., et al. (2017). Nanoscale Molecular Reorganization of the Inhibitory Postsynaptic Density Is a Determinant of GABAergic Synaptic Potentiation. *J. Neurosci.* *37*, 1747–1756.
- Petrov, E.P., and Schwille, P. (2008). Translational diffusion in lipid membranes beyond the Saffman-Delbrück approximation. *Biophys. J.* *94*, 41–43.
- Pinaud, F., Clarke, S., Sittner, A., and Dahan, M. (2010). Probing cellular events, one quantum dot at a time. *Nat. Methods* *7*, 275–285.
- Poulopoulos, A., Aramuni, G., Meyer, G., Soykan, T., Hoon, M., Papadopoulos, T., Zhang, M., Paarmann, I., Fuchs, C., Harvey, K., et al. (2009). Neuroligin 2 Drives Postsynaptic Assembly at Perisomatic Inhibitory Synapses through Gephyrin and Collybistin. *Neuron* *63*, 628–642.
- Pozo, K., and Goda, Y. (2010). Unraveling mechanisms of homeostatic synaptic plasticity. *Neuron* *66*, 337–351.
- Reiner, A., Arant, R.J., and Isacoff, E.Y. (2012). Assembly Stoichiometry of the GluK2/GluK5 Kainate Receptor Complex. *Cell Rep.* *1*, 234–240.
- Reits, E.A.J., and Neefjes, J.J. (2001). From fixed to FRAP: measuring protein mobility and activity in living cells. *Nat. Cell Biol.* *3*.
- Renner, M., Wang, L., Levi, S., Hennekinne, L., and Triller, A. (2017). A Simple and Powerful Analysis of Lateral Subdiffusion Using Single Particle Tracking. *Biophys. J.* *113*, 2452–2463.
- Renz, M., Daniels, B.R., Vamosi, G., Arias, I.M., and Lippincott-Schwartz, J. (2012). Plasticity of the asialoglycoprotein receptor deciphered by ensemble FRET imaging and single-molecule counting PALM imaging. *Proc. Natl. Acad. Sci.* *109*, E2989–E2997.
- Reza Vafabakhsh (2013). SINGLE MOLECULE FLUORESCENCE STUDIES OF BIOMOLECULAR INTERACTIONS.
- Ries, J., Kaplan, C., Platonova, E., Eghlidi, H., and Ewers, H. (2012). A simple, versatile method for GFP-based super-resolution microscopy via nanobodies. *Nat. Methods* *9*, 582–584.
- Rust, M.J., Bates, M., and Zhuang, X. (2006). Sub-diffraction-limit imaging by stochastic optical reconstruction microscopy (STORM). *Nat. Methods* *3*, 793–795.
- Saffman, G., and Saffman, P.G. (2006). Brownian motion in thin sheets of viscous fluid. *J. Fluid Mech.* *73*, 593.
- Saffman, P.G., and Delbrück, M. (1975). Brownian motion in biological membranes (diffusion). *Biophysics (Oxf).* *72*, 3111–3113.
- Saxton, M.J., and Jacobson, K. (1997). SINGLE-PARTICLE TRACKING: Applications to Membrane Dynamics. *Annu. Rev. Biophys. Biomol. Struct.* *26*, 373–399.
- Schermelleh, L., Carlton, P.M., Haase, S., Shao, L., Winoto, L., Winoto, L., Kner, P., Kner, P., Burke, B., Cardoso, M.C., et al. (2008). Subdiffraction multicolor imaging of the nuclear periphery with 3D structured illumination microscopy. *Science (80-)*. *320*, 1332–1336.

- Schnitzbauer, J., Strauss, M.T., Schlichthaerle, T., Schueder, F., and Jungmann, R. (2017). Super-resolution microscopy with DNA-PAINT. *Nat. Protoc.* *12*, 1198–1228.
- Schreiner, D., Nguyen, T.M., Russo, G., Heber, S., Patrignani, A., Ahrné, E., and Scheiffele, P. (2014). Targeted Combinatorial Alternative Splicing Generates Brain Region-Specific Repertoires of Neurexins. *Neuron* *84*, 386–398.
- Sengupta, P., Jovanovic-Talisman, T., and Lippincott-Schwartz, J. (2013). Quantifying spatial organization in point-localization superresolution images using pair correlation analysis. *Nat. Protoc.* *8*, 345–354.
- Sergé, A., Bertaux, N., Rigneault, H., and Marguet, D. (2008). Dynamic multiple-target tracing to probe spatiotemporal cartography of cell membranes. *Nat. Methods* *5*, 687–694.
- Shen, K., and Scheiffele, P. (2010). Genetics and Cell Biology of Building Specific Synaptic Connectivity. *Annu. Rev. Neurosci.* *33*, 473–507.
- Shi, Y., Lu, W., Milstein, A.D., and Nicoll, R.A. (2009). The Stoichiometry of AMPA Receptors and TARPs Varies by Neuronal Cell Type. *Neuron* *62*, 633–640.
- Shimomura, O., Johnson, F.H., and Saiga, Y. (1962). Extraction, purification and properties of aequorin, a bioluminescent protein from the luminous hydromedusan, *Aequorea*. *J. Cell. Physiol.*
- Shinohara, Y. (2009). Size and receptor density of glutamatergic synapses: a viewpoint from left-right asymmetry of CA3-CA1 connections. *Front. Neuroanat.* *3*, 1–6.
- Sibarita, J. (2014). High-density single-particle tracking: quantifying molecule organization and dynamics at the nanoscale. *Histochem Cell Biol* *141*, 587–595.
- Sobolevsky, A.I. (2015). Structure and gating of tetrameric glutamate receptors. *J. Physiol.* *593*, 29–38.
- Song, J.Y., Ichtchenko, K., Südhof, T.C., and Brose, N. (1999). Neuroligin 1 is a postsynaptic cell-adhesion molecule of excitatory synapses. *Proc. Natl. Acad. Sci. U. S. A.* *96*, 1100–1105.
- Soumpasis, D.M. (1983). Theoretical analysis of fluorescence photobleaching recovery experiments. *Biophys. J.* *41*, 95–97.
- Specht, C.G., Izeddin, I., Rodriguez, P.C., ElBeheiry, M., Rostaing, P., Darzacq, X., Dahan, M., and Triller, A. (2013). Quantitative nanoscopy of inhibitory synapses: Counting gephyrin molecules and receptor binding sites. *Neuron* *79*, 308–321.
- Strauss, S., Nickels, P.C., Strauss, M.T., Jimenez Sabinina, V., Ellenberg, J., Carter, J.D., Gupta, S., Janjic, N., and Jungmann, R. (2018). Modified aptamers enable quantitative sub-10-nm cellular DNA-PAINT imaging. *Nat. Methods* *15*, 685–688.
- Südhof, T.C. (2017). Synaptic Neurexin Complexes: A Molecular Code for the Logic of Neural Circuits. *Cell* *171*, 745–769.
- Sutton, M.A., Ito, H.T., Cressy, P., Kempf, C., Woo, J.C., and Schuman, E.M. (2006). Miniature Neurotransmission Stabilizes Synaptic Function via Tonic Suppression of Local Dendritic Protein Synthesis. *Cell* *125*, 785–799.
- Szobota, S., Gorostiza, P., Del Bene, F., Wyart, C., Fortin, D.L., Kolstad, K.D., Tulyathan, O., Volgraf, M., Numano, R., Aaron, H.L., et al. (2007). Remote Control of Neuronal Activity with a Light-Gated Glutamate Receptor. *Neuron* *54*, 535–545.

- Tarusawa, E., Matsui, K., Budisantoso, T., Molnar, E., Watanabe, M., Matsui, M., Fukazawa, Y., and Shigemoto, R. (2009). Input-Specific Intrasynaptic Arrangements of Ionotropic Glutamate Receptors and Their Impact on Postsynaptic Responses. *J. Neurosci.* *29*, 12896–12908.
- Thompson, R.E., Larson, D.R., and Webb, W.W. (2002). Precise Nanometer Localization Analysis for Individual Fluorescent Probes. *Biophys. J.* *82*, 2775–2783.
- Toomre, D., and Bewersdorf, J. (2010). A New Wave of Cellular Imaging. *Annu. Rev. Cell Dev. Biol.* *26*, 285–314.
- Treutlein, B., Gokce, O., Quake, S.R., and Südhof, T.C. (2014). Cartography of neurexin alternative splicing mapped by single-molecule long-read mRNA sequencing. *Proc. Natl. Acad. Sci.* *111*, E1291–E1299.
- Tsien, R.Y. (1998). The Green Fluorescent Protein. *Annu. Rev. Biochem.* *67*, 509–544.
- Turrigiano, G.G. (2008). The Self-Tuning Neuron: Synaptic Scaling of Excitatory Synapses. *Cell* *135*, 422–435.
- Turrigiano, G.G., Leslie, K.R., Desai, N.S., Rutherford, L.C., and Nelson, S.B. (1998). Activity-dependent scaling of quantal amplitude in neocortical neurons. *Nature* *391*, 892–896.
- Ulbrich, M.H., and Isacoff, E.Y. (2007). Subunit counting in membrane-bound proteins. *Nat. Methods* *4*, 319–321.
- Ulbrich, M.H., and Isacoff, E.Y. (2008). Rules of engagement for NMDA receptor subunits. *Proc. Natl. Acad. Sci.* *105*, 14163–14168.
- Verhage, M., Maia, A.S., Plomp, J.J., Brussaard, A.B., Heeroma, J.H., Vermeer, H., Toonen, R.F., Hammer, R.E., Van Den Berg, T.K., Missler, M., et al. (2000). Synaptic assembly of the brain in the absence of neurotransmitter secretion. *Science* (80-.). *287*, 864–869.
- Volgraf, M., Gorostiza, P., Numano, R., Kramer, R.H., Isacoff, E.Y., and Trauner, D. (2006). Allosteric control of an ionotropic glutamate receptor with an optical switch. *Nat. Chem. Biol.* *2*, 47–52.
- Weber, P.C., Ohlendorf, D.H., Wendoloski, J.J., and Salemme, F.R. (1989). Structural Origins of High-Affinity Biotin Binding To Streptavidin. *Science* (80-.). *243*, 85–88.
- Zhang, P., Lu, H., Peixoto, R.T., Pines, M.K., Ge, Y., Oku, S., Siddiqui, T.J., Xie, Y., Wu, W., Archer-Hartmann, S., et al. (2018). Heparan Sulfate Organizes Neuronal Synapses through Neurexin Partnerships. *Cell* 1–15.

– ANNEXES –

Role of nlg1 and nlg3 phosphorylation and neuronal activity in synaptic differentiation

Given their interactions with extra- and intra-cellular partners, both at the pre- and at the post-synapse, synaptic adhesion proteins appear as a keystone in the regulation of synapse formation, morphology, and function. Among those, the well-studied neurexin/neuroigin complex is particularly interesting, through its role in synapse differentiation and specification. Since neuroligins are so homologous among isoforms, and their cytoplasmic sequences appear to bind to the same intra-cellular proteins *in vitro*, it is unclear how the different neuroligins are sorted to distinct types of synapses in a given neuron, and by what mechanisms they mediate their distinct functions. Based on previous work from the team (Giannone et al., 2013), suggesting that the phosphorylation on a unique intracellular tyrosine residue conserved among neuroligin isoforms (at position 782 in nlg1) would be responsible for the differentiation of excitatory or inhibitory post-synapses, I participated to a broad study from the group focusing on the effects of neuroligin1 mutations on this tyrosine residue (Y782A/F) on excitatory synapse formation and function, and the regulation of nlg1 tyrosine phosphorylation by specific kinases (Letellier et al., 2018). Given the interplay between neurexin/neuroigin function and synaptic activity (Chubykin et al., 2007), I initially studied the role of chronically blocking NMDA receptor activity with AP5 on the effect of the nlg1 mutations. Surprisingly, we were not able to reproduce the effect of APV on miniature EPSCs, although changes in VGlut1 and GluA1 staining could be observed. The neuroligin3 isoform being present at both excitatory and inhibitory synapses, I also studied the impact of neuroligin3 mutants on the formation of excitatory and inhibitory synapses, with the hypothesis that the tyrosine phosphorylation would act as a switch in the synaptic differentiation. It turns out that although Nlg3 can also be phosphorylated at this conserved residue (Y792), the impact of this mechanism on excitatory synaptic differentiation is much pronounced for nlg1 than for nlg3. Some of my results, in particular the recordings of miniature AMPAR-mediated EPSCs upon expression of nlg1 WT or mutants, have been incorporated in this paper.

Use of light-gated glutamate receptors (LiGluRs) to control homeostatic synaptic scaling

While SCAMs play a central role in the synapse induction and differentiation, neuronal activity is a keystone for the maintenance of the newly-formed synapses (Benson et al., 2001; Jüttner and Rathjen, 2005). Indeed, although the initial synapse formation step does not depend on neurotransmitter secretion, the final specificity achieved by pruning away the incorrect terminal sites seems to be an activity-mediated process (Benson et al., 2001; Lai et al., 2017; Shen and Scheiffele, 2010; Verhage et al., 2000). It is not clear either how and to what extent synaptic activity influences synaptic adhesion and *vice versa* to stabilize or destabilize specific synapses depending on the environment.

In the adult brain, neuronal activity not only serves the neuronal communication to transfer ongoing information, but is also a key feature for information storage and memory formation. The most widely-studied form of synaptic adaptation is the Hebbian plasticity, with the long term potentiation (LTP) and long term depression (LTD), as synaptic changes operate in a positive feed-back process, where the efficacy of individual synapses is rapidly modified in an input-specific manner. In this system, synapses undergoing LTP become more excitable and the threshold for further LTP is reduced. However, as neuronal networks would lose their synapse specificities if they underwent unconstrained potentiation or depression, a homeostatic compensatory system is necessary to tune the overall sensitivity of the network, constraining runaway activity and preventing saturated synapses from undergoing further potentiation (Pozo and Goda, 2010; Turrigiano, 2008). Several mechanisms of homeostatic compensation have now been identified, revealing the ways in which neurons may sense their own activity level and accordingly adjust their properties to maintain stability. A canonical example experiment is the suppression of all network activity by tetrodotoxin (TTX) for 24-48 hrs, which results in a slow compensatory increase in synapse strength, notably post-synaptic AMPA receptors are up-regulated following activity blockade. Conversely, enhancing network activity by blocking inhibitory inputs results in a decrease in the strength of excitatory

synapses (G. G. Turrigiano et al., 1998). Another well-characterized homeostatic scaling is the expression increase of GluA1 homomeric AMPA receptors through local translation of GluA1 mRNAs present in the dendrite, following hippocampal neuron treatment with TTX (to prevent action potential) and AP5 (to further block NMDA receptors-mediated miniature synaptic transmission), which occurs in a smaller time frame (4 hrs) (Sutton et al., 2006). Previous work in the team showed that this mechanism relies on the downregulation of the micro-RNA miR-92a, which leads to a de-repression of GluA1 translation (Letellier et al., 2014).

Although genetic manipulation and chronic drug treatments are frequently used to investigate the role of activity in diverse systems, another interesting approach is the use of light-gated glutamate receptors. Those receptors are engineered so the ionic channel would get activated by light pulses instead or on top of ligand-gating. Among those, the LiGluR, a light-gated GluK2 kainate receptors was developed in Isacoff's laboratory (Volgraf et al., 2006). This kainate receptor subunit is an ionotropic cation-permeant channel, leading to the depolarization of the cell membrane, and thus the excitation of the neuron, which makes the LiGluR an interesting tool to assess the effect of neuronal activity on various systems. Furthermore, it has been used as an optogenetic tool to control cellular excitability in different models: in cultured neurons and glia (Hou, Gilbert, & Man, 2011; Szobota et al., 2007), brain slices (Janovjak et al., 2010), and *in vivo* (Szobota et al., 2007).

Direct optical control of the glutamate receptor is achieved by covalently attaching a photoswitchable tethered ligand of the L-MAG family (Maleimide Azobenzene Glutamate) to the receptor of interest, which is expressed with a cysteine substitution (L439C) close to the ligand binding site (Volgraf et al., 2006) (**Figure 48A**). Once the MAG ligands are attached to the receptor *via* a covalent maleimide-cysteine linkage, activation can be obtained upon light illumination, which isomerizes the MAG azobenzene moiety from *trans* to *cis*, reversibly presenting the glutamate headgroup to the ligand binding domain (**Figure 48B**). Deactivation is achieved by the isomerization of the MAG ligand back to its *trans* configuration, retracting the ligand from its binding site, either upon 500 nm illumination (**Figure 48C**), or through spontaneous relaxation (**Figure 48D**), depending on the type of MAG used.

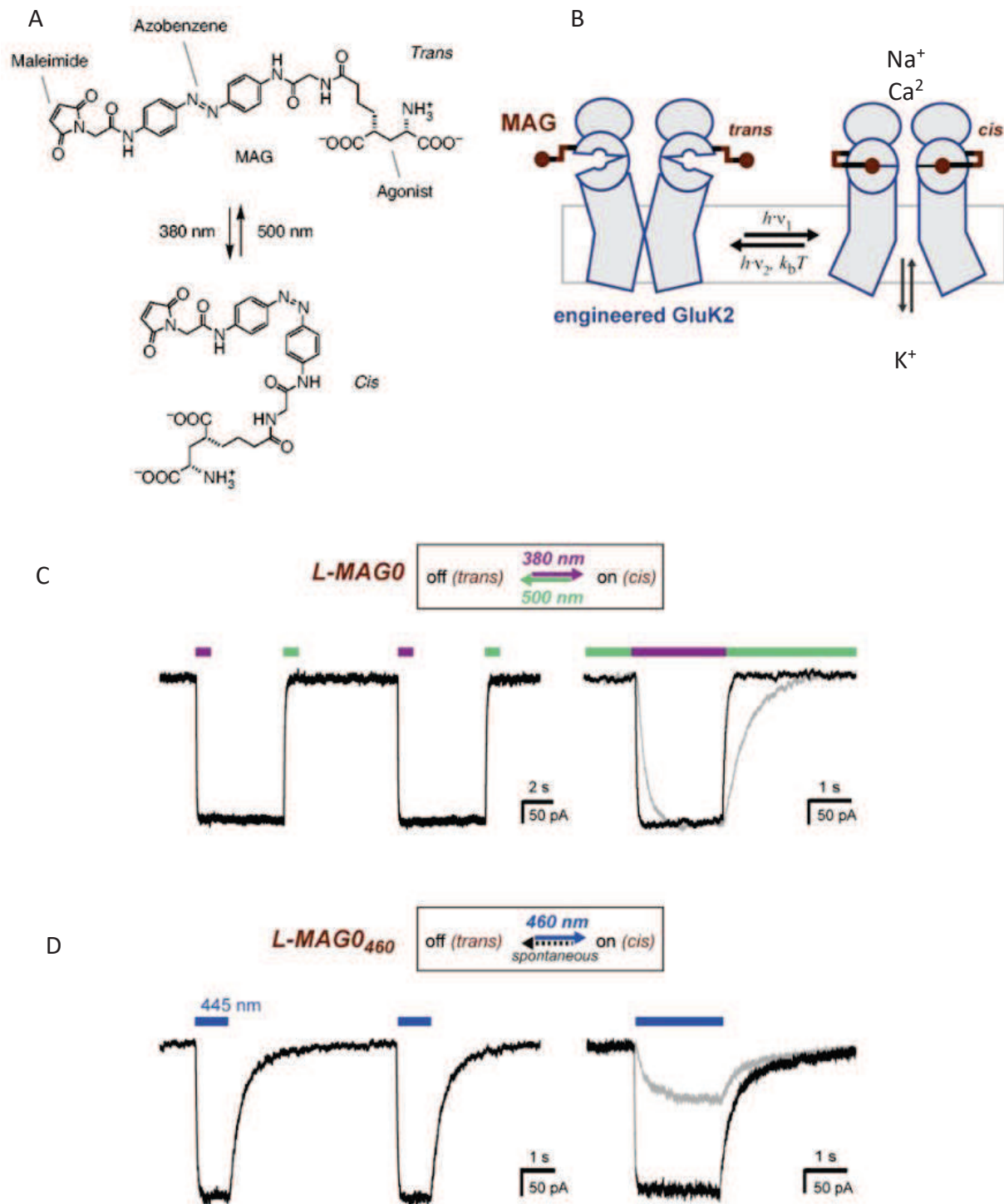


FIGURE 48. PRINCIPLES OF LIGHT-GATED GLUTAMATE RECEPTORS (LIGLURS).

(A) Structure of the synthetic photoswitchable ligand MAGO: this compound features a cysteine-reactive maleimide, an azobenzene photoswitched in its *trans*- (top) and *cis*- state (bottom), by 500 nm and 380 nm light exposure respectively, and a glutamate head group.

(B) Photoisomerization of the covalently bound MAG ligand from *trans* to *cis* presents the glutamate moiety to the glutamate binding site, which leads to ligand binding and ion channel opening.

(C) Photoswitching of LiGluR labeled with a regular, bistable MAG ligand (Gorostiza et al., 2007; Volgraf et al., 2006). 380 nm illumination (violet bar) leads to an inward current as shown in a voltage-clamp recording of a LiGluR-expressing HEK cell labeled with L-MAGO. The receptor activation is sustained in

the dark and turned off by 500 nm illumination (green bar). (Left) Switching is fully reversible, and (right) lowering the light intensity leads to slower photo-activation and deactivation kinetics, but the same current amplitude (black trace $\sim 7\text{-}8\text{ mW/mm}^2$; gray trace $\sim 0.7\text{-}0.8\text{ mW/mm}^2$).

(D) Photoswitching of LiGluR labeled with L-MAGO₄₆₀, a blue light activated photoswitch with a fast spontaneous *cis*-to-*trans* relaxation (Kienzler et al., 2013). (Left) HEK cell voltage-clamp recording showing two switching cycles with 445 nm light (blue bar). Once the blue light is turned off, LiGluR turns off spontaneously. (Right) Lowering the light intensity results in slower activation kinetics and a decreased response (black trace $\sim 1.5\text{ mW/mm}^2$; gray trace $\sim 0.1\text{ mW/mm}^2$). HEK cell recordings were performed in the presence of ConA.

(Adapted from Levitz et al., 2016; Volgraf et al., 2006).

From this primary LiGluR, mutations have been introduced to change the channel properties. On top of original L439C allowing the MAG linkage, the mutations R456A and E738D reduce the sensitivity to endogenous glutamate, so that channel opening would happen exclusively when MAG is photoswitched.

I started my PhD by investigating homeostatic regulation of AMPA receptor expression at synapses by a combination of synaptic deprivation and optogenetic restoration of activity. The rationale was that by triggering LiGluR activity using chronic light delivery, we could inhibit homeostatic synaptic scaling induced by pharmacology (TTX, APV) in a cell-autonomous fashion. In this context, I first characterized the effect of expressing such recombinant light-gated receptors on the number of synapses and the content of AMPA receptors per synapse, by electrophysiology recordings on miniature excitatory post-synaptic currents (mEPSC), in cultured neurons. Even if a small augmentation can be observed in mEPSC frequency of neurons expressing the different LiGluRs, I found no significant effect of LiGluR expression on mEPSC frequency and amplitude (**Figure 49**), suggesting that they would not interfere with the induction of the scaling process.

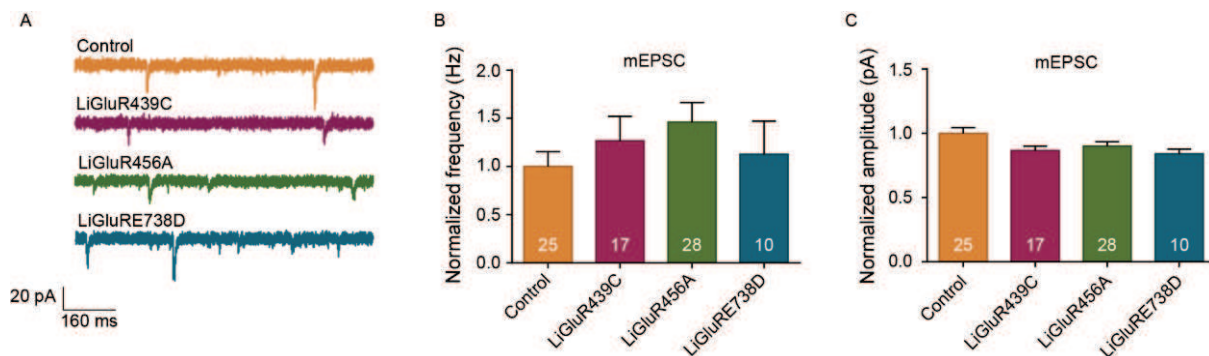


FIGURE 49: EFFECT OF LiGLURs EXPRESSION ON MEPCs OF CULTURED NEURONS

(A) Representative recordings of AMPA receptor mEPSCs from 14 DIV neurons. (B) Mean AMPA receptor mEPSC frequency, and (C) amplitude for each condition, normalized by the control condition. (Mean with SEM represented). Numbers in the bar charts represent the number of cells analyzed.

Then, I assessed the effect of chronic wide-field activation of LiGluR439C (100 ms 470 nm light activation of MAG0 every 15 s for 3 hours using an LED array) on the synaptic content in AMPA receptors, both by electrophysiology and immunocytochemistry. While I observed no effect of the chronic activation on mEPSC frequency and amplitude, an augmentation in SEP-GluA1

staining was present (Figure 50), contrary to the expected result that LiGluR activation would inhibit GluA1 expression (as found by unpublished results from the Isacoff's laboratory). Finally, I investigated the effect of LiGluR chronic activation on the AMPA receptor scaling induced by TTX and AP-5 chronic treatment. I was unable to detect AMPA receptor upscaling both by electrophysiology and immunocytochemistry and stopped the project.

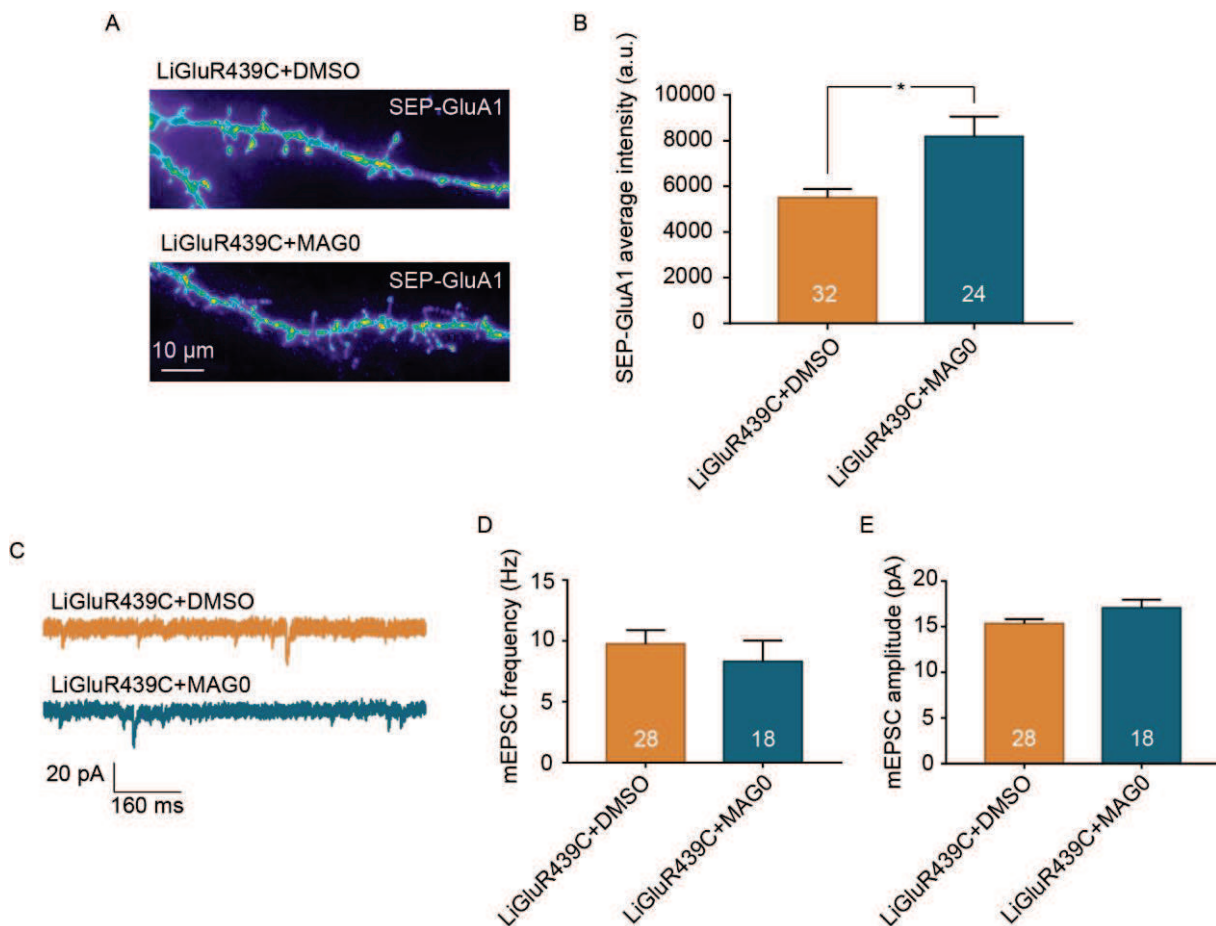


FIGURE 50: EFFECT OF CHRONIC WIDE-FIELD LIGHT-ACTIVATION OF LiGLUR ON AMPA RECEPTOR AND SYNAPSE NUMBER.

Neurons were transfected at DIV 10 with LiGluR439C and SEP-GluA1 or Td tomato. At DIV 14, DMSO (control) or MAG0 was applied, and light-activation was achieved by illuminating for 100 ms every 15s during 3 hrs. (A) SEP-GluA1 surface staining in neurons transfected with LiGluR439C and SEP-GluA1, stained with anti-GFP antibody before fixation, and (B) SEP-GluA1 average intensity after chronic light-exposition. (* $p < 0.05$). (C) Representative recordings of AMPA receptor mEPSCs. (D) Mean AMPA receptor mEPSC frequency, and (E) amplitude for each condition. (Mean and SEM represented) Numbers in the bar charts represent the number of cells analyzed.